ABSTRACT

FLARE EMISSION OBSERVED IN HIGH RESOLUTION AND COMPARISON WITH NUMERICAL MODELING

by
Nengyi Huang

As one of the most intense activities on the solar surface, flares have been extensively observed and studied ever since the first report [28]. The standard model of solar flares has been established and commonly accepted. However, many limitations from the researching tools have left some of the problems unsolved or controversial. For example, the density of electrons in the corona is lower than is required to activate the observed emission in hard X-ray (HXR), and the mechanism of how these electron beams can penetrate down to the lower chromosphere is unclear. Many theoretical scenarios are suggested, and more observations are required.

Multi-wavelength observations are powerful tools in revealing the details of solar flares. Following the improvement of research instruments, such as spacecraft, telescopes, charged-coupled devices (CCDs), and computing devices, we are able to make better use of the emissions for understanding the flare. For instance, Goode Solar Telescope in Big Bear Solar Observatory (BBSO/GST), equipped with a 1.6-meter clear aperture primary mirror, has been dedicated to solar observation. With the diffraction-limited resolution up to about 0.1 ″, GST is capable of providing detailed information on fine structures in solar flares. Interface Region Imaging Spectrograph (IRIS) offers images in the ultraviolet (UV) together with spectrograms over several wavelength windows, including tens of spectral lines that are powerful in diagnosing the flaring atmosphere. Solar Dynamic Observatory (SDO) records solar full-disk images in multiple wavelengths, from the extreme ultraviolet (EUV) to the visible continuum, covering a wide range of temperatures. Moreover, thanks to the

improvement of computing power, more plausible codes are developed to calculate the flaring atmosphere.

Taking advantages of the high-resolution instruments and novel numerical modeling packages, the dissertation work covers several topics, from the energetics of white-light (WL) emission in macroscope to the sub-arcsecond features on flare ribbons in multiple wavelengths and the corresponding modeling. As summarized below, the major results provide additional and important constraints in understanding the flare emission and instructive for future observations and developing of new modeling:

- Using the SDO/HMI images and RHESSI HXR spectra, a relationship between WL and HXR emissions was studied. The correlation between HXR power-law indices and WL emissions indicates the importance of non-thermal electrons' energy distribution in stimulating the WL flares. This suggests the direct heating mechanism accounts for the core of the compact WL flares.

- The WL flares, which are considered to be in the most violent class, and solar energetic particle (SEP) events are under survey, and no clear correlation is found between them. Straightforward speculation is that the acceleration process could be different for SEPs and the energetic electrons powering WLFs in the events analyzed.

- Emissions from chromospheric spectral lines, Mg II k line and Hα are observed using IRIS and BBSO/GST, respectively, for the flare on 2015-06-22. Unique features of the line profiles are observed in the narrow edge of the ribbon. A numerical study using a combination code of RADYN and RH suggests the formation height and corresponding thermodynamic conditions of the distinct line feature.

- Inspired by a study of solar flares in He I 10830 Å line that observed enhancement absorption in the frontiers of flare ribbons, we analyze the evolution of the line emission in numerical models and compare it with observations. The result suggests that the temperatures and free electron densities at heights of 1.3-1.5 Mm should be larger than $\sim 10^4$ K and 6×10^{11} cm^{-3} are thresholds for the line to start being in emission.

- With the high-resolution vector magnetogram, in wavelength of 1.56μm that is from the lower layer of the atmosphere, a transient rotation of the local magnetic field is observed in the leading edge of 2015-06-22 flare ribbon. The azimuth angle rotates closer to the extrapolated potential field. This newly observed magnetic field activity may be related to the energetic electron beams, but cannot be well explained using existing models.

FLARE EMISSION OBSERVED IN HIGH RESOLUTION AND COMPARISON WITH NUMERICAL MODELING

by
Nengyi Huang

A Dissertation
Submitted to the Faculty of
New Jersey Institute of Technology and
Rutgers, The State University of New Jersey – Newark
in Partial Fulfillment of the Requirements for the Degree of
Doctor of Philosophy in Applied Physics

Department of Physics

August 2020

APPROVAL PAGE

FLARE EMISSION OBSERVED IN HIGH RESOLUTION AND COMPARISON WITH NUMERICAL MODELING

Nengyi Huang

Dr. Haimin Wang, Dissertation Co–Advisor — Date
Distinguished Professor of Physics, NJIT

Dr. Yan Xu, Dissertation Co–Advisor — Date
Research Professor of Physics, NJIT

Dr. Dale E. Gary, Committee Member — Date
Distinguished Professor of Physics, NJIT

Dr. Wenda Cao, Committee Member — Date
Professor of Physics, NJIT

Dr. Lucia Kleint, Committee Member — Date
Head of the German Solar Observatory on Tenerife, Germany

Dr. Neepa T. Maitra, Committee Member — Date
Professor of Physics, Rutgers University - Newark

BIOGRAPHICAL SKETCH

Author: Nengyi Huang

Degree: Doctor of Philosophy

Date: August 2020

Undergraduate and Graduate Education:

- Doctor of Philosophy in Applied Physics,
  New Jersey Institute of Technology, Newark, NJ, 2020
- Master of Science in Applied Physics,
  New Jersey Institute of Technology, Newark, NJ, 2014
- Bachelor of Science in Physics,
  Jilin University, Jilin, Changchun, China, 2013

Major: Applied Physics

Presentations and Publications:

N. Huang, V. M. Sadykov, Y. Xu, J. Jing, and H. Wang. Comparison of Enhanced Absorption in He I 10830 Å in Observations and Modeling During the Early Phase of a Solar Flare. *The Astrophysical Journal Letters*, 879, L6, July 2020.

N. Huang, Y. Xu, V. M. Sadykov, J. Jing, and H. Wang. Spectral Diagnosis of Mg II and Hα Lines during the Initial Stage of an M6. 5 Solar Flare. *The Astrophysical Journal Letters*, 878, L15, June 2019.

N. Huang, Y. Xu, and H. Wang. Relationship Between Intensity of White-light Flares and Proton Flux of Solar Energetic Particles. *Research Notes of the American Astronomical Society (AAS)*, 2, 7, January 2018.

N. Huang, Y. Xu, and H. Wang. The Energetics of White-Light Flares Observed by SDO/HMI and RHESSI. *Research in Astronomy and Astrophysics*, 16, 177, November 2016.

Y. Xu, W. Pötzi, H. Zhang, N. Huang, J. Jing, and H. Wang. Collective Study of Polar Crown Filaments in The Past Four Solar Cycles. *The Astrophysical Journal Letters.*, 862, L23, August 2018

Y. Xu, W. Cao, K. Ahn, J. Jing, C. Liu, J. Chae, N. Huang, N. Deng, D. E. Gary, and H. Wang. Transient Rotation of Photospheric Vector Magnetic Fields Associated with A Solar flare. *Nature Communications.*, 9, 1-8, January 2018.

H. Wang, C. Liu, K. Ahn, Y. Xu, J. Jing, N. Deng, N. Huang, R. Liu, K. Kusano, G. Fleishman, D. E. Gary, W. Cao. High-Resolution Observations of Flare Precursors in the Low Solar Atmosphere. *Nature Astronomy*, 1, 1-6, March 2017.

N. Huang, Y. Xu, J. Jing, and H. Wang. High Resolution Post-flare Loop Observations by GST and IRIS. iPoster Presentation on American Astronomical Society/Solar Physics Division Meeting 50, St. Louis, MO, 2019.

N. Huang, V. M. Sadykov, Y. Xu, J. Jing, and H. Wang. Spectral Diagnosis of Mg II and Hα Lines during the Initial Stage of an M6.5 Flare. Oral Presentation on First Ten Years of Goode Solar Telescope Workshop, Newark, NJ, 2019.

N. Huang, V. M. Sadykov, Y. Xu, J. Jing, and H. Wang. Observation and Modeling of Mg II lines during an M6.5 Flare. Oral Presentation on American Astronomical Society/Solar Physics Division Meeting 49, Leesburg, VA, 2018.

N. Huang, Y. Xu, J. Jing, and H. Wang. Spectral Analysis Flare ribbons by NST and IRIS. Poster on American Astronomical Society/Solar Physics Division Meeting 48, Portland, OR, 2017.

N. Huang, Y. Xu, J. Jing, and H. Wang. Spectral Analysis Flare ribbons by NST and IRIS. Oral Presentation on Joint HINODE-11/IRIS-8 Science Meeting, Seattle, WA, 2017.

N. Huang, Y. Xu, and H. Wang. The Energetics of Wight-light Flares Observed in Visible Continuum and Hard X-ray. Poster on American Astronomical Society/Solar Physics Division Meeting 47, Boulder, CO, 2016.

以此献给我亲爱的家人
我的母亲，兄长和我的丈夫。
感谢他们全部的陪与一路的
陪伴，支持与鼓励，并日夜的
祷告。

以此纪念我亲爱的
父亲。

To my mother and brother,
who have been supporting me with all of their love,
and praying for me days and nights.

To my husband,
who has watched me succeed, seen me fail, kept me strong, and walked with me all the way.

And
In memory of my father.

ACKNOWLEDGMENT

I would like to express my deepest gratitude to my advisors, Dr. Haimin Wang, and Dr. Yan Xu. They have been helping me study, research, and write papers, and guiding me all the way. They taught me the knowledge and the way to learn; they helped me in research and became a researcher. Their patience and thoughtfulness have been keeping me positive through any difficulties. Their qualities as physicists have been encouraging me to work and learn. From them, I learned how to be a real researcher. Besides, through their support, I have opportunities to observe using GST in BBSO and attend meetings and present the works. I could not have imagined having better advisors for my Ph.D. study.

I sincerely thank all of my committee members for their time to attend my proposal and final defense, and for helping me in my writing of this dissertation. Thanks to Dr. Dale E. Gary for the brilliant thought and knowledge he shared in lectures and group meetings. Thanks to Dr. Wenda Cao for his support in data and his professional advice in observations in BBSO. Thanks to Dr. Lucia Kleint for her valuable help and suggestions for my researches and the questions she asked to keep me thinking. I thank Dr. Neepa T. Maitra for serving on my committee when I am really in need. And thanks for attending my dissertation proposal defense to Dr. Zhen Wu.

This dissertation was supported by NSF grants AGS-1539791, AGS-1821294, AGS-1954737, and by NASA grants 80NSSC17K0016, 80NSSC19K0257, 80NSSC19K0859.

I am deeply thankful to my collaborators, Dr. Ju Jing and Dr. Viacheslav M. Sadykov, for their labor in the papers presented in this dissertation. It was such a pleasure to work with them.

I am truly indebted to professors and students in the Center for Solar-Terrestrial Research, Drs. Chang Liu, Na Deng, Jeongwoo Lee, Bin Chen, Gregory D. Fleishman,

Gelu Nita, Sijie Yu, Shuo Wang, Zhicheng Zeng, Xin Chen, Natsuha Kuroda, Zhitao Wang, Xu Yang, Ms. Shaheda Begum Shaik, Ms. Dandan Ye, Mr. Jiasheng Wang, Yingjie Luo, Nian Liu, for the interesting talk and valuable discussions in seminars and group meetings. Especially thank Dr. Qin Li for his help and tips for dissertation writing.

I faithfully appreciate Mr. Claude Plymate, Mr. Nicolas Gorceix, Mr. Jeff Nenow, Mr. Sergey Shumko, Dr. John Varsik, and Dr. Vasyl Yurchyshyn for the technical support in observations using GST. And I would like to thank Ms. Erika Norro for her work during the time I was in BBSO.

My sincere gratitude also goes to the administrative staff in NJIT Physics Department, Ms. Cheryl E. James, Ms. Christine A. Oertel, Ms. Cindy Montalvo-Harden, Mr. Donald W. James III, and Ms. Leslie M. Williams, for their daily works to make my Ph.D. life easier. I want to thank the staff in the NJIT Graduate Student Office, Dr. Sotirios G. Ziavras, and Ms. Clarisa González-Lenahan for reviewing this dissertation.

It gives me great pleasure in acknowledging teams that provide data and technical support used in the dissertation: BBSO/GST, IRIS, RHESSI, SDO, GOES.

Last, but not least, I would like to thank all my family, friends, brothers and sisters in Lord. Thanks to them for always keeping me in their prayer. That is significant for my study, work, and entire life.

TABLE OF CONTENTS

TABLE OF CONTENTS
(Continued)

Chapter **Page**

LIST OF TABLES

LIST OF FIGURES

LIST OF FIGURES
(Continued)

Figure **Page**

LIST OF FIGURES
(Continued)

Figure **Page**

LIST OF FIGURES
(Continued)

Figure **Page**

LIST OF FIGURES
(Continued)

Figure **Page**

LIST OF FIGURES
(Continued)

Figure **Page**

LIST OF FIGURES
(Continued)

Figure **Page**

LIST OF FIGURES
(Continued)

Figure **Page**

CHAPTER 1

INTRODUCTION

1.1 The Sun and Solar Flares

The Sun, to the universe, is an inconspicuous star in the main sequence of Hertzsprung–Russell diagram. To the lives on the Earth, it is the closest star that provides light, energy, and other impacts on our planet. Solar activity certainly has significant impacts on the Sun-Earth environment, which is also known as space weather. The solar emission can change the density and temperature of the upper layers of the Earth's atmosphere. During the period of high solar activity, the increased air resistance can drag many satellites and, therefore, lower their orbits [145]. The energetic particles generated by flares and coronal mass ejections (CMEs) can cause more severe damage to the satellites and astronauts. Even more, solar activity can have a significant impact on the ground. For instance, on March 10th, 1989, an extremely violent solar eruption led to a geomagnetic storm, brought strong magnetic field and energetic particles, propagated to the Earth. As a consequence, power grids were damaged, and a wide range of outage occurred in the entire Quebec Province in Canada, as well as facility problems in other North America sites. Apart from this, the periodical evolution of solar magnetic fields is believed to have a close correlation with long term variation of terrestrial climate [66, 65, 169]. Therefore, studying solar activities powered by magnetic energies is crucial in plasma physics and astrophysics and has a profound impact on human lives. The close relationship of the Sun to the Earth has been motivating scientists to observe it closely. Being among the very typical main-sequence stars, the Sun is a unique approach that people can use to understand the remote stars in the universe. Astrophysicists have been taking advantage of this for the research of stars. Moreover, providing very extreme

conditions like high temperature and high pressure, the Sun is an advanced lab of plasma physics. Observations of the plasma in the solar atmosphere have been promoting several research fields in science.

The Sun is like a gas balloon filled with hot plasma 'floating' at the center of the solar system. Being on a focus of Earth's elliptical orbit, the Sun is approximately one astronomical unit ($1\ \text{au} \approx 1.496 \times 10^8\ km$) away from the Earth, varying between $(1.471 - 1.521) \times 10^8\ km$. One solar radius, defined as the radius of the solar photosphere, approximately equals to $7 \times 10^5 km$. The mass of sun is about $2 \times 10^{33}\ kg$ and the average density is $1.4\ g/cm^{-3}$. However, the Sun is not made with uniform plasma. Layers with different properties construct it.

1.1.1 Solar Activity

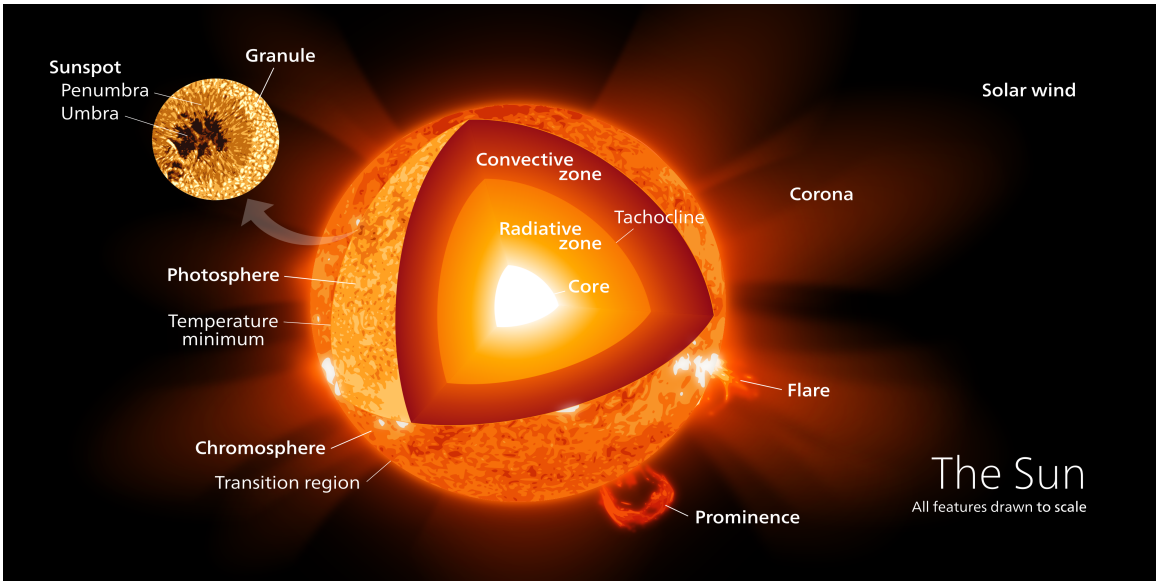

Figure 1.1 Structure of the sun in a cutaway view. Layers and phenomena on solar surface are identified with the labels.
(courtesy of WIKI user: Kelvin Ma)

The layers that form the Sun are very distinct by the temperature, density, motion, as well as their roles in the dynamics of the Sun. They can be divided into

the internal and external Sun, and these are well described by the widely accepted standard model.

The internal Sun is not observable because of its high opacity, but with the advanced observation of photospheric oscillation and the development of the helioseismology inversion method, the properties are calculated [100]. The internal Sun includes three zones: the core, the radiative zone, and the convective zone. In every second, there is about 3.845×10^{33} erg of energy released through the solar surface, of which 99% is generated by the nuclear fusion in the hot condensed core. The core is 1/5 to 1/4 of radius and about 1/50 in the volume of the Sun, but it has a very high density of 150 $g \cdot cm^{-3}$ and extremely high temperature of 1.57×10^7 K. Outside the core are the radiative and the convective zone. In the radiative zone, the density drops from over 20 $g \cdot cm^{-3}$ to about 0.2 $g \cdot cm^{-3}$ the temperature decreases from 7 MK to about 2 MK within the height from the top of the core to near 0.7 solar radii. The temperature gradient is too small to drive convection, and the energy is transferred by radiation. Meanwhile, in the convective zone from 0.7 radii to the bottom of the photosphere is a low-density plasma that provides conditions for convection. That is also where the solar magnetic field is majorly formed. A photon produced in nuclear fusions in the core would experience countless times of collision, absorption and re-emission, in these inner layers, before it reaches the first external layer, the photosphere [35].

The external Sun, also called solar atmosphere, is constructed by the photosphere, chromosphere and corona. Photosphere is the bottom layer of the solar atmosphere. It is the 'round plate' that people can see when they look at the Sun and thus identified as the surface of the Sun. Even though the thickness of this layer, 500 km, is only about $7 \times 10-4$ solar radii, it emits almost all the radiations on the visible continuum from the Sun. The typical number density is about $10^{12}/cm^3$. The bottom of the photosphere is commonly defined as the position where the optical

depth of 5000 Å equals 1 ($\tau_{5000} = 1$). In the quiet Sun, the temperature decreases with height in the photosphere. The minimum temperature is about 4170 K on top of the photosphere, also known as the 'temperature minimum region'. From the layer above this height to about 2000 km is called the chromosphere, even though the upper boundary is not well defined. The lower 1500 km is comparatively stable and uniform, while the higher part is composed of complicated structures like spicule, which is quite dynamic, even in the quiet Sun. Chromosphere has a lower density and higher temperature, comparing to the photosphere. Between the chromosphere and solar corona, there lies a very thin transition region. It is distinguished by the large temperature gradient. The temperature rises from about 20,000K at the top of the chromosphere to above 20 MK in corona, in only 100 km. The explanation of this dramatic temperature change, as well as the reason for such the high temperature in corona, are still under investigation. For corona, not like the layers mentioned above, it has no defined top. Instead, mass in the corona expands and flows over the entire space of the solar system via the solar wind.

Properties of the solar atmosphere do not stay the same. Instead, during solar activities, the energy released can strongly affect the chromosphere and change its properties, such as temperature, plasma density, electron density, velocity, etc. The atmosphere of the Sun is like an ever-bright city, where activities happen all the time. With long time-span observations, solar activity has been found to vary periodically, or known as solar cycles. The first scientific report of the solar cycle is by Schwabe et al. [155], who studied the number of sunspots from 1826 to 1843. Since then, studies of solar cycles have extended from sunspots to a variety of solar features, such as filaments, flares, radio flux, magnetic fields, CMEs, and galactic cosmic rays. The well-known 11-year cycle is defined by the sunspot number. Wolf el al. [183] defined an equation to describe the periodic sunspot number quantitatively,

$$R = k(10g + n), \tag{1.1}$$

in which R is the sunspot number, k is a correction factor for the observer, g is the sunspot group number, and n counts individual sunspots. Several sunspot archives are established, such as the International Sunspot Number and Boulder Sunspot Number, based on different observations and choices of the parameters.

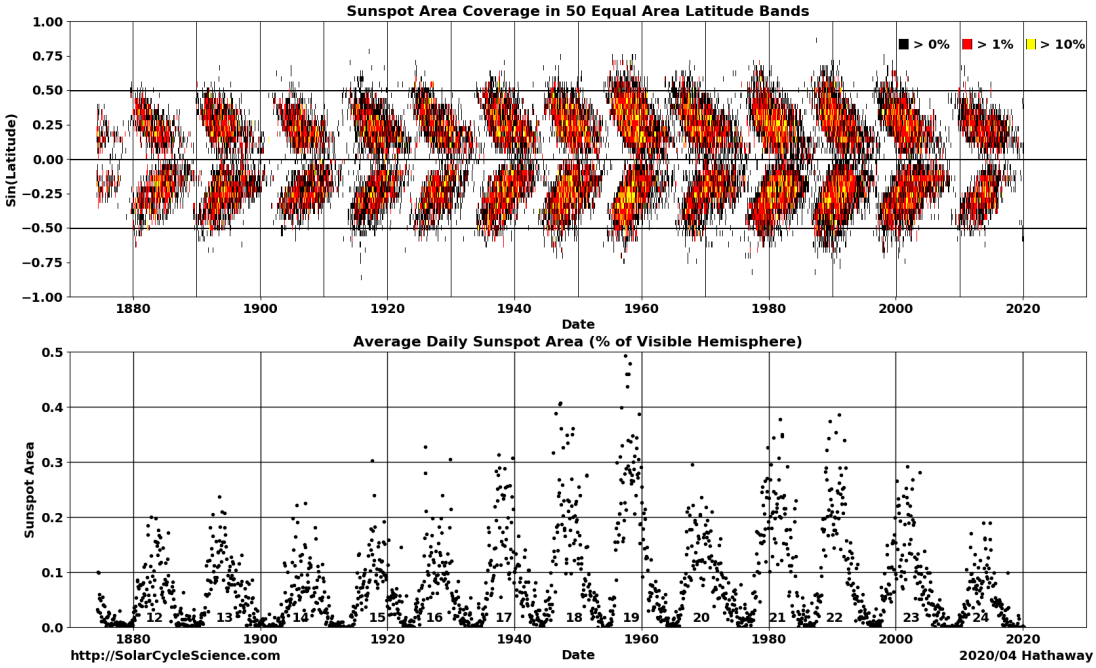

Figure 1.2 Uppper: Butterfly diagram showing area coverage of sunspots distributed on different latitudes varying over time since 1874. Lower: Time profile of percentage of sunspot area over solar disk.

Source: http://solarcyclescience.com/ accessed on July 7, 2020

Magnetic fields are the primary sources of solar features and activities. The generation and evolution of magnetic fields can be well described by solar dynamo, a combined model including Ω, α effects, and meridional flows [139, 160, 30]. The Ω, α effects describe the mutual relationship between poloidal and toroidal fields, which are the critical process in understanding the generation and emergence of bipolar magnetic regions. Upon decay, the leading polarity diffuses and drifts to the equator and cancels out with the opposite polarity in the other hemisphere. The trailing polarity travels a much longer distance to the polar areas driven by the meridional

flows and cancels out with residual fields of the previous cycle [180, 34]. In the convection zone, the buoyancy pushes the toroidal magnetic field up, and X-ray brightening would be observed when a magnetic field line is getting through the photosphere. The arch-shape magnetic field and frozen-in-field plasma form pores on the photosphere connected by an arch filament system and then develop into a sunspot pair. With the coexisting magnetic field lines, twisting, instability, and even reconnection can happen. A large scale of energy released by reconnection would lead to flare, CMEs, and solar energetic particle (SEP) events.

1.1.2 Solar Flares

Solar phenomena, including but not limited to sunspots, filaments, prominence, flares, coronal loops, CMEs, are extensively observed and studied. Solar flares are among the most violent activities, with energy release up to $10^{32} erg$ in a single event.

Table 1.1 GOES Flare Category

Class	*Peak Flux* $(W/m^2)^a$
X	$I > 10^{-4}$
M	$10^{-5} < I < 10^{-4}$
C	$10^{-6} < I < 10^{-5}$
B	$10^{-7} < I < 10^{-6}$
A	$I < 10^{-7}$

[a]The classification is based on the SXR peak flux in 1-8 Å.

Flares are classified with different methods, among which the Geostationary Operational Environmental Satellite (GOES [55]) classification is most commonly

used. According to the soft X-ray (SXR) peak flux in 1-8 Å measured by GOES, flares can be categorized into different groups: X-, M-, C-, B-, A-class, as shown in Table 1.1. The following digits describe the intensity levels of each group. For example, an M5.0 flare has a peak flux intensity of $5.0 \times 10^{-5} W/m^2$. The appearing frequencies are lower for higher level flares, and vice versa. Only six flares over X10 have been recorded since 1996.

A solar flare is originally defined as a sudden brightening in a well-defined area on the solar disk. Flares are usually associated with some other solar activities. Developed by Carmichael, Sturrock, Hirayama, Kopp and Pneuman [27, 161, 77, 98], the "CSHKP" model is well accepted and known as the standard model for interpretation of eruptive solar flares. In this model, the solar magnetic field over active region twists during the evolution and opposite direction field lines are pushed closer and closer until a reconnection happens. The magnetic energy stored in the solar corona is then released to drive explosive activities. In Figure 1.3, the upper panel is the sketch of this standard model. The reconnection releases a dramatic amount of energy in the current sheet and generates upward and downward flows, together with new arch-shaped magnetic field lines. The upward momentum can initiate filament eruptions, CMEs, or SEPs, and the downward component accelerates electron beams that precipitate along the reconnected magnetic field lines. In the lower panel of Figure 1.3, it shows the responsiveness of the lower atmosphere. High energy electrons move downward along the magnetic loops (or called flare loops) and heat the cool and dense plasma in the lower atmosphere, such as chromosphere or even photosphere. These processes generate hard X-ray (HXR) from bremsstrahlung, together with emissions like Hα from the activated plasma. The fast non-thermal electrons can even penetrate down to the upper photosphere and drive brightenings on the continuum, which could be identified as a white-light (WL) flare. On the other hand, emissions like SXR, extreme ultra-violet (EUV), and Hα emitted by the

plasma trapped in the arch-shaped loops also reveal the plasma motion in the flaring atmosphere.

However, the standard model left some questions unsolved. For example, the density of electrons in corona is lower than is required to activate the observed emission in HXR, and the mechanism that these electron beams can penetrate down to the lower chromosphere is unclear. The back-warming mechanism was developed to address the problem of depth that electron beam can penetrate [39, 82, 124], and Fletcher & Hudson [54] suggested a scenario that energy transported by Alfven wave accelerates electrons in chromosphere to ease the "number problem". These detailed supplements of the flare standard model were also widely supported by observation following the improvements of facilities [185].

1.1.3 Spectral Lines Emission

In the flaring atmosphere, the heated plasma not only enhances the emission of continua but also impacts the atomic lines. For example, Hα, produced by the transition of hydrogen atoms between $n = 3$ and $n = 2$, is a signature absorption line in the quiet Sun. During flares, the heated chromosphere turns it into emission from the lower chromosphere [105]. With known transition rates and statistical equilibrium equations, the intensity of the atomic lines can give hints to parameters like temperature, number density, the electron density in the chromosphere. Moreover, the asymmetry and broadening of its line profile can provide Doppler velocity information of the plasma.

Atomic lines, resulting from transitions between energy levels, are playing significant rules in the solar spectrum. Joseph von Fraunhofer first reported and mapped over 570 dark lines on the visible spectrum of the Sun, in 1814, and these lines were named Fraunhofer Lines afterward (Figure 1.4). These lines were identified as the absorption line of atoms in the solar atmosphere, except for a few telluric

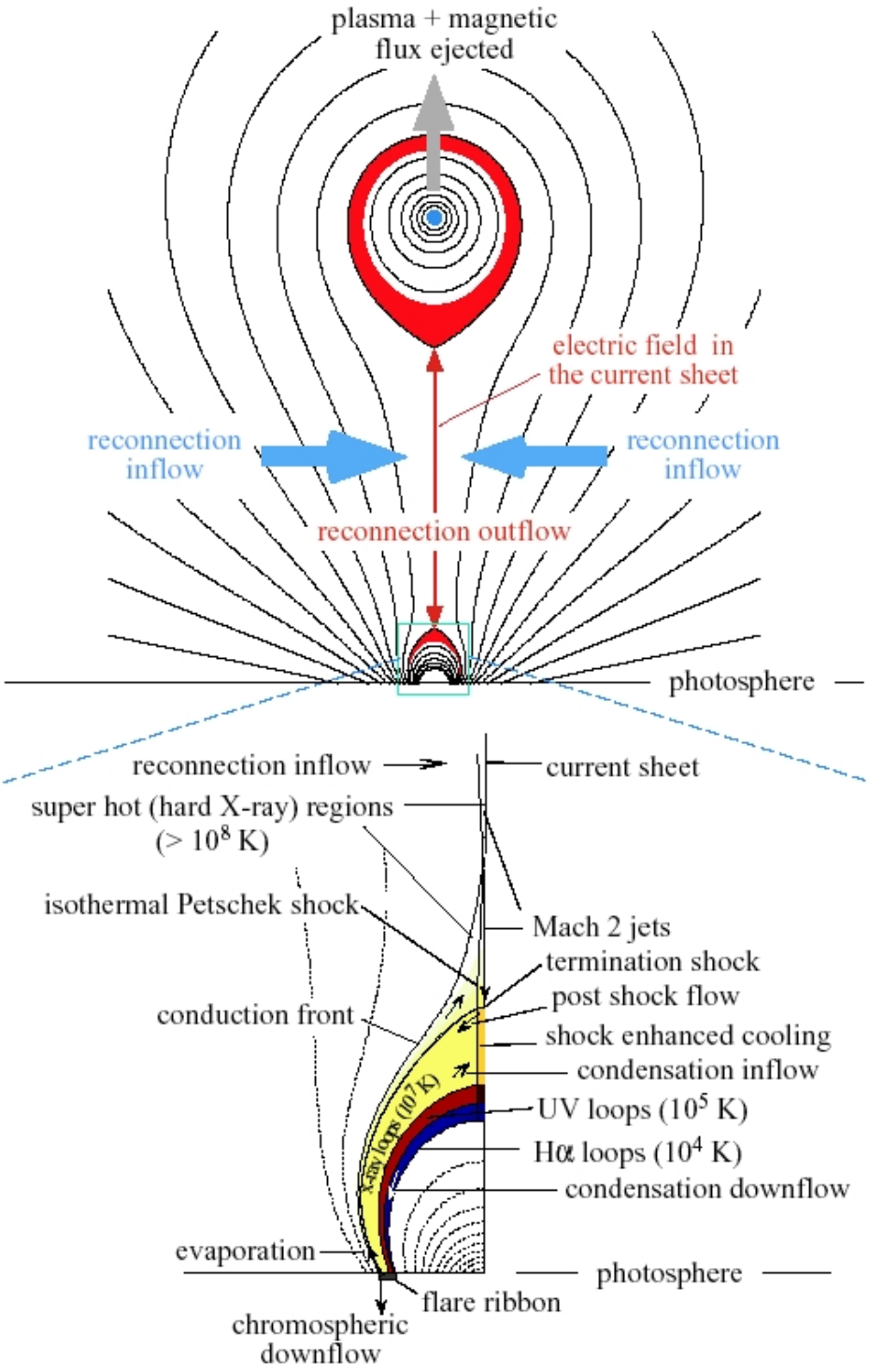

Figure 1.3 The upper panel: Sketch of the standard model of an eruptive solar flare. The lower panel: Enlarged image of lower solar atmosphere demonstrating the heating and flaring.
Source: Lin & Forbes [110]

contamination lines by the atmosphere of the Earth [95]. With updated observations, the number of lines was expanded to thousands over a broader wavelength range. These absorption lines are essential tools for solar physicists to understand the solar atmosphere. The depth, width, shifting of these lines provide hints of thermodynamic properties of the plasma.

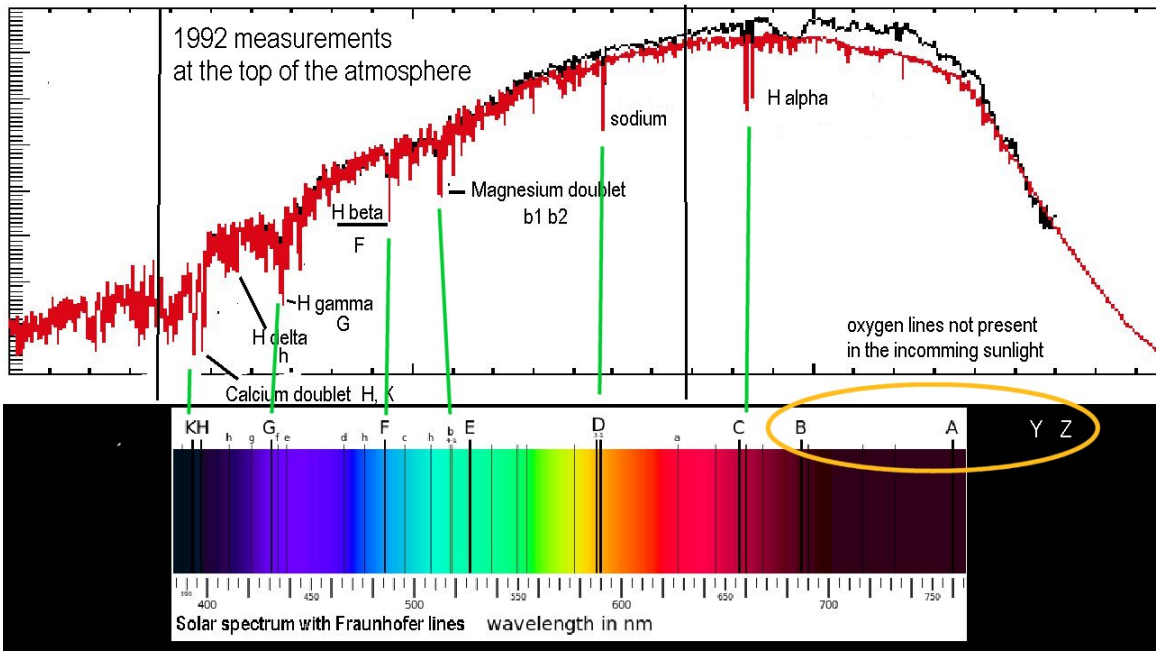

Figure 1.4 The Fraunhofer Lines over the solar spectrum near-visible light wavelength. Fraunhofer Lines were labeled with letters originally and identified as absorption by the solar atmosphere 45 years afterward.
Source: "Climate Change in the Sunlight" by Rolf A. F. Witzsche

The line intensity, either absorption or emission, is contributed by both radiative and collisional transitions. For any two energy levels, denoted by E_i and E_j (lower and higher energy), three radiative transitions should be included: spontaneous emission, induced emission, and absorption. The numbers of transition per unit time, volume, frequency interval, solid angle are described, respectively:

$$\frac{1}{4\pi} n_j A_{ji} \chi(\nu) \tag{1.2}$$

$$\frac{1}{4\pi} n_j B_{ji} I_\nu \psi(\nu) \tag{1.3}$$

$$\frac{1}{4\pi} n_i B_{ij} I_\nu \phi(\nu) \tag{1.4}$$

where n_i and n_j are number density of lower and higher energy level; A_{ji}, B_{ji} and B_{ij} are their Einstein coefficients, $\chi(\nu)$, $\psi(\nu)$ and $\phi(\nu)$ are the frequency distribution functions for the frequency ν, and I_ν is the intensity of radiation at frequency $\nu = (E_j - E_i)/h$. The line source function S_l is:

$$S_l = \frac{n_j A_{ji} \chi}{n_i B_{ij} \phi - n_j B_{ji} \psi} \tag{1.5}$$

In addition, the rate of collisional transition from lower to higher energy level (i to j) can be expressed in the way:

$$n_i C_{ij} = n_i n_e \int_{v_0}^{\infty} \sigma_{ij}(v) f(v) v dv = n_i n_e q_{ij}(T) \tag{1.6}$$

where $\sigma_{ij}(v)$ is the collisional cross section, $f(v)$ is the distribution of velocity, and $q_{ij}(T)$ is a function of temperature. These can be used as the expression of the line emissions, and plugged into the non local thermal equilibrium (non-LTE) equations.

1.2 Observations

The first observation of flare was back to September 1st, 1859, when Carrington first saw a WL flare that happened near a sunspot group [28]. However, flares were not very frequently observed until the 1930s when Lyot polarization interference filters were used in solar observations [115]. Up to the 1970s, following the improvement of technologies, both ground- and space-based telescopes, as well as higher resolution instruments, were developed.

1.2.1 Multi-wavelength Observations

Flares are observed over a broad electromagnetic spectrum, from nanometric gamma-ray to kilometric long-wave radio waves. However, different wavelength ranges have different transmittance. Some, such as EUV, is perfectly blocked by

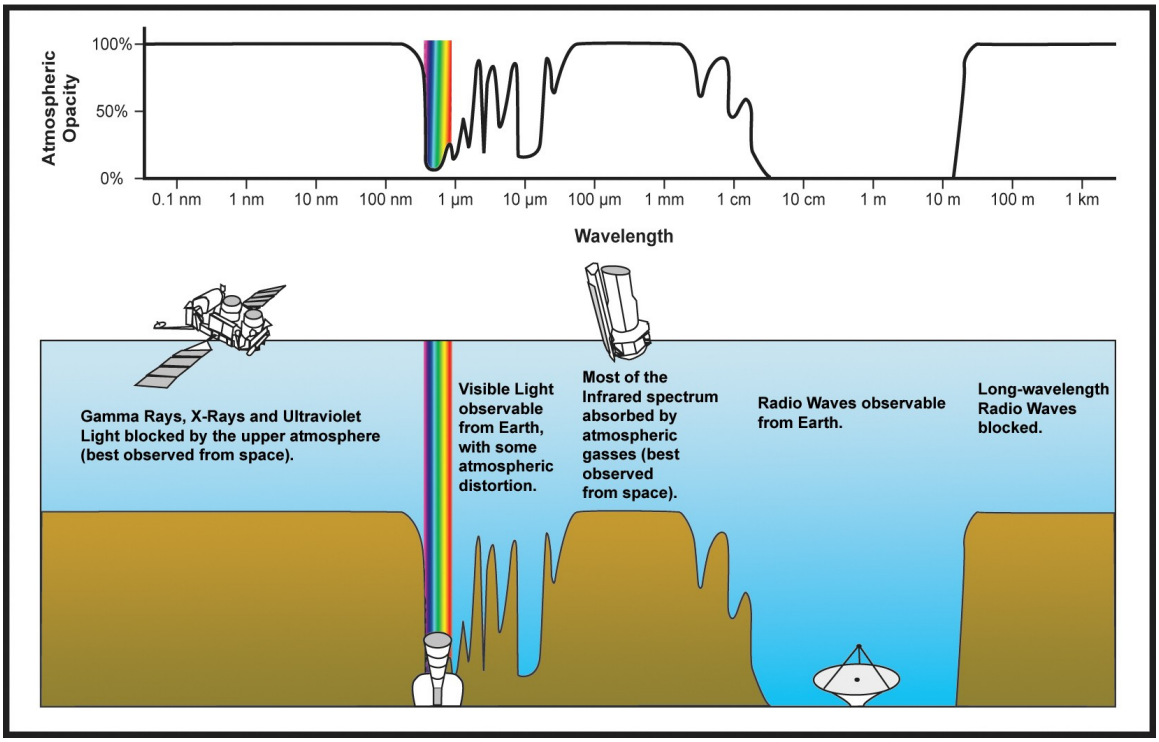

Figure 1.5 The transmittance of earth atmosphere to solar radiation. The opacity differs by the wavelength over the spectrum. Most parts of the spectrum are not observable on Earth, and thus space observations are applied. Radio wave range is widely observed on Earth because of the good atmospheric transmittance. Near to visible light ranges, the transparency of the Earth's atmosphere is good, but some perturbations may occur. So both ground and space-based observations are used. *(courtesy of NASA)*

the atmosphere of the Earth, while others, such as radio waves, are well transmitted to the ground. Figure 1.5 illustrates the transmittance of the Earth's atmosphere in different wavelength ranges. Figure 1.6 shows the spatially integrated evolutions of a typical flare observed in different wavelengths. Referring to the standard model of flare, these different types of radiation may be generated by different processes, while they are related to each other.

According to their optical properties to earth atmosphere, ground-based and space-based facilities are utilized for coverage of different wavelength ranges. For the spectrum with shorter wavelengths (as well as higher energy) than visible light, spacecraft are usually used. These are corresponding to the highest-energy particles, usually produced by the most energetic solar activities. At the shortest wavelengths, the *gamma-ray* is monitored by the GBM-9 of Fermi [12]. Most of the time, the Sun is faint over the gamma-ray wavelength range unless the charged particles are accelerated to near the speed of light and hit the solar atmosphere. With wavelength longer than the gamma-ray, radiation with energy higher than a few keV, called *HXR*, is very informative to studies of flare due to its direct relationship to the energy distribution of electrons and the energy deposit in the early phase. An HXR telescope onboarded Yohkoh worked for imaging of about 13 to 91 keV [137] until 2002 when the Reuven Ramaty High Energy Solar Spectroscopic Imager (RHESSI [111]) was launched, and spectroscopic images were available over 3 keV to 17 MeV range. RHESSI has spectral, spatial and temporal resolutions as high as 1 keV, 2 arcseconds, and 4 s, respectively. *SXR* has lower energy and longer wavelength than HXR, and its flux is used in classifying flare, as mentioned. SXR imagers on-boarded GOES satellite, GOES 12-15 SXI has been observing solar activities, especially flares since 2001. Most recently, GOES 16, which is also called GOES-R, use Solar Ultraviolet Imager (SUVI) with broader spectral coverage and higher spatial resolution as a

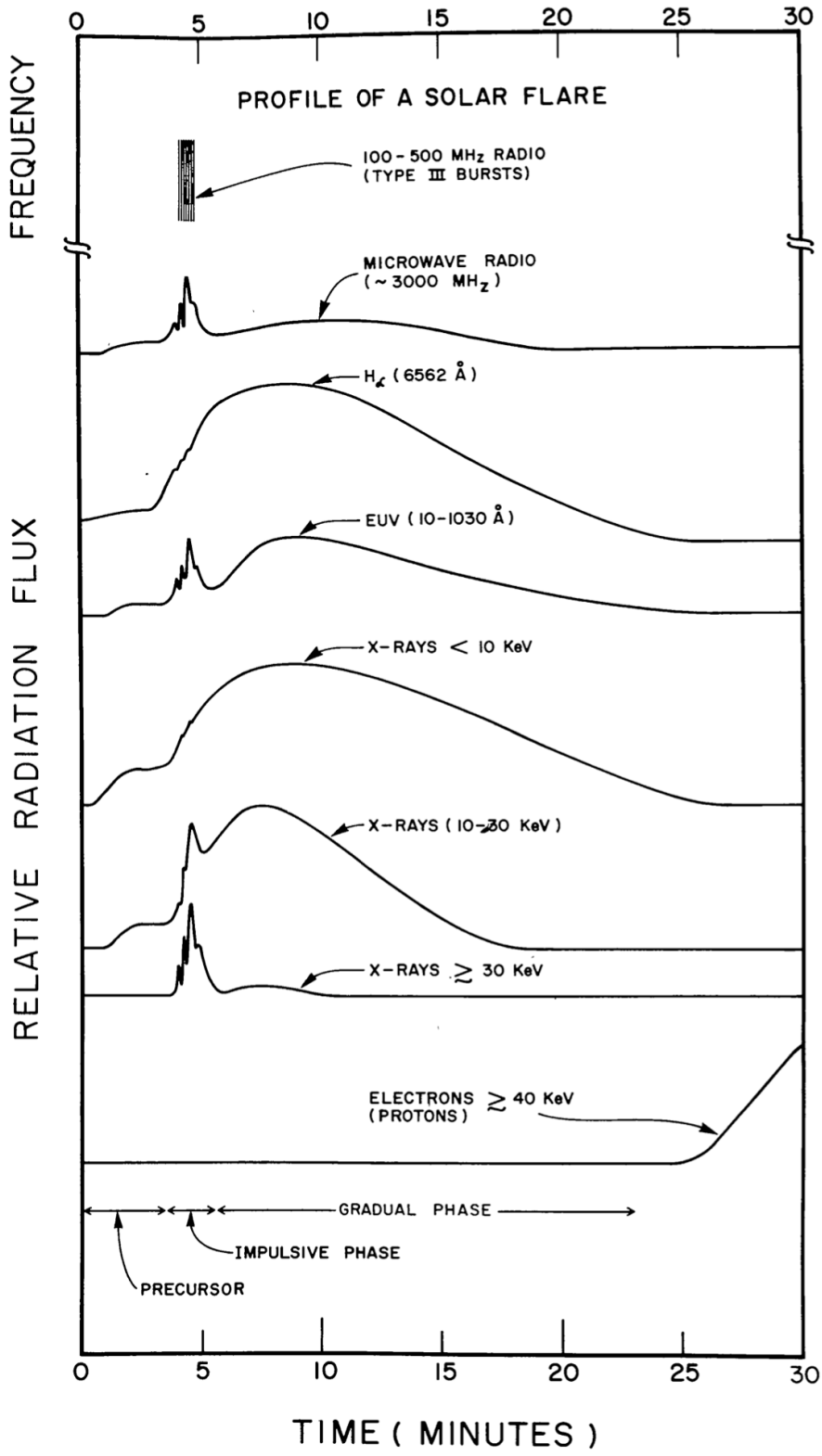

Figure 1.6 A schematic showing time evolution of a flare in different wavelength range.
Source: Kane 1974 [93]

replacement. Also, X-ray telescopes on Yohkoh and Hinode (XRT) provide SXR images from 1991 to 2001 and since 2005, respectively [59].

The *EUV* spanning over 100 Å to 1240 Å, and *ultraviolet(UV)* spanning over 1240 Å to 4000 Å spectra are mostly blocked by the Earth's atmosphere and thus require space-based observation as well. In earlier observations, narrow band (tens of Angstroms) images were recorded by space-based instruments like SUMER [182] and TRACE [67]. Afterward, Extreme Ultraviolet Imaging Telescope on Solar and Heliospheric Observatory (SOHO/EIT [37]) and Hinode provided images in 171, 195, 284 304 Å from 1995 to 2011. Then STEREO, launched in October 2006, consists of two satellites moving in orbits ahead (A) and behind (B) orbit of the Earth, was also equipped with Extreme Ultraviolet Imagers (EUVI) at the same wavelengths. Starting from March of 2010, the Atmospheric Imaging Assembly on Solar Dynamic Observatory (SDO/AIA [143]) started to provide images in 10 wavelengths in EUV, UV, and even visible continuum. Moreover, the space-based observations avoid the limitation from the night time and have good time coverage. These wavelengths are sensitive to temperature and responsive to activities.

Because of the good transmittance, solar observations in *visible light* and *near-infrared (NIR)* are usually carried out by ground-based telescopes. Although suffering atmospheric seeing conditions, the ground-based instruments still retain their advantages of availability of larger apertures and higher resolution limitations, not to mention the convenience of instrument maintenance and upgrading. Numbers of observatories and telescopes have been built for visible and NIR observation for over a hundred years. A more detailed description of the high-resolution ground-based observations in visible and NIR wavelengths is available in Section 1.2.2. Nevertheless, ground-based observations still have to face their limitations, such as local weather, seeing conditions, telluric contamination, and the restricted daylight time. Good

selection of sites, intelligent design of telescopes, and the advanced electronic control system were used to weaken the impact of some limitations.

The opacity of the *far-infrared* (FIR), over an extensive spectral range, is more complicated. When observation to spectrum around $10\mu m$ is available on Earth, the longer wavelength from hundreds of micrometers to one millimeter is only accessible in space. The longer wavelength makes FIR lines have better sensitivity to the magnetic field due to the more significant Zeeman splitting [36], but also produces difficulty due to the diffraction limit. In a broad frequency range from tens MHz to hundreds GHz (between a few millimeters and a few meters), the *radio* wavelength is covered by couples of imaging and non-imaging observations, such as Nobeyama [99]; Expanded Owens Valley Solar Array (EOVSA [87, 56]), Nançay [132]. The radio wavelength reveals thermal and non-thermal effects, which are closely related to a bunch of mechanisms in solar flares.

Other than imagers over different wavelengths mentioned above, spectropolarimeters were also used in solar observations to obtain magnetic field information through Zeeman or Hanle effect. Magnetic fields are related to all the solar phenomena, and thus the magnetograms are important tools for understanding solar activities.

Additionally, the particles, including energetic electrons, protons, and ions, are also captured by satellites. Solar winds and SEPs widely interest scientists because of their impacts on the Earth.

1.2.2 High-Resolution Observations: Instruments

The improvements of instruments not only benefit the observations in the better coverage of wavelength range and time but also in the higher spatial, temporal, and spectral resolutions. The enhanced spatial and temporal resolutions reveal a lot of fine structures to be investigated. In particular, we started to see tiny flare features

with imaging spectroscopic data. For example, Xu et al. [186] studied a flare observed in the NIR at 1.56 μm, which is believed to represent the deepest layer of the solar atmosphere and found non-uniform flare ribbon with distinct kernels embedded, which are named flare core and halo structures according to their brightness. The authors attributed direct heating and back-warming mechanisms to be the causes of core and halo emission, respectively. Note that the core areas are extremely concentrated, with a typical area less than 4 Mm^2. Many other studies [185, 92, 157, 101] presented narrow flare ribbons in the order of 100 km. At the same time, some of the fine structures in solar flares have a comparatively short lifetime and evolve rapidly. The utilizing of high-cadence ensures the observation and the reliability of comparison between their time profiles. Additionally, higher spectral resolution is available in the spectrographs. During flares, the solar atmosphere changes dramatically, and so do the profiles of spectral lines. With the high spectral resolution that provides detailed information of the line profiles, the spectrum lines can be powerful tools to diagnose the parameters such as velocity, density, and temperature.

Such high-resolution observations bring us closer to the fundamental features of solar flares and shed new light on flare studies. In the studies in this dissertation, some of the most up-to-date instruments were used.

Goode Solar Telescope: The ground-based has an obvious advantage in high-resolution observations. In the equation of the minimum resolvable angle due to the diffraction limit:

$$\theta \approx 1.22\frac{\lambda}{D} \tag{1.7}$$

λ is the wavelength, D is the aperture diameter, and θ is in the radiant unit. The resolution can be improved by increasing the size of the aperture. GST [60, 22], at Big Bear Solar Observatory (BBSO), equipped with a 1.6-meter clear aperture primary mirror and a high order adaptive optics (AO) system with a wave-front

sensor of 308 sub-apertures [61]. It can provide an image scale as high as 0″.08 per pixel at 5000 Å after proper speckle reconstruction. Currently, there are five mainly used imaging and imaging-spectroscopic instruments functioning on GST, namely: Broad-Band Filter Imager (BFI), Visible Imaging Spectrometer (VIS), Near Infra-Red Imaging Spectropolarimeter (NIRIS), Cryogenic Infrared Spectrograph (CYRA), and Fast-Imaging Solar Spectrograph (FISS). The capabilities of BFI, VIS, and NIRIS are listed in Table 1.2. FISS using 40″ spectrograph slit provides spectrographs typically at lines of Ca II, k line near 8540Å and Hα. The spectral resolution at Hα and Ca II lines are 0.05 and 0.06 Å. Besides, CYRA was newly developed to operates at wavelengths in 1-5 μm, which is the first fully cryogenic spectrograph. CYRA uses a grating spectrograph to obtain spectral profiles. The high resolution of GST allows it to observe the fine structure of flare, as well as the rare emission in visible and IR continua. Figure 1.7 is one of the examples of GST observations.

Interface Region Imaging Spectrograph: IRIS [144] is a space-based imaging solar spectrograph that launched in 2013. Some observational characteristics of IRIS instruments are listed in Table 1.8. Very high spatial and spectral resolution spectroscopic data and the corresponding slit-jaw images can be recorded simultaneously. The spectrograms are taken in spectral windows covering several lines in both near- and far-ultraviolet (NUV and FUV). The slit encompasses a field-of-view (FOV) of 175 ″, which can well-cover the major part of a typical solar flare. The spectrograph includes some lines such as O IV, Si IV, C II, and Mg II, whose behaviors in solar flares are very interesting, together with the slit-jaw images (SJI) taken in both NUV and FUV. These cover the depth from the bottom of the chromosphere to the solar corona. We use the database of IRIS as a resource of space observations on the UV wavelength. This spacecraft provides multi-wavelength images and spectra simultaneously focusing on the transition region to the corona. As seeing-free observation, IRIS data has well covered many solar flares since its first

Table 1.2 Characteristics of GST Imaging Instruments

Instrument	Available	Wavelength Bandpass (Å)	Image Scale (″/pixel)	Diffraction Limit (″)	FOV (″)	Cadence (s)
BFI	G-band	4305 5	0.027	0.067	55	15 (100frames)
	red-continuum	6684 4	0.034	0.093	70	15 (100frames)
	TiO	7057 10	0.034	0.093	70	15 (100frames)
VIS	Hα	6563 0.07	0.034	0.103	70	15 (11 lines * 25 frames)
	Fe I	6300 0.07	0.034	0.099	70	15 (11 lines * 25 frames)
	Na I D2	5890 0.07	0.034	0.093	70	15 (11 lines * 25 frames))
NIRIS	Fe I	15650 0.1 (doublet)	0.083	0.246	85	10 (full-Stokes)
	He I	10830 0.05 (multiplet)	0.083	0.170	85	10 (full-Stokes)

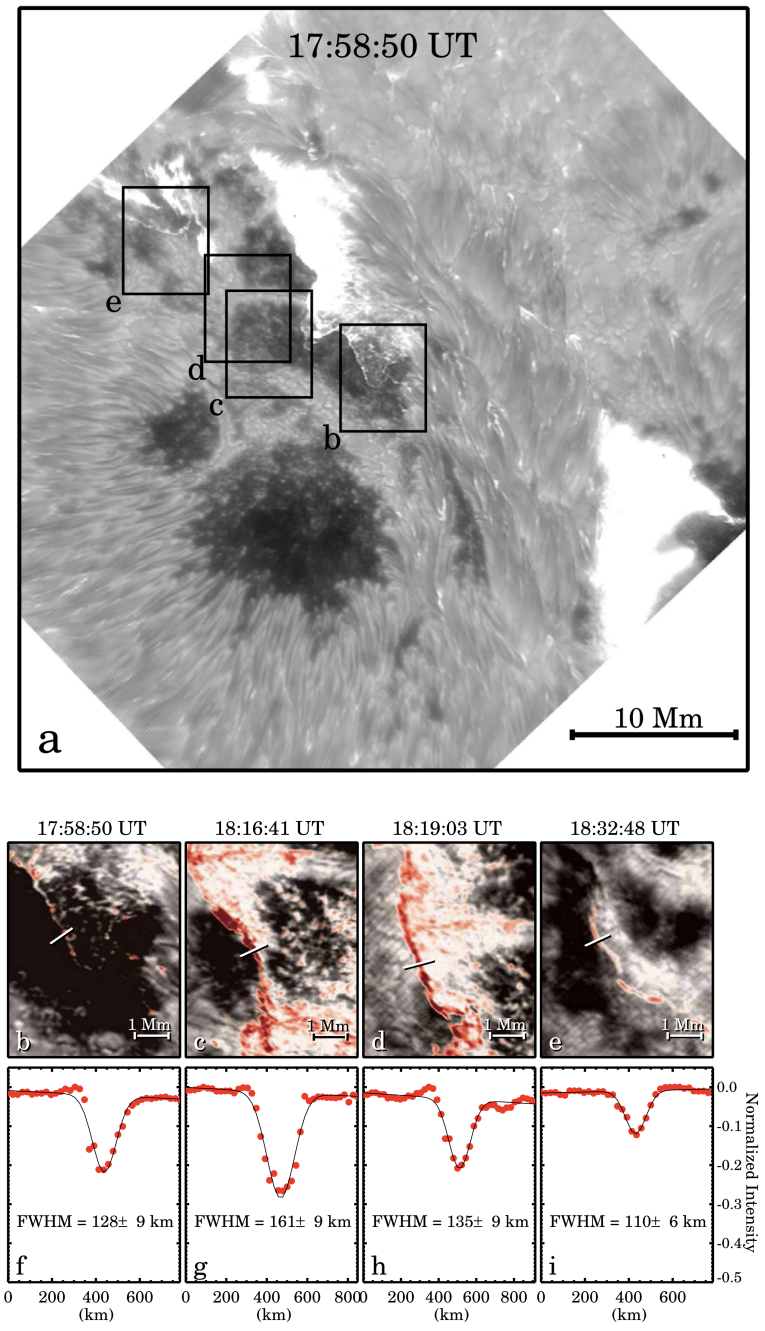

Figure 1.7 A sample of the fine structure of a solar flare observed by GST high-resolution observation. The panel (a) is an image of the flaring area during the impulsive phase, taken in Hα + 1.0 Å. Panel (f-i) are plots of pseudo Dopplergrams along the slits shown in panel (b-e), respectively. The distinct structure in the flare ribbon front is just over 100 km, which was not observable without high-resolution imagers.
Source: Jing et al. [92]

light. Figure 1.8 shows some samples of IRIS SJI and spectrograms. The upper panel is a NUV SJI taken at $\lambda = 2796\mathring{A}$, the vertical black line in the middle of which is the snapshot of the slit. The light passes through the slit and grating, then produces spectrograms. The lower panels are examples of spectrograms over wavelength windows close to Mg II h&k lines, C II 1335 Å lines and Si IV 1401 Å line. Thanks to IRIS's high spatial and spectral resolutions, distinct line profiles of small structures are observed in detail, such as a central-reversal in a strongly enhanced and broadened C II 1335 Å line from a small brightening point.

Table 1.3 IRIS Instruments Characteristics

Field of view	$175 \times 175\ arcsec^2$ (SJI)
	$0.33 \times 175\ arcsec^2$ (SG-slit)
	$130 \times 175\ arcsec^2$ (SG-raster)
Spatial scale (pixel)	0.167 *arcsec*
Spatial resolution	0.33 *arcsec* (FUV)
	0.4 *arcsec* (NUV)
Spectral scale (pixel)	12.8 $m\mathring{A}$ (FUV)
	25.6 $m\mathring{A}$ (NUV)
Spectral resolution	26 $m\mathring{A}$ (FUV SG)
	53 $m\mathring{A}$ (NUV SG)
Bandwidth	55 $\mathring{A}$ (FUV SJI)
	4 $\mathring{A}$ (NUV SJI)

Table Source: De Pontieu et al. (2014) [144]

Solar Dynamic Observatory: The SDO [143] is also a space-based observatory with three instruments onboard, and two of them provide high-resolution images: HMI and AIA. The HMI is dedicated to retrieving magnetograms of the

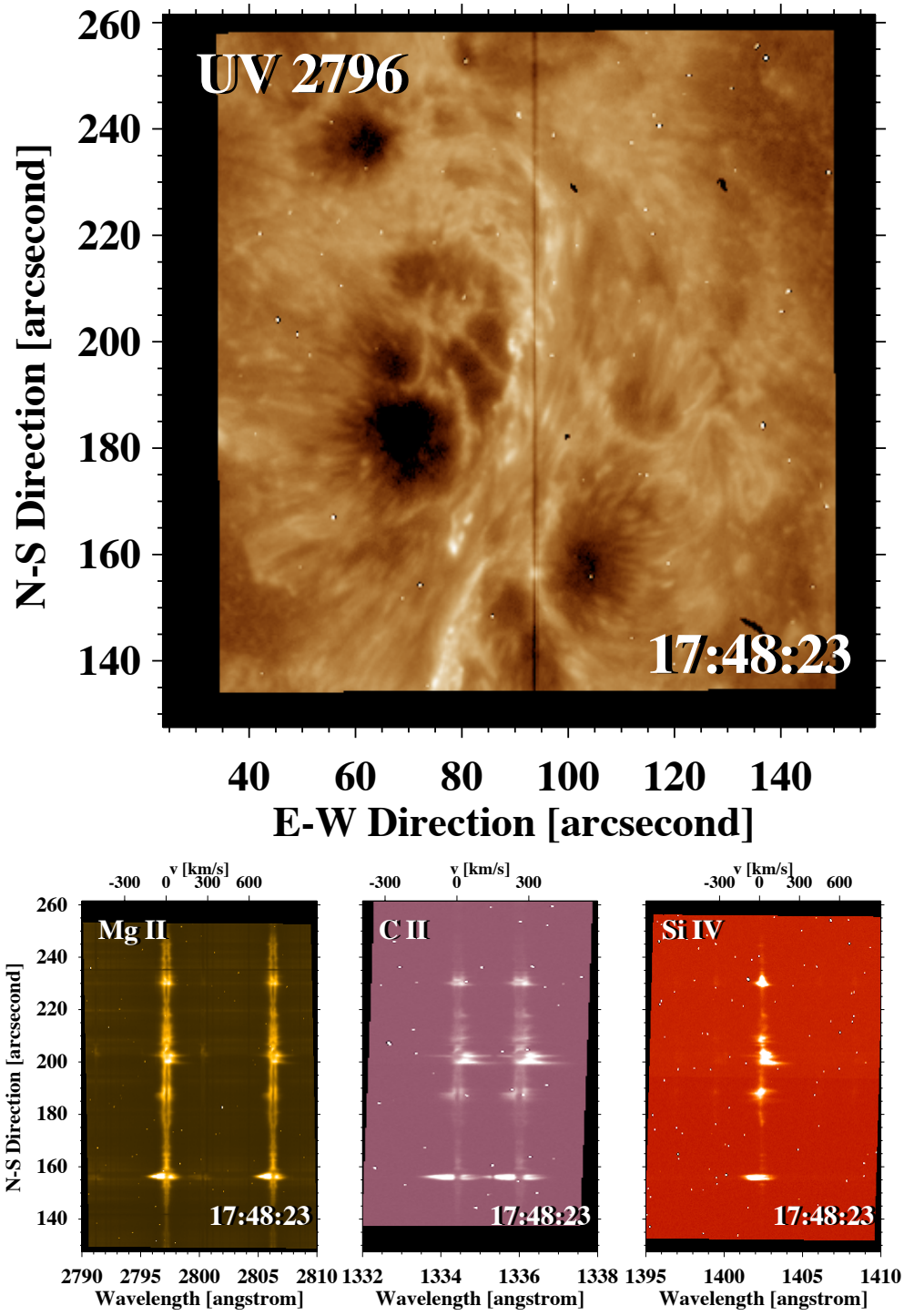

Figure 1.8 A sample of IRIS slit-jaw image, and spectrograms near Mg II 2796 Å, C II 1336 Å and Si IV 1403Å lines, at the initial phase of a flare.

photosphere using 6 points taken close to Fe I 6173Å. The continuum intensity images are also calculated using this data. AIA provides full-disk images in up to 10 wavelengths, covering wavelengths from 94 Å to 4500 Å, depth from the upper photosphere to coronal structures, and temperature from about 5000 K to 10 MK. SDO has the image scale as good as 0.5 and 0.6 arcsecond/pixel for HMI and AIA, respectively. Moreover, AIA has a cadence of 12s for most of the wavelengths.

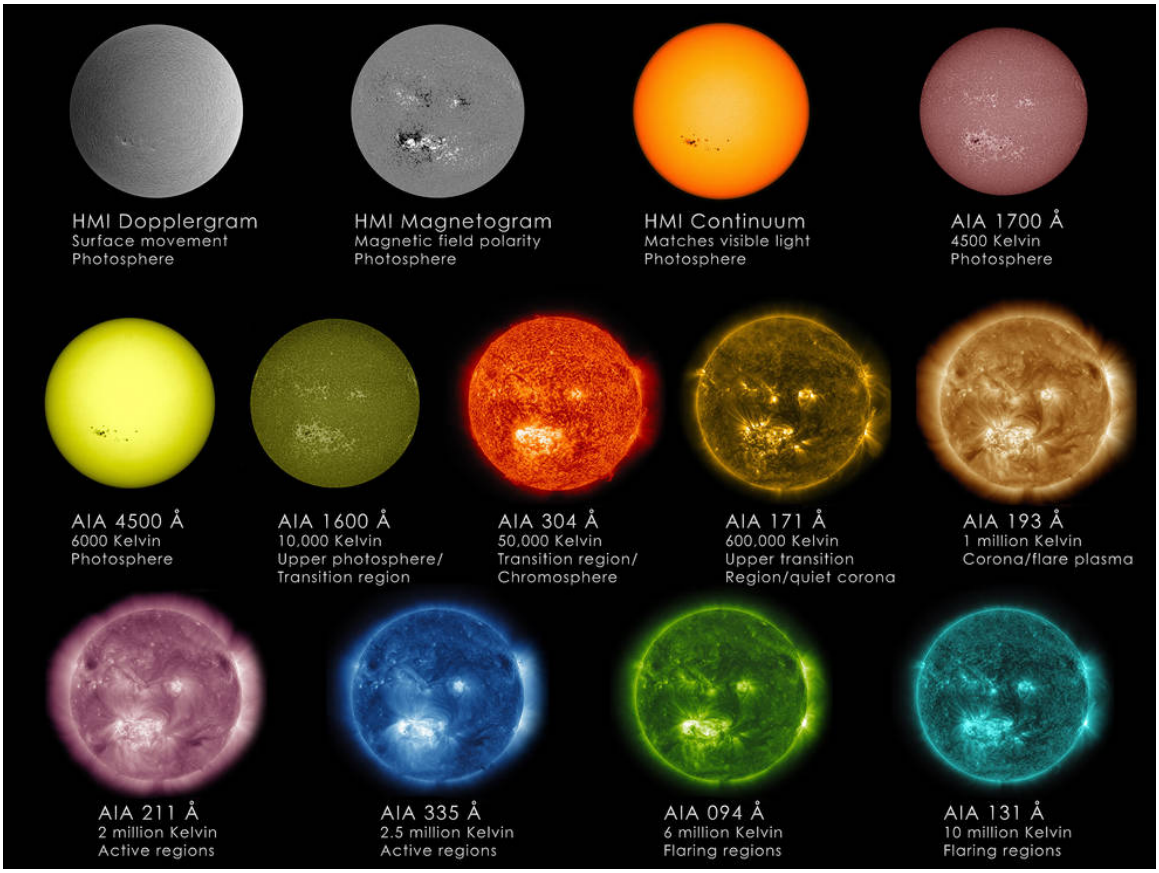

Figure 1.9 Images taken by SDO's instruments: HMI and AIA, in different wavelengths.
(courtesy of NASA)

Reuven Ramaty High Energy Solar Spectroscopic Imager: The RHESSI [111] observes the Sun, from SXR to gamma rays, was used due to the HXR images and spectra it performs. The spectrograph has a variety of spectral resolutions over the observed range. The spatial resolution is 2″, and the temporal resolution

is 4 seconds. However, both are able to be improved via computation. With classic assumptions of the accelerated electron beams' energy distribution, the HXR spectrum is a perfect tool for analyzing the electron in flares. To diagnose the electron beam properties by using the HXR data, we used the tool provided by the RHESSI team, **Object Spectral Executive** (OSPEX [156]), which includes multiple spectrum fitting models.

1.3 Modeling of Flaring Atmosphere

Following the availability of solar spectra, semi-empirical models of flaring solar atmosphere were proposed since the 1970s. With more lines and continua included, the model was furnished and became comprehensive [17, 73, 75]. Ever since Machado [116] published two chromospheric models of the solar flare, F1 and F2, the standard model of quiet-sun, VALC [171] and the other two flare models, F1* and F3 [1], were proposed to supplement. These models are all based on the assumptions of non-LTE and hydrostatic equilibrium, and computed by statistical balance function, radiation transfer function, and charge conservation function. The radiative hydrodynamic equations were in need of understanding the mechanisms of energy releasing and transferring in flaring solar atmosphere.

1.3.1 RADYN

With the fast progressing computational capability, Abbett [1] calculated the model of solar atmosphere hit by accelerated electron beam, via solving equations developed to describe the conservation of mass (Equation 1.8), momentum (Equation 1.9), energy (Equation 1.10) and the radiation hydrodynamics (Equations 1.11 and 1.12), by Carlsson & Stein[23, 24, 25]. This radiative hydrodynamic code was named **RADYN** afterward, and it was supplemented to include back-warming by X-ray and EUV in corona, which made it more comprehensive to modeling the flaring atmosphere and diagnosing the energy release mechanism [5, 6]. The RADYN code

simplified interaction between the lower atmosphere and the electron beam into a 1D motion along a symmetric arch-shape single loop. It adopted the classic VALC as the pre-flare atmosphere model and modeled the time-dependent hydrodynamic and radiative evolution of the atmosphere in response to the electron beam. It includes the continuum and spectral lines of H , Ca II, He and Mg II.

$$\frac{\partial \rho}{\partial t} + \frac{\partial \rho v}{\partial z} = 0 \tag{1.8}$$

$$\frac{\partial \rho v}{\partial t} + \frac{\partial \rho v^2}{\partial z} + \frac{\partial \left(p + q_v\right)}{\partial z} + \rho g - A_{beam} = 0 \tag{1.9}$$

$$\frac{\partial \rho e}{\partial t} + \frac{\partial \rho v e}{\partial z} + \left(p + q_v\right) \frac{\partial v}{\partial z} + \frac{\partial \left(F_c + F_r\right)}{\partial z} - Q_{cor} - Q_{beam} - Q_{rc} = 0 \tag{1.10}$$

$$\frac{\partial n_i}{\partial t} + \frac{\partial n_i v}{\partial z} - \left(\sum_{j \neq i}^{N'} n_j P_{ji} - n_i \sum_{j \neq i}^{N'} P_{ij} \right) = 0 \tag{1.11}$$

$$\mu \frac{\partial I_{\nu\mu}}{\partial z} = \eta_{\nu\mu} - \chi_{\nu\mu} I_{\nu\mu} \tag{1.12}$$

In these equations, g is the gravitational acceleration projection to the loop direction, and it equals to the gravitational acceleration in the lower atmosphere because of the large angle; t, z, ρ, e and v stand for time, height, density, internal energy density and velocity; p and q_v are pressure and viscous pressure, respectively. F_c and F_r are conductive and radiative fluxes, and Q_{cor}, Q_{rc}, Q_{beam}, and A_{beam} are heating terms added for coronal temperature, return currant, electron beam, and the momentum deposited by electron beam, respectively.

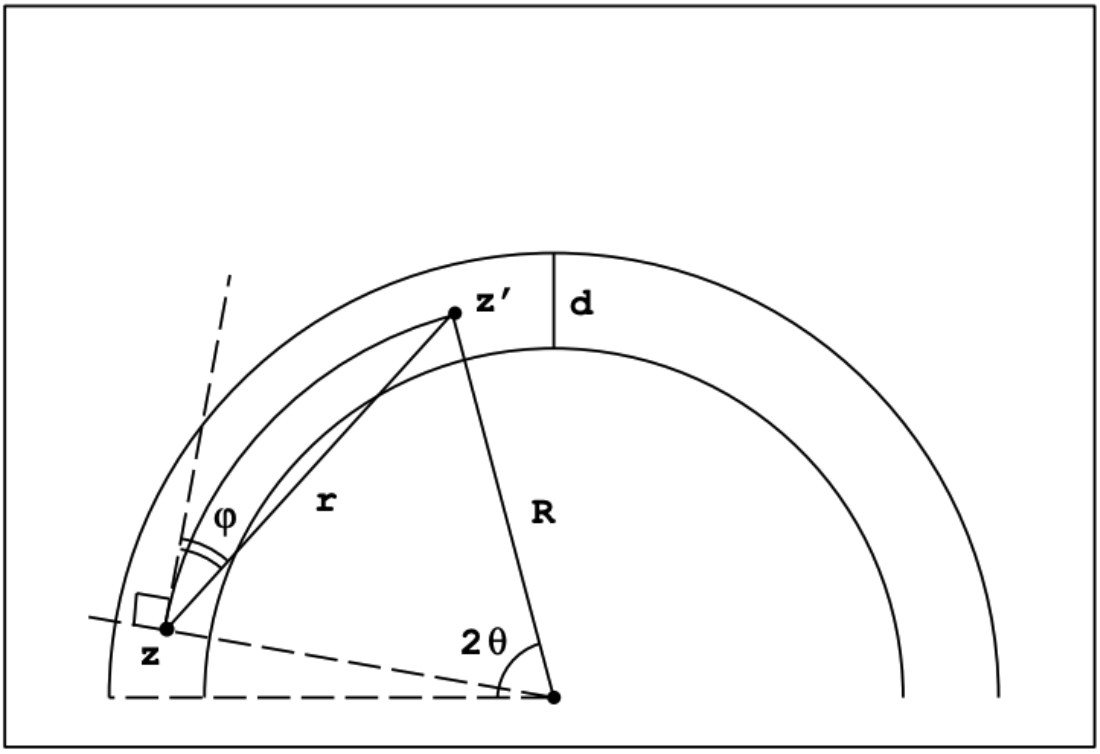

Figure 1.10 A sketch of the 1D single loop employed in RADYN model.
Source: Abbett 1999 [1]

The equations of radiation hydrodynamics, Equations (1.11) and (1.12), are referring to two states, i and j. n_j, P_{ij} and P_{ji}, are denoting the number densities and transition rates, where $P_{ij} = C_{ij}+R_{ij}$, and C_{ij} and R_{ij} are same as was described in Section 1.1.3. Distribution functions η and χ are also similar to the Section 1.1.3 part except for that the angle distributions are also considered here. ν stands for the frequency and μ for angle.

The energy deposition of the electron beam accelerated in the flare is modeled through adopting the Fokker-Planck function. It was assumed that the fast propagating electron beam distribution is time-independent. The distribution function, $f(E, \mu, z)$, where E is the kinetic energy, $\mu = \cos(\alpha)$ express the pitch angle, and z is

the 1D motion distance, can be solved in the 1-D Fokker-Planck equation:

$$\begin{aligned}
&\mu\frac{\partial\Phi}{\partial z} - \frac{d\ln B}{2dz}\frac{\partial}{\partial\mu}\left[\left(1-\mu^2\right)\Phi\right] = \\
&+\frac{1}{\beta^2}\frac{\partial}{\partial E}\left\{\left[C + S\beta^3\gamma^2\left(1-\mu^2\right)\right]\Phi\right\} \\
&+\frac{C'}{\beta^4\gamma^2}\frac{\partial}{\partial\mu}\left[\left(1-\mu^2\right)\frac{\partial\Phi}{\partial\mu}\right] + \frac{\Sigma}{c\beta^2} \\
&-\frac{S}{\beta\gamma}\frac{\partial}{\partial\mu}\left[\mu\left(1-\mu^2\right)\Phi\right]
\end{aligned} \tag{1.13}$$

where $\Phi = f/\beta$, $\gamma = E + 1$ is the total energy including relativistic effect, $\beta c = c(1 - 1/\gamma^2)^{1/2}$ is the velocity of the accelerated electrons, B is magnetic field, and Σ is injecting electron souces term. C, C' and S measure the energy loss, pitch angle scattering due to the collisions and energy loss due to the synchrontron emissions. They can be expressed as:

$$C = -\frac{dE_{col}}{dt}\frac{\beta}{c} \tag{1.14}$$

$$C' = \frac{\beta^2}{c^2}\frac{dv}{dt} \tag{1.15}$$

$$S = \frac{2}{3}\frac{(Ze)^4 B^2}{\left(mc^2\right)^3} \tag{1.16}$$

Through these terms, relativistic effect, Coulumb collision, pitch angle scattering are all considered.

F-CHROMA is a project that analyses the observations of flares and tests the models, emphasizing on the chromospheric part. Using RADYN simulations, this project prepared a database of flares driven by different electron beams. This great resource is available online (`http://www.fchroma.org/` accessed on July 7th, 2020).

1.3.2 RH

There are many approximations used in the RADYN code, and the frequency *complete redistribution* (CRD) is one of them. Recall the radiation transfer (Equations 1.2-1.5), and the line source function can be expressed using Einstein coefficients and

distribution functions. CRD assumes that the frequency distributions are equal in these processes:

$$\chi_\nu = \psi_\nu = \phi_\nu \tag{1.17}$$

However, this simplifying assumption only works well in limited conditions. For calculation of spectral lines, the emission and absorption profiles are not equal if there exits coherence scattering, then frequency *partial redistribution* (PRD) is in need. Especially for strong resonance lines, such as Ca II K line and Mg II h&k lines, the discrepancy between observed and CRD modeled line profiles are significant [127, 14, 107, 106].

RH is a stationary radiative transfer code that can calculate for PRD and solve the functions iteratively. It can solve the radiation transfer for a given atmosphere using PRD assumption, and calculated for specific atoms. With the capability to solve PRD functions, RH code is widely used for modeling of Ca and Mg emissions. Nevertheless, the RH code assumes statistical equilibrium since it is not time-dependent, and that may also cause a non-neglectable effect to the line profiles [26, 19].

1.4 Scientific Goal and Dissertation Outline

Ever since the first witness of solar flares, numbers of observations and studies have been carried out, as well as the theoretical and numerical modeling. However, there are missing pieces in the puzzle, and some of them are because of the limitations of observing instruments and computing power. One the one hand, the observations in higher resolution are opening access to the identification of smaller-scale structures, such as white-light flares kernels, which were hard to be observed previously. In particular, this reveals the non-uniform nature of flare ribbons. In addition, the use of advanced computation techniques allows a higher degree of freedom in modeling.

This work mainly focuses on the synthetic observations and numerical simulation of flare emission, to understand the flare energetics. High-resolution observational data from BBSO/GST and IRIS are mainly analyzed, together with supporting data obtained from SDO/HMI, SDO/AIA, and RHESSI. For numerical modeling of the flaring atmosphere and emissions, non-LTE radiative transfer codes, RADYN and RH, were used. The comparison between observations and modelings provides important clues in advancing our understanding of flare emission.

The relevant background knowledge, previous studies, and the motivation of this work are introduced in Chapter 1. Chapter 2 describes a statistical analysis of the energetic of WL emission in comparison with HXR radiations, which is a proxy of non-thermal electrons accelerated by magnetic reconnection. In Chapter 3, the correlation between WL flares and SEP events is investigated. In Chapter 4, A blue-wing asymmetric feature in Mg II h&k lines and red-shift in Hα line were observed in the front edge of flare ribbon, using IRIS and GST, and they are studied using radiative hydrodynamic codes RADYN. In Chapter 5, the absorption in He I 10830 Å line in leading flare ribbon edges, which was reported in previous studies, was numerical simulated using RADYN to reveal the atmosphere in the initial phase of the flare. Chapter 6 reported a newly observed transient rotation of the photospheric magnetic field, also in a narrow ribbon front. The summary of my Ph.D. work and preliminary plans for future research are shown in Chapter 7.

CHAPTER 2

THE ENERGETICS OF WHITE-LIGHT FLARES OBSERVED BY SDO/HMI AND RHESSI

WL flares have been observed and studied more than a century since the first discovery by Carrington [28]. However, some fundamental physics behind such energetic events remains highly controversial: such as the formation depth of WL emission and heating mechanisms. Previous observations have shown that the spatial and temporal correlations between WL emission and HXR radiation, suggesting that energetic electrons play an essential role in heating the lower atmosphere. In this chapter, we present a statistical analysis of 25 strong flares ($\geq$ M5), observed simultaneously by the SDO/HMI and the RHESSI. Among these events, WL emission was detected by SDO/HMI in 13 flares, which are associated with HXR emission. To quantitatively describe the strength of WL emission, equivalent area (EA) is defined as the integrated contrast enhancement over the entire flaring area. The results show that the EA is inversely proportional to the power-law index of HXR emission, suggesting that the level of WL depends on the population of electrons with higher energies. However, no strong correlation is found between WL emission and flux of non-thermal electrons at 50 keV. For the other group of 13 flares without detectable WL emission, the HXR spectra are softer (higher power-law index) than those flares with WL emission, especially for the X-class flares in this group. [1]

2.1 Introduction

WL flares are characterized by sudden emission in the visible continuum against the bright photospheric background. In the literature, they are always associated

[1]This chapter is based on the following paper: Huang, N.Y.; Xu, Y. & Wang, H., "The Energetics of White-light Flares Observed by SDO/HMI and RHESSI", *Research in Astronomy and Astrophysics*, 2016, volume 16, 177 [81]

with intense X-ray bursts and are thought to be classified in the top group of GOES classification at the first[134]. On the other hand, quantitative analysis of WL emission is subject to the limitation of observing techniques, for instance, the spatial-temporal resolution and the dynamic range of detectors. In fact, Zirin [197] and Neidig [133] have predicted that the WL emission might exist in all flares, but is detectable only at certain levels. This limitation was outstanding during the low-resolution observation era. With the rapid development of both space-based and ground-based instruments, WL flares are becoming more resolvable. Matthews et al. [121] surveyed observations of flares on G-band from Yohkoh and found flare of GOES class down to of C7.8 with brightening signals. Hudson & Metcalf [86] investigated flares observed by the Transition Region and Coronal Explorer (TRACE). By removing the UV line contaminations, the authors detected WL emission of a flare in GOES class of C1.6. Jess et al. [90] reported a C2.0 flare on 2007 August 24 with the high-resolution G-band observations carried out by the Swedish Solar Telescope (SST). The flaring area is very compact, but the contrast of WL emission was found to be 300% at its peak time compared to the quiescent background. Wang et al. [173] studied flares observed by Hinode and suggested that M1 class could be the lower limit for the flare with detectable WL emission observed by Hinode.

It is well accepted, as described in the standard model of flare, that the initial energy release occurs in the corona by magnetic reconnection, from which a tremendous amount of electrons are accelerated to near relativistic speeds. Part of these electrons penetrate downward along the magnetic field lines and generate various radiations, such as X-ray, microwave, and optical emissions [131, 82]. As first reported in the visible continuum, the term WL refers initially to the visible continua, which mainly comes from the photosphere. As time went on, solar observations cover to more spectral windows, then continua at UV and NIR were observed and included. Flaring emission at the NIR continuum, which is believed to reflect the opacity minimum,

was observed in an X10 flare [189]. The formation height and mechanisms of the WL emission remain highly controversial. Several models have been proposed to address these questions. For instance, the direct heating model indicates that the continuum emission is generated by the precipitating electrons via collision and ionization in the lower atmosphere [18]. However, considering the density and short collision range of the upper atmosphere, the electron energy for direct heating should be critically high: 350 KeV electrons can only precipitate to temperature minimum region [2]. Emslie [44] calculated the energies required for electrons to penetrate to certain layers and the corresponding densities. As a result, to heat the photosphere ($\tau_{5000} = 1$), the initial energy should be at least a few MeV. Moreover, to generate a WL flare, the needed total population of accelerated electrons would be higher than the affordable. This is a so-called "number problem". Nevertheless, the hypothesis of direct heating is not necessarily the only mechanism. A good alternative explanation is that the electrons stop, release their energies and heat the lower layer to power the continuum emission by back warming [117, 124, 40].

HXR bremsstrahlung radiation is a helpful tool to diagnose the electron beams. With well-accepted energy distribution of electrons in beams, where the thermal electrons follow the Maxwellian distribution and non-thermal electrons follow the power-law distribution, the HXR spectrum can reveal the electron energy distribution. At the same time, all the flare models assume that the WL emission is generated by accelerated electrons [84, 53]. The associations between WL and HXR during flares were proposed by Rust & Hegwer [152] and confirmed by observations in both spatial and temporal perspectives [135, 190, 86]. Therefore, a coordinated analysis of WL and HXR can reveal the mechanism of how these high-energy electrons should generate bursts of emissions. Battaglia & Kontar [15] compared EUV, WL and HXR emission of a limb flare using data from SDO/HMI, SDO/AIA, and RHESSI. They found that the EUV emission comes from higher layers (3 Mm from the photosphere) where

low energy electrons ($\sim$ 12 keV) deposit their energies. The HXR of 35-100 keV is suggested in lower layers in a range of 1.7 Mm to 0.8 Mm and the WL locates a little higher at 1.5 Mm. Martinez Oliveros et al. [118] related WL with HXR in a similar energy range of 30-80 keV. However, they found the formation heights were rather lower for both WL and HXR at 195 km and 305 km, respectively. Cheng et al. [33] further confirmed the temporal correlation between WL and HXR emission (26-50 keV) using SDO and *Fermi* data, respectively. Hao et al. [68] studied an M6.3 flare close to the disk center. Their results show a clear Balmer jump and classify this flare as a type I flare [48] with a direct link to electron precipitation.

Motivated by the above case studies, we attempted to relate the quantitative characteristics of WL and HXR emission **statistically**. Besides the total energy carried by accelerated electrons, the energy distribution of electron populations is very important and a key parameter for numerical simulations. By solving the radiative hydrodynamic equations, the atmospheric response to the precipitating electron beams can be simulated. The original idea was developed for stellar flare emission. Therefore this kind of simulations is simplified to deal with one-dimensional configurations (along the direction of flare loops). The input parameters can be assumed or derived from the HXR observations. Previous studies have matched the simulated results with the observed emission at a certain level [5, 31, 150]. Usually, HXR emission is composed of two components, thermal and non-thermal emission. The non-thermal emission, as mentioned, follows the power-law and can be described as one or more linear functions in a log-log plot. The slope of such a linear function, also known as the power-law index, is the crucial parameter in determining the contribution of the high energy electrons to the entire HXR emission. To quantitatively denote the WL emission strength, we followed the work of Wang et al. [173]. For each WL flare, they integrated the contrast over the areas of WL flare kernels and defined this quantity as equivalent area (EA), which describes WL

emissions' strength and extent. In this chapter, we present the investigation of a series of WL flares. Comparing and correlating WL and HXR emissions, we try to answer whether direct heating or back-warming dominates in powering WL flares.

2.2 Observations and Data Reduction

SDO [143] has been monitoring the Sun since its first light in 2010 and flying with three major experiments–HMI, AIA, and EUV Variability Experiment (EVE). Among those three, HMI provides full-disk maps of visible intensity and vector magnetograms. The intensity maps are obtained by taking six sampling points across the Fe I absorption line 6173.3 Å estimating the Doppler shift, linewidth, and line depth, then "reconstructing" the continuum intensity [154]. The effective cadence of the visible continuum images is 45 s, and the angular resolution is around $1''$. The RHESSI was launched in 2002 to explore hard X-ray (HXR) emissions during solar flares. It is sensitive to an energy range from 3 keV to 17 MeV with various energy resolutions and angular resolutions. The image cadence is usually 4 s, determined from the period of a full cycle of modulation. The Object Spectral Executive (OSPEX [156]) is a tool developed by the RHESSI team, which can calculate the spectrum from photon-count data and fit the spectrum into preset models to diagnose the electrons. In this study, we use SDO/HMI intensity images to retrieve the WL flare signals and use RHESSI HXR data plus OSPEX software for imaging and spectroscopic analysis.

Our targets are flares with WL emission observed by HMI WL channel and have coverage by RHESSI. Although it was predicted theoretically and confirmed observationally that the WL emission is a common feature not only for most violent events, it is still generally accepted that the more energetic flares are more likely to be associated with detectable WL enhancement. One of the reasons is that the detection of WL flares depends on the capabilities of instruments, for instance, the resolution and dynamic range. As listed in the introduction part of this chapter,

the studies using higher resolutions and dynamic ranges tended to find WL emission in flares in lower GOES classes. According to the instrumental conditions of HMI, we set a threshold of M5.0 to select events. In addition, to minimize the projection effect, near limb events ($\geq 50°$) are excluded. Besides, there are gaps of RHESSI observations, such as satellite night and South Atlantic Anomaly (SAA). Therefore, we need to eliminate the events which were not well-covered by RHESSI. In practice, we first selected all events covered by RHESSI and which occurred close to the disk center. During the period from March 2010 to June 2015, 25 flares satisfied with the criteria, including flares from GOES class of M5.1 to X3.1. Among these events, we observed that the WL signals were present not only in the strongest X-class but also in some of the M-class flares. Moreover, some X class flares do not have detectable WL enhancement signal. Therefore, we split the events into two categories, with and without WL emission, as shown in Tables 2.1 and 2.2.

For each event, we obtained a full-disk image sequence observed by HMI about 10 minutes prior to the HXR flux peak lasting at least 15 minutes. Then we zoomed in to the flare region with a small FOV, including the entire flare sources identified by HXR images. All the images are then aligned spatially using the first frame as a reference. Figure 2.1 shows an example of the X1.0 flare on 2014 March 29th, in the active region 12017. The upper panel presents an image taken at 17:41:46 UT, which is before the flare and used as the reference frame for alignment. In order to show the WL emission clearly, difference images are constructed by subtracting each image by the reference frame. This process requires a normalization of the image sequence. For this purpose, a quiet Sun area was selected, indicated by the white box, and the averaged intensity within this area is defined as the background I_b. Then the normalized images are obtained and the contrast defined by

$$Contrast = \frac{I - I_b}{I_b} \tag{2.1}$$

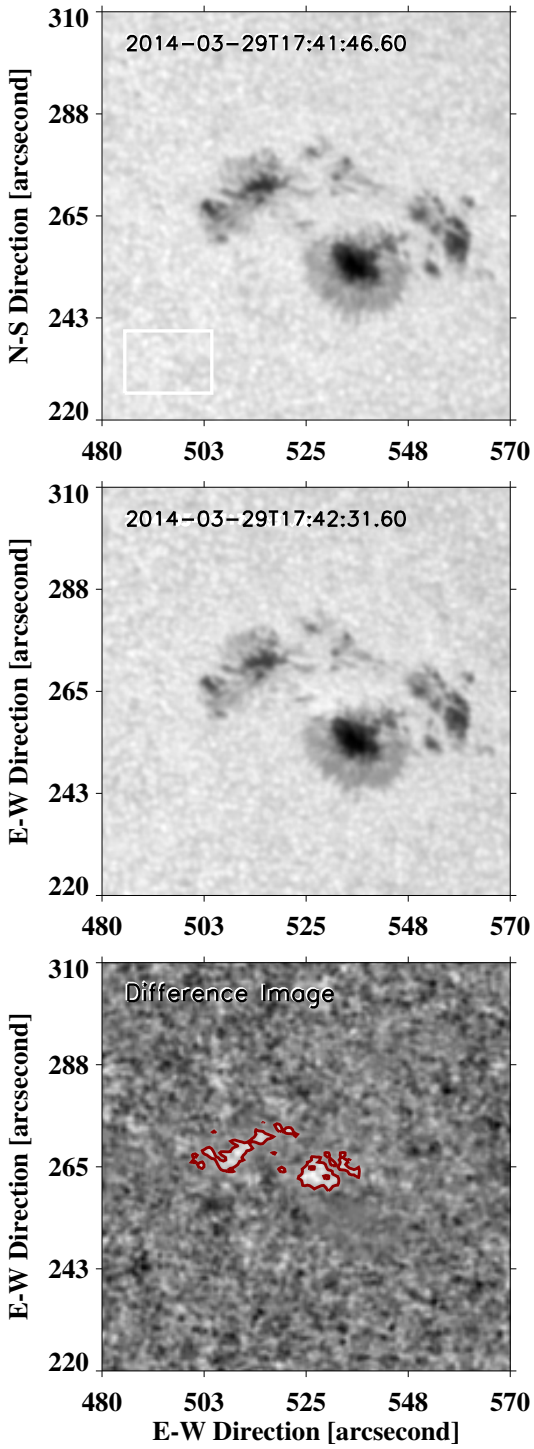

Figure 2.1 Image processing steps of an example event, X1.0 flare on 2014 March 29th. Upper panel: the pre-flare image of the active region, where the white box region was selected as the background. Middle panel: the flare peak image was taken 5 minutes prior to the WL flare peak. Lower panel: the difference image of the flare peak subtracting the pre-flare image, where the WL flare ribbons were shown in red contours. The total number of flaring pixels is 124, and the equivalent area is 3.20 arcsec^2.

is retrieved. In the middle panel of Figure 2.1, it is an image during the peak of that flare. A very weak brightening can be seen around the center but not significant. More obvious flare sources are obtained by the difference images, shown in the lower panel which are outlined by red contours. We used the running difference image, and manually set thresholds for the WL flare kernels, which can be identified visually. Therefore, only the intense flare cores are included in our analysis.To quantitatively describe the WL emission, the equivalent area (EA) is defined by integrating the contrast enhancement (E) over the entire flaring area (A) [173]:

$$EA = \oint_A Contrast\ d(A) \tag{2.2}$$

The flaring area is found by contours of 3 times of standard deviations above a background threshold. As an example, the EA for the 2014-03-29 event is 3.20 arcsecond^2. The results of all WL events are listed in Table 2.1.

HXR spectra around the peak time of WL emissions were then constructed using the default setups of RHESSI with pileup correction, as all of the events are stronger than M5.0. For events without detectable WL emission, the flare peak times were defined as the maxima in 25-50 keV HXR emission. The spectral fitting involved two models, the variable thermal (vth) and the broken power-law (bpow), in which the former represents the thermal HXR component usually in low energy ranges, and the latter represents the non-thermal component. The non-thermal component usually represents the high energy component and correlates with WL and HXR emissions at footpoints. The representative parameter of the non-thermal component is the power-law index, which is the absolute value of the fitted line slop in log-log space. In principle, a low value of power-law index refers to as 'harder' HXR spectrum with more electrons populated in high energy tail, and a high power-law index indicates a 'soft' HXR spectrum with more electrons in the low energy ranges. Figure 2.2 shows a

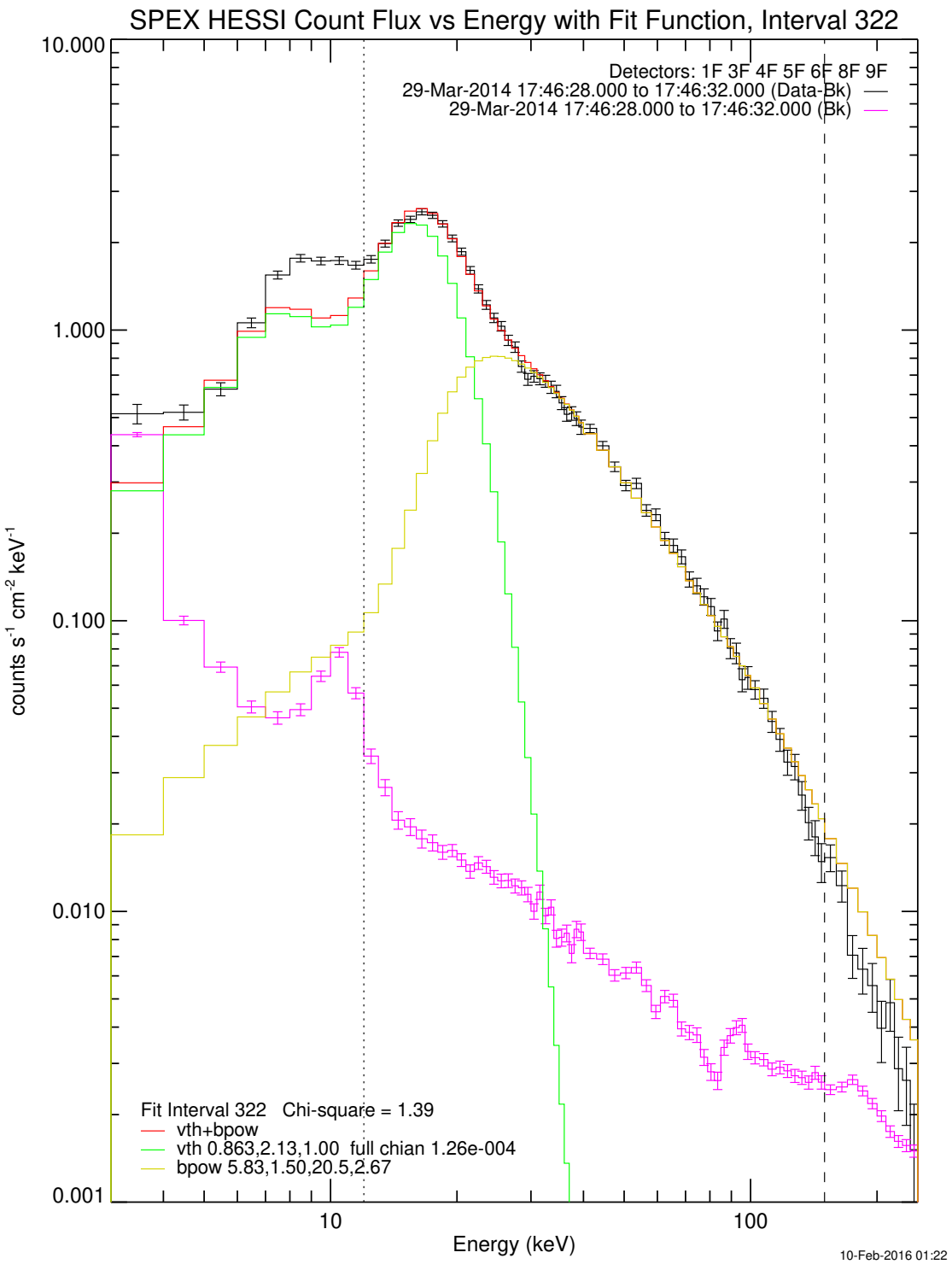

Figure 2.2 Fitting of peak spectrum of the sample flare on 2014 March 29th, using two components of Variable Thermal and Non-thermal broken power law. The black curve is the spectrum data after subtracting the background (pink). The modeled thermal component, non-thermal component, and the overall spectrum are plotted in green, yellow, and red, respectively.

sample spectrum of the sample event of flare in 2014-03-29. The power index for that event is 2.67. The power-law index change during the flare, and while the hardest spectrum usually occur close to the WL emission peak (as is shown in Figure 2.4). The smallest power-law index near the WL emission peak time was taken as the power-law index for that flare. The power indices for all of the 25 events are listed in Tables 2.1 and 2.2.

Table 2.1 Properties White-Light Flares

Date	Time	GOES	AR#	Location	Equivalent Area	HXR Spectral Index
2011.02.15	01:43	X2.2	11158	S21W12	1.45	5.30
2011.07.30	02:04	M9.3	11158	N16E32	5.55	4.84
2011.09.06	22:08	X2.1	11283	N16W15	6.31	2.88
2011.09.08	15:32	M6.7	11283	N14W41	0.95	2.79
2012.07.04	09:47	M5.3	11515	S16W15	1.42	3.45
2012.07.05	11:39	M6.1	11515	S17W30	1.20	2.99
2013.11.10	05:07	X1.1	11890	S13W13	2.34	3.98
2014.01.07	10:07	M7.2	11944	S13E13	2.52	3.65
2014.03.29	17:35	X1.0	12017	N10W32	3.20	2.67
2014.10.22	14:02	X1.6	12192	S14E13	0.87	4.46
2014.10.24	21:07	X3.1	12192	S12W31	0.71	6.25
2015.03.10	03:19	M5.1	12297	S15E39	0.83	2.99
2015.03.11	16:11	X2.1	12297	S17E22	1.15	4.33

2.3 Results and Discussion

Among the 25 events, 13 of them are companioned by WL flare signals, and the other 12 are not. Figure 2.3 shows the scatter plot of the WL EA vs. HXR power

Table 2.2 Properties of Flares without White-Light Emission

Date	Time	GOES	AR#	Location	Spectral Index
2011.02.13	17:28	M6.6	11158	S19E01	5.05
2011.03.09	23:10	X1.5	11166	N10W11	5.91
2011.09.25	04:31	M7.4	11302	N12E45	4.25
2012.03.09	3:22	M6.3	11429	N17W01	5.17
2012.05.10	04:11	M5.7	11467	N10E20	3.84
2012.07.12	16:28	X1.4	11520	S20W03	7.61
2014.01.01	18:40	M9.9	11936	S16W45	9.40
2014.04.18	12:50	M7.3	12036	S15W35	2.77
2014.10.22	01:16	M8.7	12192	S13E21	4.02
2014.10.25	16:55	X1.0	12192	S12W31	7.73
2014.12.04	18:05	M6.1	12222	S20W34	5.84
2014.12.18	21:58	M6.9	12242	S18W26	4.07

index. The red dots represent the X-class flares, and the green dots indicate the M-class flares. In principle, we see a correlation between the EA and the power-law index. The flares with smaller HXR power-law index, which is to say that the HXR spectrums are harder, tend to have larger EA in the WL flare ribbons. The solid line denotes the trend for all the events, and the dotted line denotes the trend for X-class flares only. According to the trend of X-class flares, the **negative correlation** between WL strength and HXR power index is more significant. The comparison of EA of WL flares and HXR power index shows that flares with smaller hard X-ray indices tend to have larger equivalent areas. On the other hand, we notice that the HXR spectra are somewhat harder, with spectral indices smaller than 4, of all the M-class flares with WL emission shown in this study. We suspect that other M-class flares with relatively higher power index do not have detectable WL emission and are excluded from the analysis. Therefore, this selection effect is one of the reasons why the negative correlation between the power-law index and EA is not as evident for the M-class flares. As we mentioned in the introduction section, the power index effectively denotes the population of high-energy electrons in general. Therefore, the negative correlation between the EA and power index indicates that the high-energy electrons play a significant role in generating the WL flares, especially for strong (X-class) flares. This result is in favor of the direct-heating model, which requires electrons to have high energy to penetrate down to lower atmosphere and deposit their energy by collision.

In addition to the multiple events analysis for the WL and HXR emission correlation, the temporal variations of WL emission and HXR power index are retrieved and compared. For each event, over a time range covering the peak of WL emission, the HXR spectral power-law indices were calculated for selected time-stamps. RHESSI has a higher time cadence than SDO/HMI, and thus we selected the RHESSI data point based on SDO timing. Figure 2.4 shows the time

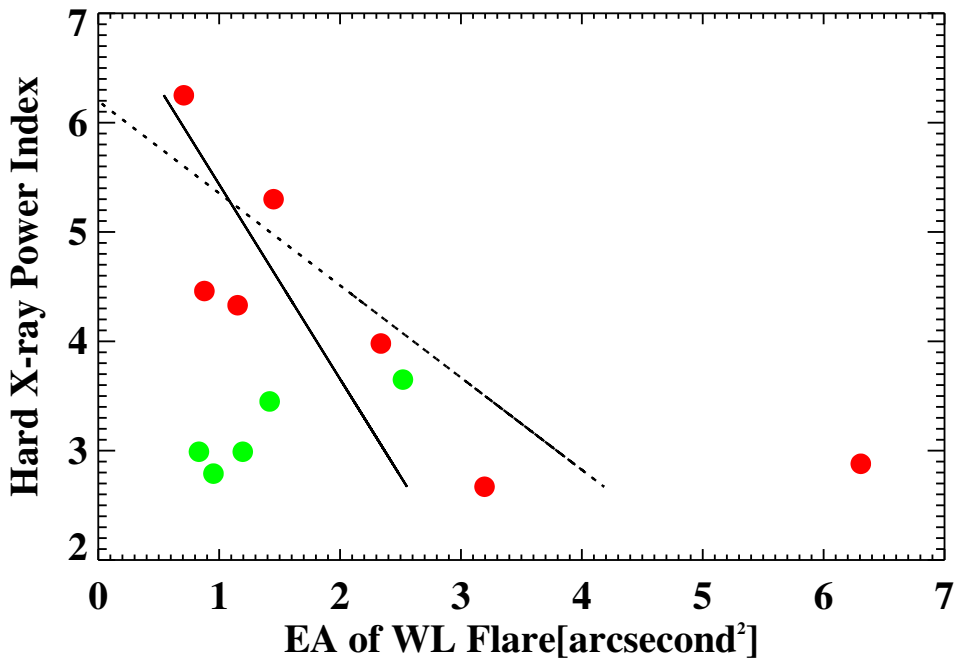

Figure 2.3 Plot of *equivalent area of WL flare source* vs *hard X-ray power index*. The solid line shows the trend of linear fitting for all events. A negative correlation is obviously seen (the lower the power index, the larger the EA of WL). The red dots represent the X-class flares, and the green dots indicate the M-class flares. The dotted line denotes the trend for X-class flares only.

evolutions of WL and HXR emissions fluxes and HXR power index during a sample flare on 2014-03-29. The solid black plot shows the light curve of WL emission, the dotted line shows the power index evolution, and red and green lines plot the time profiles of HXR fluxes in energy ranges of 50-100 keV and 100-250 keV, respectively. We see that the WL and HXR fluxes are temporally correlated as expected. There is a negative correlation between the WL emission and the power-law index, which is typical for all the WL flares in our list.

Furthermore, the correlation between WL intensities and HXR fluxes for those WL flares is investigated. Figure 2.5 is the scatter plot of WL EAs and HXR peak fluxes at 50 keV. The red dots represent the X-class flares, and the green dots represent the M-class flares. The correlation between EA and HXR flux is not as clear, based on

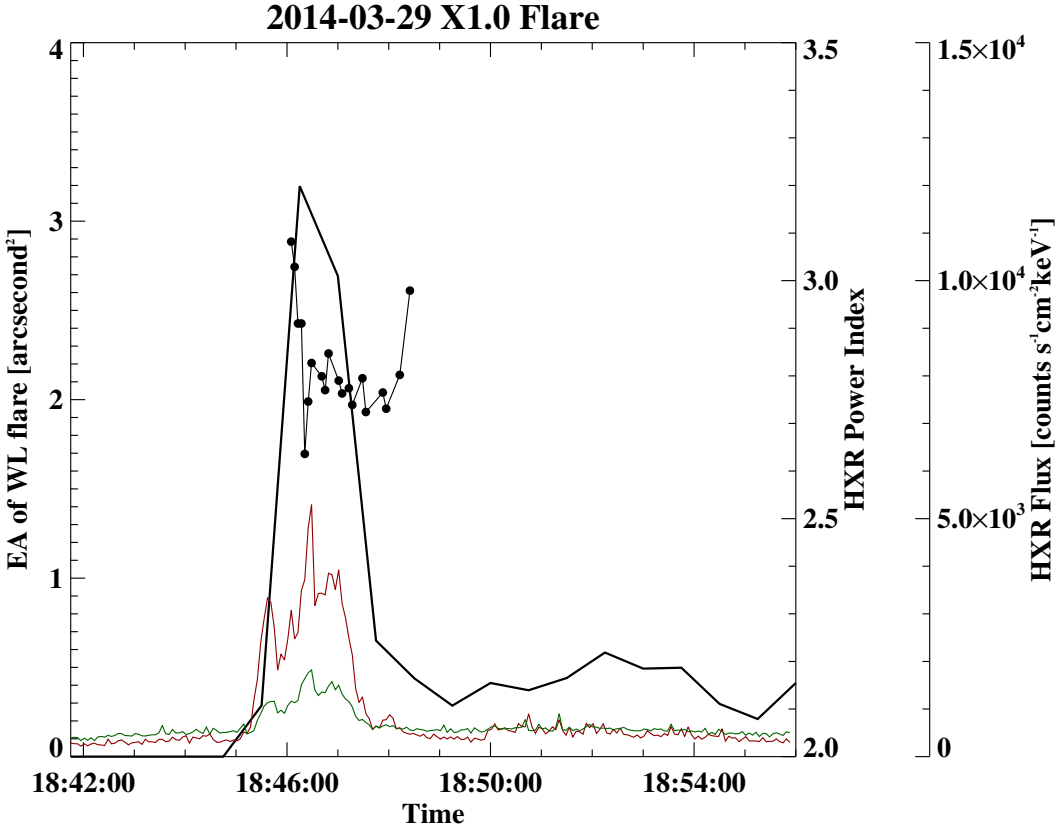

Figure 2.4 Time evolutions of WL EA, HXR energy flux, and HXR power index during the flare on 2014 March 29th. The red and green lines indicate the fluxes of HXR in energy ranges of 50-100 keV and 100-250 keV, respectively. The thick black line shows the temporal variation of WL emission and the dotted line represents the power index evolving as a function of time. As expected, a good correlation between the WL and HXR emission is shown. More importantly, we see a negative temporal correlation between WL emission and HXR power index.

the events in our study. Our result is consistent with that was observed in the work of Fletcher et al. [53], in which HXR power above 20 keV and 50 keV were compared with the WL power. Our result suggests that the **distribution** of high-energy non-thermal electrons is more critical, and the electrons in even higher energy are more closely related to the generation of WL flares. However, using a more extensive data set and a different method in detecting WL, Kuhar et al. [102] found a positive correlation between WL emissions and HXR fluxes at 30 keV. Moreover, their result shows no clear correlation between the WL emission and HXR spectral indices, which is also

different from our result. The discrepancy is mainly due to the method of measuring the EA of WL emission. For each flare, they integrated all the excess WL flux automatically within a certain level of HXR contour. In our study, we manually set thresholds for the WL flare kernels, which can be identified visually. Therefore, only the intense flare cores are included in our analysis. According to previous studies [136, 188, 89, 187], the WL flare kernels are consist of bright inner cores and relative weaker halos, corresponding to the direct heating by electrons and the back-warming emission, respectively. The intensity of the halo structure is not a monotonically increasing function of electron energy. Therefore, the relationship between the HXR spectral index and WL intensity is altered for halos. By concentrating on the core emission, we exclude the contamination of halos and other uncertainties introduced by the misalignment among frames in a time sequence.

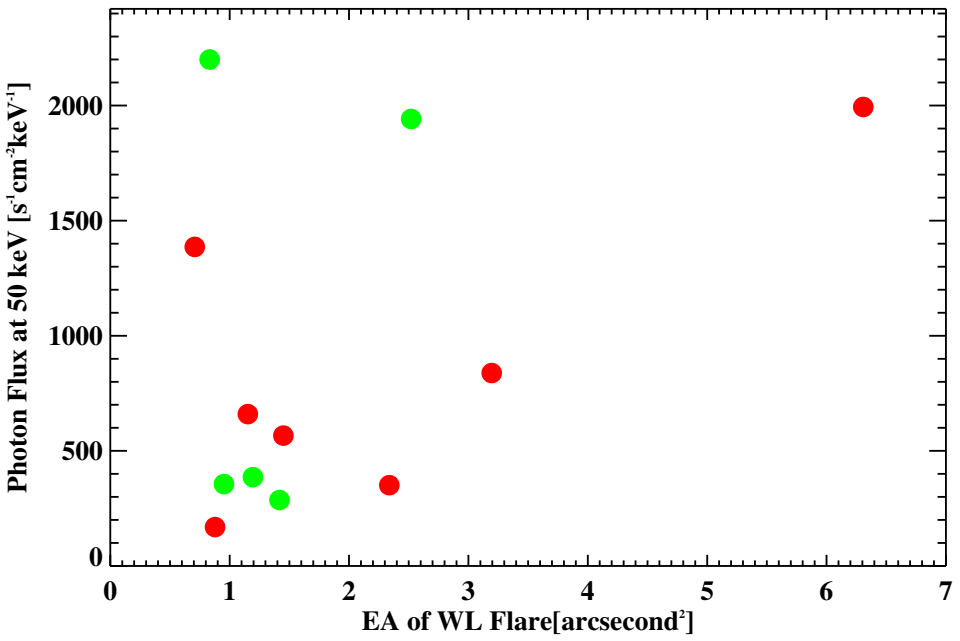

Figure 2.5 The scatter plot of WL EAs and HXR peak fluxes at 50 keV. The red dots represent the X-class flares, and the green dots indicate the M-class flares.

The HXR power indices vs GOES classes of the other 12 non-WL flares are plotted in Figure 2.6. Again, the green and red colors are used for M-class and X-class flares, respectively. It is clear that two distinct groups can be defined for M- and X-class flares. For the X-class flares without detectable WL enhancement, we see that all of the four events have relatively higher power indices (>6), which implies that they have less high-energy electrons although they have relatively high SXR emissions. This result is consistent with the result of WL flares discussed above. However, for M-class non-WL flares, their power-law indices can be small, indicating the spectra are as hard as the WL flares. These events have lower levels of SXR emissions, which means fewer thermal electrons. Based on the assumption of energy distributions of accelerated electrons, even though having lower power-law indices, these events with lower thermal electron does not have enough high-energy electrons to stimulate the WL emissions.

In summary, 25 disk-center events above GOES class of M5.0 are studied since the launch of SDO. They are also covered by RHESSI HXR observations. The WL emission are quantified by the EA and the high energy electrons are represented by the the power-law index of HXR emission. The result shows a negative correlation between them, suggesting that the high-energy electrons play an important role in producing WL emission during strong flares. On the other hand, for the M-class flares, especially those without WL emission, the power-law index is neither the only nor the most important parameter to determine the WL emission. Considering the complexity of WL and HXR emission, this study are preliminary and can be improved by carrying out a more comprehensive analysis. For instance, the $hmi.Ic\_45s$ data from SDO/HMI is not real continuum data but reconstructed by intensity data at six spectral points, which can introduce uncertainties of intensity measurements. For future analysis, more precise results can be obtained by including filtergrams without any reconstruction and using higher spatial-temporal resolutions.

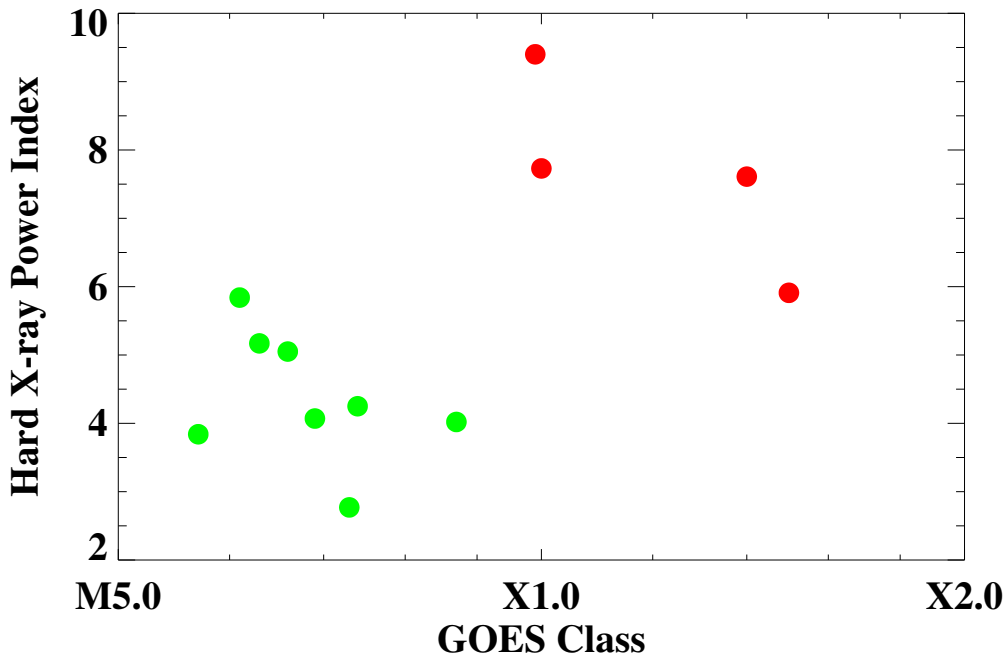

Figure 2.6 Plot of *GOES class* and *hard X-ray power index* of non-WL flares. For the X-class flares without obvious WL enhancement, the peak spectra show considerably high HXR power indices, while all of the power indices for M-class flares are smaller than 6.

2.4 WL Observation of 2015-June-22 M6.5 Flare

Table 2.3 Properties White-Light Flares

Date	Time	GOES	AR#	Location	Equivalent Area	HXR Spectral Index
2015.06.22	17:39	M6.5	12371	N13W14	0.1	4.37

The latest instruments have been proving the necessity of resolving power in WL flare observations. The BBSO/GST, one of the highest resolution telescopes for solar observations, was used to observe the WL emissions in flares. On 2015-June-22, the M6.5 flare was observed by GST, using the TiO filter on BFI. The basic information is in Table 2.3. Using both the intensity continuum images from

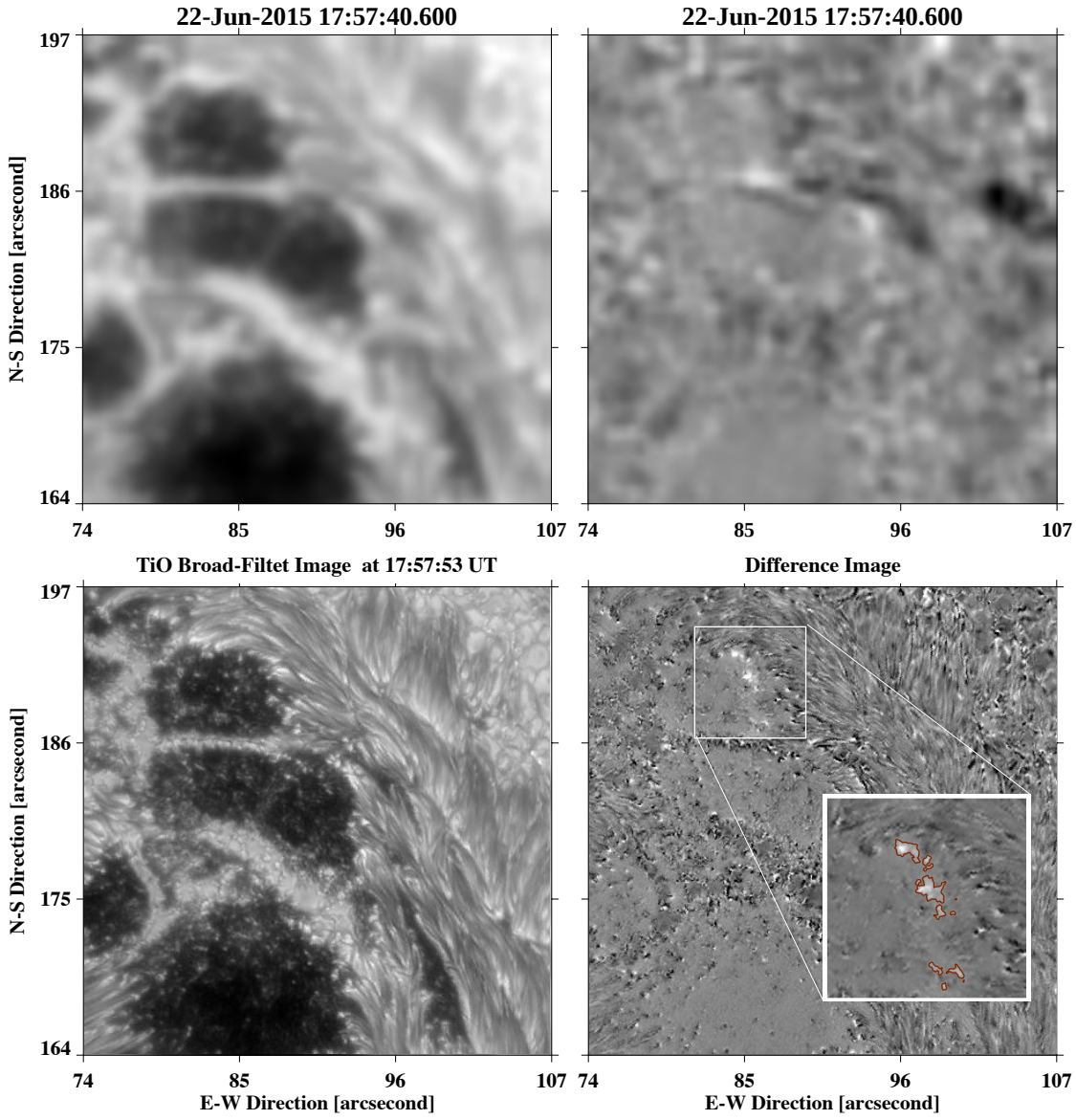

Figure 2.7 WL observation of 2015-June-22 M6.5 Flare, using SDO/HMI and GST/BFI. All images were aligned to the same FOV. Upper Panels: The intensity continuum image from SDO/HMI at the peak time (left) and the corresponding difference image (right). Lower Panels: Broad filter TiO image from GST/BFI for the flare peak time (left) and the difference image, subtacting a pre-flare frame (righ).

SDO/HMI and the TiO broad filtered images from BBSO/GST, the difference images were processed, and the EAs were calculated, as is presented in Figure 2.7. All of the panels in Figure 2.7 were aligned to the same FOV. The left two panels were simultaneous images, which are taken at the flare peak time, and the right panels are the difference images subtracted by pre-flare frames correspondingly. The upper panels were continuum images from HMI, and the lower ones are presenting the broad-filter images from GST. In HMI continuum images, the WL emission was too faint to identify. Using the high-resolution TiO images from GST, some small but well-defined emission areas were detected. The compact brightenings points were distributed over a ribbon-like area. The the white box in the lower right panel in Figure 2.7, we zoomed in to show them more clearly. Using the same algorithm, we retrieved the contrast image in refers to a selected background area where a standard deviation was calculated. The red contours outlined three times of standard deviation and defined the footpoint areas of flare. The EA and the HXR power-law index were than calculated. The results were listed in Table 2.3 and plotted as the blue dot in Figure 2.8.

The EA of this WL flare was 0.01 $arcsec^2$, which would not be detectable signal noise in lower resolutions. It is necessary to mention that in Figure 2.8, over-plotting the data point retrieved by GST/BFI image onto the EA-HXR power-law index scatter plot directly, is only for rough comparison, since different continua were in used. However, the comparison between HMI images with $0.5\,''/pixel$ images scale and GST TiO images with $0.034\,''/pixel$, confirms that more WL flares would be resolved by using high-resolution observations in solar flares.

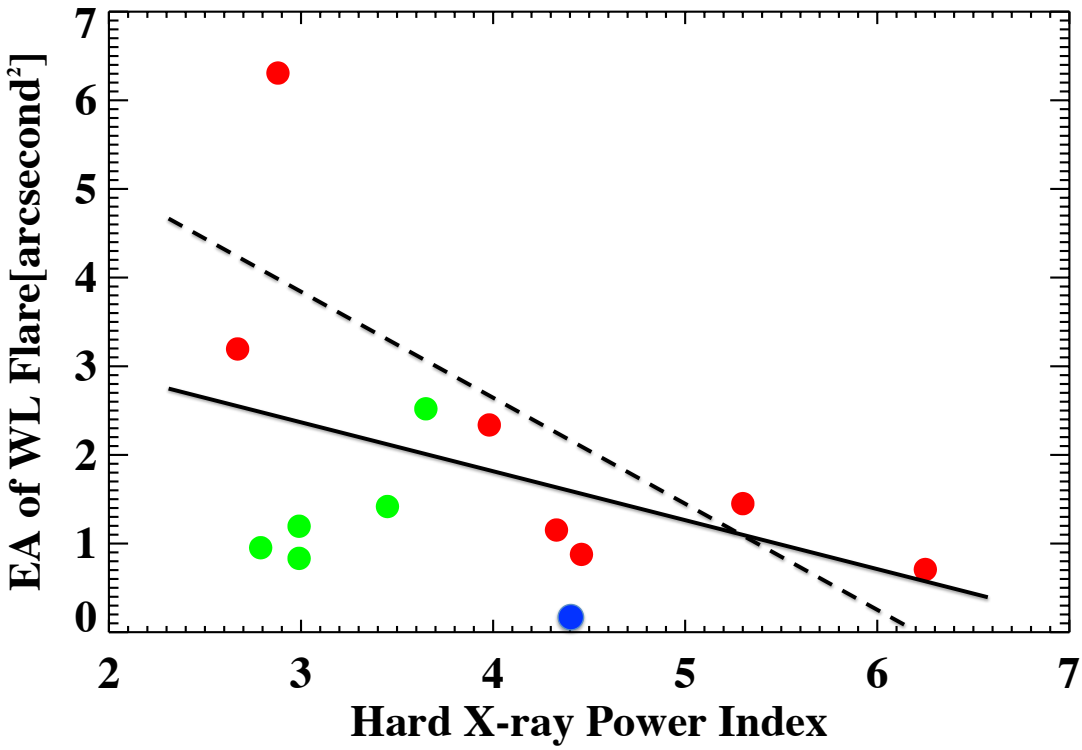

Figure 2.8 The equivalent area of this WL flare is about 0.01 $arcsec^2$ (by GST, not detectable by SDO) and the HXR spectral index is 4.37 at the peak time. This "new" event was denoted as the blue dot.

CHAPTER 3

RELATIONSHIP BETWEEN INTENSITY OF WHITE-LIGHT FLARES AND PROTON FLUX OF SOLAR ENERGETIC PARTICLES

3.1 Introduction

Solar Energetic Particles (SEPs; see review by Reames 1999 [147]) are considered to be one of the most important kinds of events in terms of their effects on space weather. They are mostly in the form of accelerated protons and heavy ions. The SEPs were found to be accelerated by magnetic reconnection during solar flares (e.g., Mori et al. 1998, Bombardieri et al. 2008 [88, 16]). They also can be accelerated by shocks while CMEs are propagating in interplanetary space (e.g., Klein & Trottet 2001, Roussev et al. 2004 [97, 148]). Aschwanden [10] found that both flare and CME shock play important roles. In solar observations, WL flares are considered as the most energetic signature of particles bombarding solar surface and associated with both HXR and Gamma-ray emissions [83]. In our previous study (see Chapter 2), we found a close correlation between WLF intensities and the HXR power index [81]. In this chapter, we focus on the comparison between SEP flux and WLF intensities. [1]

3.2 Data Reduction and Discussion

In this study, WLFs are identified using the $hmi.Ic\_45s$ data obtained by SDO/HMI. It is not real continuum data but reconstructed by intensity data at six spectral points close to Fe XXI 6173 Å line. The counts of SEP flux can be found at `https://umbra.nascom.nasa.gov/SEP/`, which is curated by Solar Data Analysis Center. It lists all the SEP events captured by detectors onboard GOES [55]. The proton flux in this list is defined as averages of integrated 5-minute counts of particles

[1] This chapter is based on the following paper: Huang, N.; Xu, Y. & Wang, H., "Relationship between Intensity of White-light Flares and Proton Flux of Solar Energetic Particles", *Research Notes of the AAS*, 2018, volume 2, 7 [80]

Table 3.1 Fluxes of SEP Events And Properties of the Corresponding Flares (continued)

#	Date	Time (max)	GOES	AR#	Location	Proton Flux > 10MeV (pfu)	WL EA ($arcsec^2$)
1	2010.08.14	12:45	C4	11099	N17W52	14	No
2	2011.03.08	08:00	M3	11164	N24W59	50	No
3	2011.06.07	18:20	M2	11226	S21W64	72	No
4	2011.08.05	21:50	M9	11261	N15W49	96	1.19
5	2011.08.09	12:10	X6	11263	N17W83	26	3.09
6	2011.11.27	01:25	C1	11353	N08W49	80	No
7	2012.01.24	15:30	M8	11402	N28W36	6310	0.1
8	2012.01.28	02:05	X1	11402	N27W71	796	No
9	2012.03.08	11:15	X5	11429	N17E15	6530	7.65
10	2012.03.13	20:45	M7	11429	N18W62	469	6.39
11	2012.06.16	20:20	M1	11504	S17E14	14	No
12	2012.07.07	07:45	X1	11515	S18W50	25	5.95
13	2012.07.12	22:25	X1	11520	S16W09	96	No
14	2012.07.18	06:00	M1	11520	S17W75	136	No
15	2012.09.02	08:50	C8	None	S06E20	59	N/A
16	2012.09.28	04:45	C3	11577	N08W41	28	No
17	2013.03.17	07:00	M1	11692	N11E12	16	No
18	2013.04.11	16:45	M6	11719	N09E12	114	No

(continued) Fluxes of SEP Events And Properties of the Corresponding Flares

#	Date	Time (max)	GOES	AR#	Location	Proton Flux > 10MeV (pfu)	WL EA ($arcsec^2$)
19	2013.05.17	17:20	X1	11748	N11E51	41	No
20	2013.05.23	06:50	M5	11745	N15W70	1660	No
21	2013.06.24	05:20	M2	11777	S16E66	14	No
22	2013.09.30	20:05	C1	None	N15W40	182	No
23	2013.12.28	23:15	C9	11936	S18E07	29	No
24	2014.01.09	03:40	X1	11944	S15W11	1033	No
25	2014.02.20	09:25	M3	11976	S15W67	22	No
26	2014.02.28	08:45	X4	11990	S12E82	103	No
27	2014.04.19	01:05	M7	12036	S16W41	58	No
28	2014.09.12	15:55	X1	12158	N16W06	126	No
29	2015.06.22	19:00	M2	12371	N13W00	1070	No
30	2015.06.27	00:30	M7	12371	N12W40	22	2.48
31	2016.01.02	04:50	M2	12473	S21W73	21	No
32	2017.07.14	23:20	M2	12665	S06W29	22	No
33	2017.09.08	00:35	M5	12673	S11W16	844	2.14

with energies higher than 10 MeV. The unit is *particle flux unit(pfu)* where 1 pfu = 1 particle·cm^{-2} sr^{-1} s^{-1}. An event record started when there were three data points equal or greater than 10 pfu in a row, and ended when it decrease to 10 pfu or lower. According to the record, there were 42 SEP events recorded from 2010, when SDO was launched, to September 2017. Among these listed 42 SEP events, excluding the farside ones, 37 of them are accompanied by flares. For the flares higher than M5.0 among them, we used the difference images of intensity continuum data from SDO/HMI and visually identify the WL emission signals. The WL emission is characterized by an EA [173, 81], which is the integrated enhancement of contrast over the entire flare ribbons, as was defined in Chapter 2. The information about these flares, their WL emissions and energetic particle fluxes are listed in Table 3.1

Events in Table 3.1 are scatter plotted in Figure 3.1 according to their proton fluxes in a unit of pfu and EAs of WL emissions in a unit of arcsecond^2. For events without WL emissions, the EAs were set to be zero. To extend our study, we also included the WL flares within the same period, which are not accompanied by SEP. Most of them are listed in Table 2.1 except for the latest X9 flare, which we will discuss in more detail below. In the plot, the solid circles represent the SEP events, and the empty circles represent the WL flares without detected SEP signals. For all these events, red, blue and green colors are denoting their GOES flare classes, X, M and C, respectively. By comparing the SEP and WLF lists, the events can be divided into three groups:

- Group 1: The group includes SEP events that were not associated with WLFs. They are plotted using solid circles (half) on the y-axis, indicating zero WL emission. Their SXR flux (represented by GOES classes in different colors) does not correlate with the proton flux. As we can see, a C-class flare may have stronger proton flux than many X- and M-class flares (e.g., event # 22 in Table 3.1). It should be noted that some of the events in this group are possible to have WL emissions that is too weak to be defined as signals. For example, the #29 event in Table 3.1 was visually identified as a weak WL flare using TiO 7057 Å BFI in BBSO/GST, while it is not visible using intensity continuum images from SDO/HMI.

- Group 2: This group contains WLFs without SEP detected. Those events are represented by empty circles (half) on the x-axis. The latest X9 flare, which was not included in Table 2.1, was on Sept. 6, 2017. It was the strongest WLF with EA almost an order of magnitude larger than the second largest one. However, no obvious increase in proton flux was detected. This group also suggested the irrelevance between WL emissions and SEP fluxes.

- Group 3: We found eight SEP events that were associated with WLFs, including 5 M-class (blue color) and 3 X-class (red color) flares. There is no clear correlation between SEP fluxes and EAs of WLFs in this group, as we can see.

The events in these all three groups show that there is no correlation between WLFs and SEPs. This result indicates that the SEPs may not be accelerated in the region where flare-related magnetic reconnection takes place. Besides, one can notice that there is no clear intersection between events in Table 2.1 and Table 3.1. In other words, almost none of the WL flares selected in Chapter 2 are accompanied by SEPs. The only exception is event #24 in Table 3.1, whose SXR time profile is plotted in Figure 3.2. The two vertical yellow dashed lines mark the starting and peak time of SEP flux. The green arrow is pointing at the flare associated with this SEP event, and the red arrow is pointing at an M7.2 WL flare listed in Table 2.1. The detection of the SEPs in this event was combined with a far-side event, and that moved up the start time. However, this SEP event was associated with the X1 flare without WL emission, which was companioned by CME.

Another noteworthy event is the X9 WL flare on Sept. 6th, 2017, which in Figure 3.1 is plotted on the x-axis. This flare happened in the same active region as

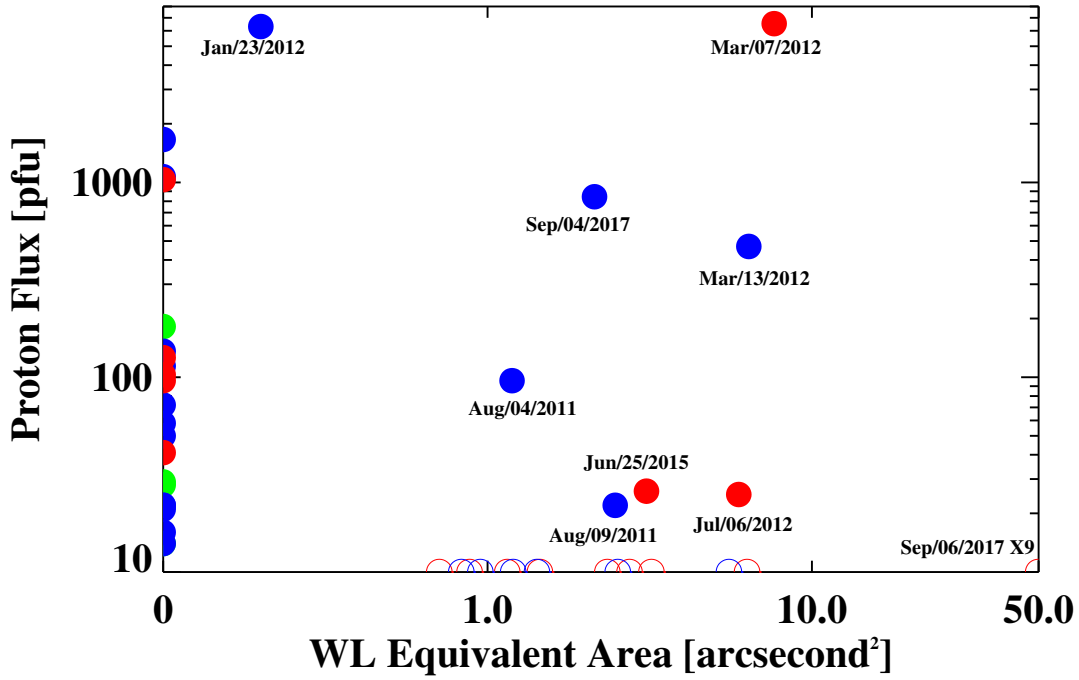

Figure 3.1 Comparison of SEP events and WLFs. Solid circles represent SEP events and empty circles represent WLFs, which were not associated with SEP events. Different colors indicate the magnitudes of flares: red for X-class, blue for M-class and green for C-class flares.

the M5 flare that is responding to events #33. The time profile of SXR flux is plotted in Figure 3.3. That productive AR was detected to have SEP from the beginning of Sept. 6th and reached the peak on Sept. 8th. It is reasonable to guess that the long duration SEP event was contributed by multiple flares continuously, including the X9 flare with outstanding WL emission. However, the peak of the SEP flux arrived at the beginning of Sept. 8th, which is more likely to be contributed by activities on Sept. 7th.

Our preliminary results show that most ($> 83\%$) of WLFs and SEP events have no correspondence. Note that all SEP events were checked, and some limb WLFs were excluded to avoid projection effect in calculating the EA. Therefore, the actual percentage of non-correlated events should be even higher. In a small group of events

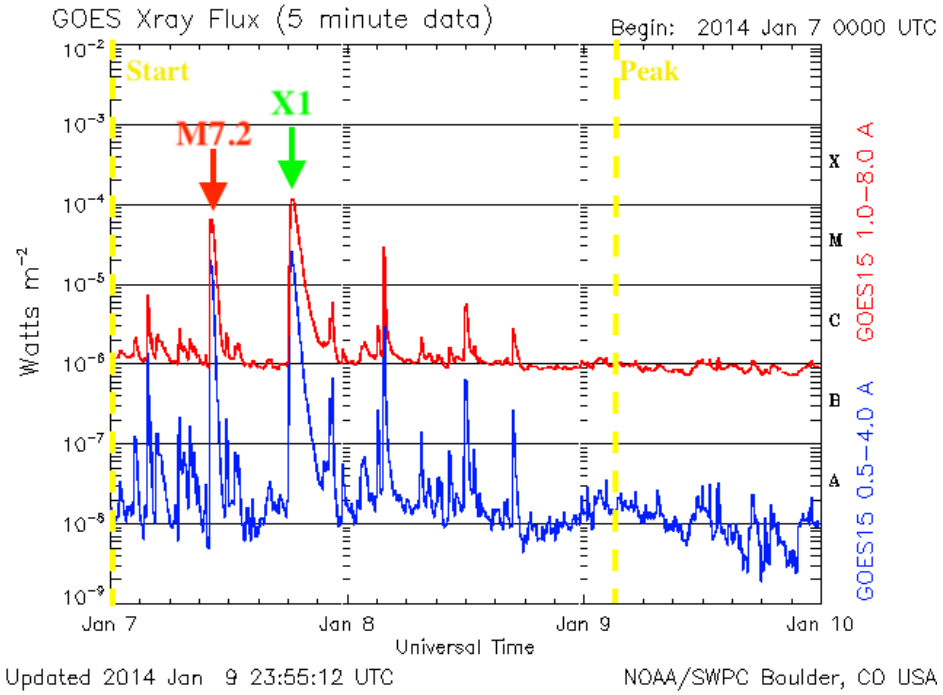

Figure 3.2 Time profile of GOES SXR emission during the SEP event peaked on January 9th, 2014(Table 3.1 # 24). The two vertical yellow dashed lines mark the starting and peak time of SEP flux. The green arrow is pointing at the flare associated with this SEP event, and the red arrow is pointing at an M7.2 WL flare listed in Table 2.1.
Source: GOES X-ray 3-Day plot archive.

with both WL emission and SEPs, we did not see a positive correlation between SEP flux and contrast enhancement in WL. In the time profile of each event, the relevance between WL emission and SEPs are weak. Straightforward speculation is that the acceleration process could be different for SEPs and the energetic electrons powering WL flares in the events analyzed. In other words, between the possible SEP acceleration mechanisms, flare reconnections versus CME waves, our result favors the latter one. However, these two candidate drivers for SEP are not independent. Many studies have suggested the combination of both of them. Particles on different parts

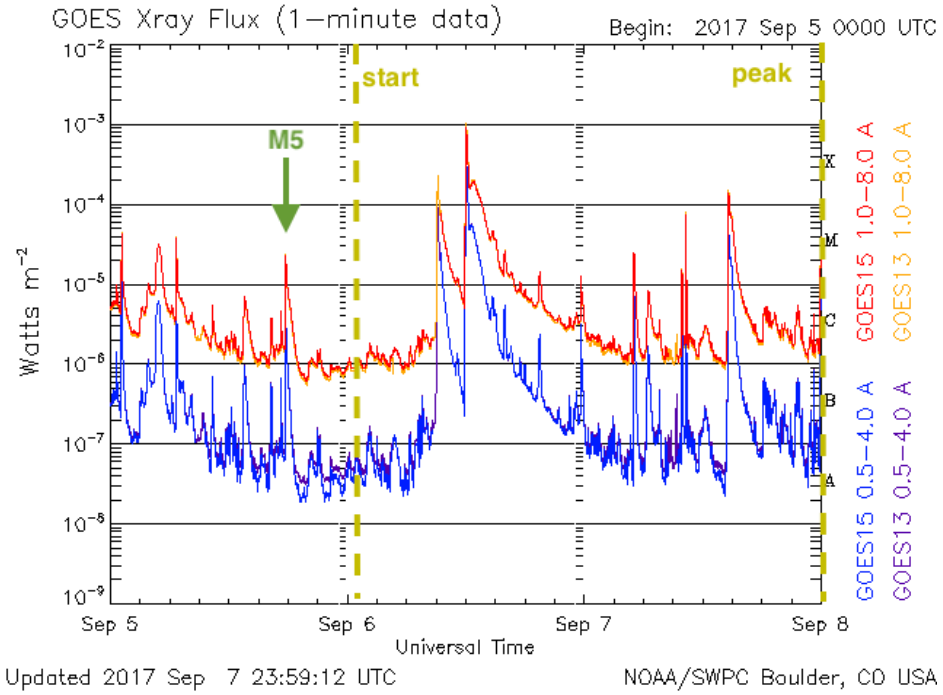

Figure 3.3 Time profile of GOES SXR emission during the SEP event peaked on September 8th, 2017 (Table 3.1 # 33). The two vertical yellow dashed lines mark the starting and peak time of SEP flux. The green arrow is pointing at the flare associated with this SEP event. The 2017-September 6th X9.3 flare began at 11:53 UT and SXR peaked at 12:03 UT.
Source: GOES X-ray 3-Day plot archive.

of the energy spectrum were probably driven differently. Our study used the 10 MeV as a threshold for energetic particle flux counting, which was lower than what was commonly used in studies that connected SEPs with flares. In summary, our result suggested the importance of the CME shock wave in SEP acceleration.

CHAPTER 4

SPECTRAL DIAGNOSIS OF MG II AND Hα LINES DURING THE INITIAL STAGE OF AN M6.5 FLARE

Recent studies have shown the existence of fine structures on flare kernels or ribbons, which were not fully resolved before. One of the important results is the distinct properties on the leading edge of the propagating flare ribbons, such as the enhanced absorption in He I 10830 Å line and a strong redshift in Hα. In order to gain more comprehensive understading of the absorption and Doppler shifts in the lower atmosphere, we investigated the emission from upper chromosphere which is closer to the initial energy release site in corona and may have effects on lower layers. Using the high-resolution imaging spectroscopic data obtained by IRIS, we studied the Mg II emission lines during an M6.5 flare (SOL2015-06-22T18:23), which was well covered by the joint observation of IRIS and BBSO/GST [1]. On the leading edge of the propagating ribbon, Mg II h and k lines are characterized by blue wing enhancement and strong broadening. On the other hand, redshifts in Mg II and Hα are found in the following areas of the flare ribbons. Numerical modeling, by combination using RADYN and RH codes, suggested that the Mg II line broadening was possibly caused by unresolved turbulence with velocities distributed in about 10 to 30 km/s. The enhanced blue wing is likely due to a decrease in temperature and an increase in electron density as a consequence of electron precipitation. Based on the observations and simulation results, we discussed the possible response of the lower atmosphere to the electron precipitation, in terms of the evolution of temperature, electron density, and turbulence velocities.

[1]This chapter is based on the following paper: Huang, N.; Xu, Y.; Sadykov, V. M.; Jing, J. & Wang, H., "Spectral Diagnosis of Mg II and Hα Lines during the Initial Stage of an M6.5 Solar Flare", *The Astrophysical Journal Letters, American Astronomical Society*, 2019, volume 878, L15 [79]

4.1 Introduction

Flare footpoints are usually ribbon-like structures at lower atmospheres. The intensities over the ribbon are not uniform with high-resolution observations. For instance, core-halo structures were found on the well-defined WL ribbons [188]. These features were explained using dual-heating mechanisms, namely, direct heating and chromospheric back-warming [188, 89]. Benefited by the improvement of modern instruments, unprecedented resolutions made finer structures revealed. The 1.6-m GST in BBSO currently provides the highest resolution at visible (0.″027/pix) and NIR images and magnetograph observation. Sharykin & Kosovichev [157] and Jing et al. [92] found 100 - 160 km narrow leading frontiers that show strong pseudo redshifts in Hα line. Xu et al. [185] reported enhanced absorption in He I 10830 Å, concentrated in a 340-km wide ribbon front. More importantly, this absorption is co-aligned with strongly broadened Mg II h&k line profiles with an FWHM of 1 Å observed by IRIS. Panos et al. [138] implemented the machine learning method on 33 flares and found universal characteristics on leading ribbon front, including strong broadening, blueshift, and central reversal. According to the standard flare model (see Figure 1.3, the leading front of the ribbon represents the footpoints of the newly reconnected flare loops. Therefore, the different characteristics on the leading front and following areas indicate the difference of distributions in the initial precipitating electron beam and the trapped electrons by the magnetic loops.

In addition to the emissions, other signatures of precipitating electrons, chromospheric evaporations and condensations [50], have been observed and studied using coronal [64, 128] and chromospheric lines [21]. The evaporation speed reaches 300 km s^{-1} and the condensation speed can reach 40 km s^{-1}, and the condensation occurred earlier than the evaporation flows[64, 63]. On the other hand, the existence of the dominant stationary component suggests that the observed Doppler signals come from multiple filamentary loops [69]. Chromospheric condensation was found to be

concentrated at the leading fronts of flare ribbons, in agreement with the filamentary scenario indicating a relationship with the unique properties of the leading ribbon front [47]. More recently, Tei et al. reported blueshift in Mg II h&k lines during the impulsive phase of a flare [166].

In this chapter, we analyze the IRIS Mg II h&k spectral profiles and make a comparison with Hα pseudo Doppler maps calculated from spectroscopic images taken by VIS of BBSO/GST. These lines are formed in chromosphere [172, 167], where most of the energetic electrons deposit their energy and evaporation and condensation originate. With high-resolution data provided by IRIS and BBSO/GST, important constraints of chromospheric dynamics are investigated.

4.2 Observations

An M6.5 flare was observed on 2015-06-22 by the joint observation of BBSO/GST and IRIS. The hosting active region NOAA 12371 was close to the disk center around N13W14. It started at 17:39 UT and decayed slowly in several hours. The flaring areas include an intensive core and a significantly extended region (see Jing et al. 2017 [91]). The field-of-view (FOV) of GST observations covered the region of two major sunspots in opposite polarities. Within this area, two flare ribbons are seen moving away from each other.

IRIS provides spectral data on FUV (1331.7 Å - 1358.4 Å and 1389.0 Å - 1407.0 Å) and NUV (Interface 2782.7 Å - 2851.1 Å), as well as the slit-jaw images (SJI, taken at 1330 Å, 1400 Å, 2796 Å, and 2832 Å). Raster mode of large coarse 16-step and $16'' \times 130''$ FOV were used with standard flare line list (OBSID3660100039). The time lag between steps is 2 s, and the cadence between scans (16 positions) is 33 s. The pixel resolution is $0''.6$. In this event, the IRIS FOV is tilted by 45° for better coverage of ribbons. Figure 4.1 shows sample images of GST Hα off-band in Panel (a) and 1330 Å SJI in Panel (b). The three panels were taken almost simultaneously.

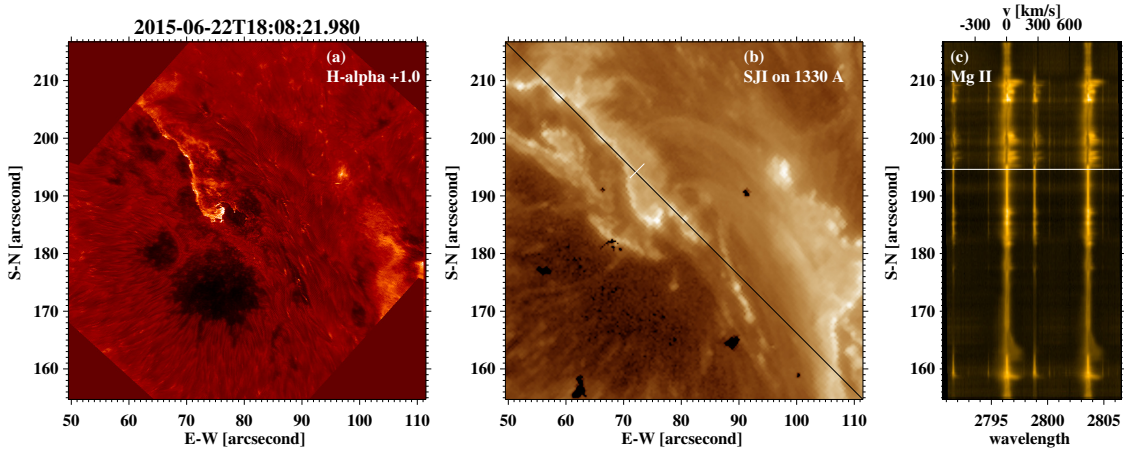

Figure 4.1 Panels (a): Hα off-band image taken at 18:08 UT on 2015-06-22. Panel (b): IRIS 1330 Å SJI within the same FOV and same time as Hα off-band image, the black line denotes the slit, and the short white stick marks the location of the sampling pixel mentioned in Section 4.3.1. Panel (c): The Mg II spectra along the slit represented by the black line in Panel (b), and the horizontal white line indicate the spectrum of the sampling pixel in Panel (b).

IRIS SJI was rotated and cutted to be aligned with GST FOV. The spectrogram in wavelength window covering Mg II h&k lines, in Panel (c), was taken along the dark slit shown in Panel (b). The horizontal white line in Panel (c) denotes the corresponding spectrum from the position on the slit marked with the white stick in Panel (b).

GST provides three channels, TiO 7057 Å, Hα, and vector magnetograms using the NIR 1.56 μm line, for this event. Weak white-light emissions were detected in the TiO band [80]. In this study, we focus on the Hα images. They were taken by VIS at five different spectral points: center line and off-bands ($\pm$0.6 Å and $\pm$1.0 Å). The cadence of the 5-point scan is 28 s after speckle reconstruction. For the Doppler images, the time lag is 3 to 4 s between the off-band image pairs. The pixel size of the Hα image is $0''.03$ and the FOV is $57'' \times 64''$.

In addition, context data of HXR and full-disk UV images were obtained from RHESSI and SDO/AIA, respectively. The RHESSI data was used to extract the

HXR spectral parameters, such as the power-law index, low energy cut-off, and total electron flux, which are key inputs for numerical simulations. SDO/AIA images are used as reference images to align IRIS with GST data. The HXR spectrum and UV images were used for the numerical study and will be described in more detail in Section 4.3.3.

4.3 Data Analysis and Results

4.3.1 Mg II Blueshift And Broadening

Formed mainly in the upper chromosphere, the Mg II h&k resonance doublets are among the strongest emission lines in UV spectra due to the abundance of Mg in the chromosphere. Due to their similar behaviors of these two lines, our investigation focuses on the k line at λ 2796 Å. The intensity maximum, Doppler shift, and line width were measured. The intensity maximum was the value of peak of k line. The line width was defined as the full width at 1/3 maximum [41]. To describe the Doppler shift signal, two methods were used and compared, namely integrated centroid and bisector of different intensity levels. The centroid method is to find the difference between the integrated arithmetic mean of the line profile and the theoretical line center. The bisector method calculates the arithmetic mean at a given intensity level, for instance, at the 1/3 maximum. The bisector shifts vary as a function of intensity levels. We found that the results from 1/3 maximum bisector and integrated method are in good agreement.

The IRIS slits covered the main section of the north ribbon. Due to the similarity, the spectra at the first list position (from 16 positions) were used as the representative spectra. Time-space diagrams of the intensity maxima, Doppler shift of centroid, and full width at 1/3 maximum are shown in upper panels of Figure 4.2. The color bars on top of each diagram present the scale of colors. It should be noticed that the intensity maxima were normalized in this plot. Additionally, the color scale of Doppler shift diagram was not symmetric for blueshift and redshift.

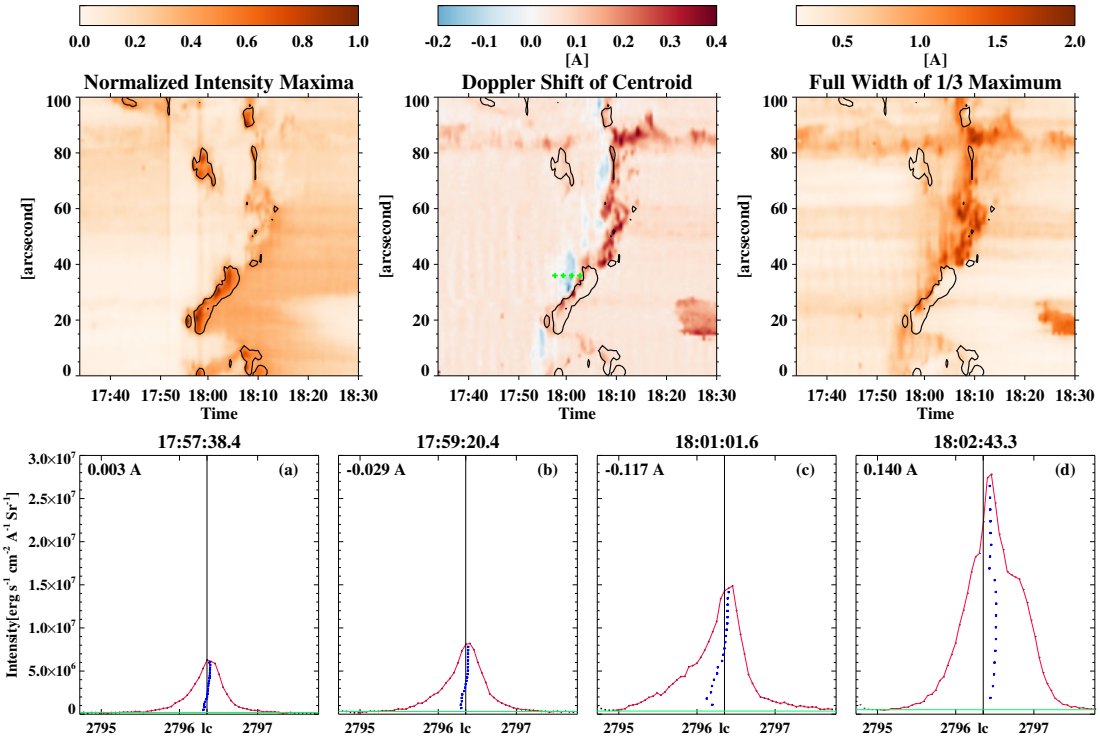

Figure 4.2 Upper Panels (left to right): time-space diagram of emission maximum, doppler shift of bisector of 1/3 maximum, and the full width of 1/3 maximum of Mg II k line with corresponding color bars on top, respectively. The contours of the time-space diagram of intensity maximum are over-plotted onto the diagrams of Doppler shifts and line width. The green plus signs mark are representing for the data points whose line profiles are used as examples in lower panels. Lower Panels: Sample Mg II k line profiles (a) before flare, (b) at the initiation time, (c-d) with blue wing enhancement and at flare peak. The green horizontal line is the background level and blue asterisk points are the bisectors on different intensity levels. The shifting of their centroids are on the upper left corner of each plot.

To show the evolution of the line profile more clearly, contours of intensity maxima are overlaid to each of the diagrams. From these, we found: 1) The maximum Mg II k emission correlated with strong redshift well, which means that the strongest line emissions were accompanied by Doppler redshift; 2) This line is significantly broadened over 1.0 Å at 1/3 maximum; 3) Blue-wing enhancement was found at 33 - 165 seconds prior to the maximum emission, which presents as Doppler blueshift coincident with increased line broadening. The typical blue shift (averaging the entire profile) is less than 10 km/s, but can reach 20 km/s at certain locations.

Samples of Mg II k profiles were shown in the bottom of Figure 4.2. The time-steps of these profiles are indicated by green plus in the Doppler time-space diagram in the upper middle panel. The bisector centroids at different intensity levels are shown as blue asterisks in each line profile plot. The overall Doppler shift is calculated by averaging all of the centroids and noted on the upper left corner of each panel. Before being heated, the overall shift is nearly zero compared with the theoretical line center (Panel (a-b)). When the ribbon front passes through the second green cross, the blue-wing of the Mg II enhanced, leading to a left-shift of the line centroid. This is the blue-wing enhancement we are studying in this chapter. Shortly after that, the ribbon with peak intensity steps in, and the line profile becomes red-shifted.

4.3.2 Hα Redshift

To investigate the spatial relationship between Mg II and Hα observations, precise image alignment was required. Both IRIS SJI in 1330 Å and Hα images were registered with a full-disk reference image taken in 1700 Å by SDO/AIA, and heliocentric coordinates of IRIS and GST's FOVs are determined. As shown in Figure 4.1, GST's FOV was well-covered by the relatively larger FOV of IRIS SJIs. Therefore, SJIs can be cut to align with GST FOV. Hα pseudo Doppler maps were calculated by subtracting blue-wing images from the red-wing images. Along the same slit position that IRIS had, time-space diagrams of Hα pseudo doppler shift were retrieved. Zooming into the time and space that the flare ribbon passed through the slit position, the diagram was shown in Figure 4.3 Panel (a). The colored lines over it were contours of Mg II Doppler shifts, where the blue contoured out the blueshift of the line centroid, and the red contoured out the redshift. Panel (b) plots the time profiles of Mg II k Doppler shift and Hα pseudo Doppler shift at a representative location indicated by the black line in Panel (a). It can be told from both panels

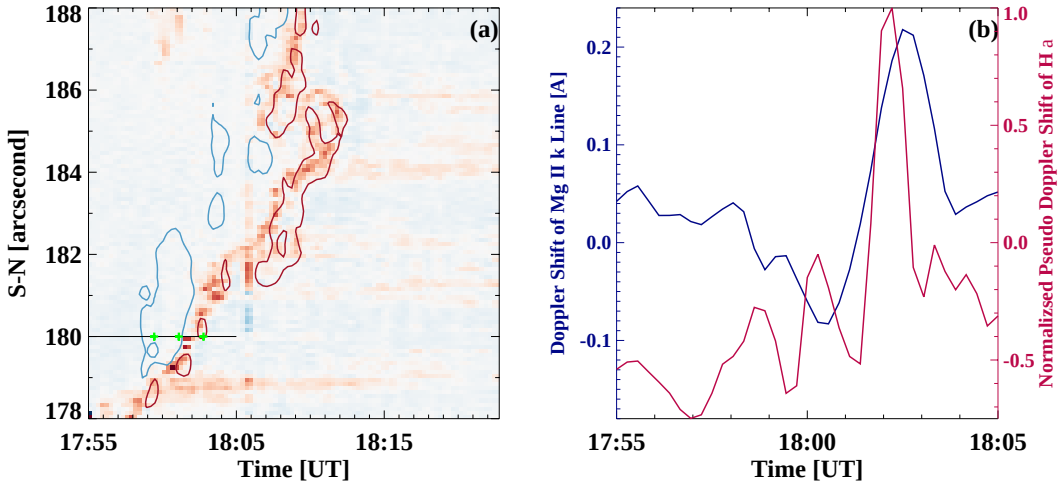

Figure 4.3 Panel (a): Time-space diagram of Hα pseudo Doppler shift with contours of IRIS Mg II k velocity (20 km s^{-1} level). The blue and red colors indicate the blue and redshift in Hα. Panel (b): Temporal profiles of Mg II k line (blue) and normalized pseudo Doppler of Hα (red). The corresponding location and time are indicated by the black line in Panel (a).

that the strong Hα redshift located between the timings that the centroid Mg II turned from blueshifted to redshifted. Since this flare ribbon moves across the slit, the relative locations represent the order of appearance of these Doppler shifts. The results can describe the evolution time sequence that the Mg II blue-wing enhanced first, followed by the redshifts in Hα and Mg II. Comparing to the temporal evolution described in a previous study on this event [174], this blue-wing enhancement followed the second flare precursor, by which the conditions, such as temperature and density, of the chromosphere have been disturbed.

4.3.3 Numerical Modeling and Possible Physics of Doppler Signals

We attempted to explain the thermodynamic conditions of the atmosphere where Doppler signals were generated. There are several existing packages in modeling the flaring atmosphere. One of the most commonly used radiative hydrodynamic code, RADYN [23, 25, 5, 6], calculates the time-dependent atmospheric response to

energy deposition, capturing the dynamics of the processes. It considers optically-thick radiation and calculates for the dominating atoms in chromospheric radiation-energy balance. However, Mg II was not included in the RADYN code that we use (see below for more detail). On the other hand, a radiation transfer code, RH [168], models the flare emissions time-independently. It is capable of solving Mg II using partial frequency redistribution (PRD) instead of complete frequency redistribution (CRD) used in RADYN, which is considered to be effective in the formation of Mg II [162, 107]. Following the idea of previous studies (e.g., Rubio da Costa et al. 2016 [150]), we started with RHESSI HXR spectral parameters and obtained results from RADYN simulation, including parameters of the heated atmosphere, such as the temperature, velocity, electron density, micro-turbulence, as functions of column mass. Then each of the snapshots representing the atmosphere for each time-steps during the pulsation, calculated with RADYN, were passed through RH code to compute the Mg II profiles.

The key inputs of the RADYN, include energy flux, power-law index, and low energy cut-off of the non-thermal electron, were obtained by fitting the RHESSI HXR spectra with thick target model. An HXR spectrum was generated using the default combination of front RMCs, 1, 3, 4, 5, 6, 8 and 9 in RHESSI GUI, before the flare peak at 17:42:28 UT. We use OSPEX developed by RHESSI team for the fitting (see Figure A.1 in Appendix for the fitting of the spectrum). Using GST (for ribbon width) and SDO/AIA (for ribbon length) imaging data, the area of flare ribbons was estimated to be $5{\times}10^{17}$ cm^2. The non-thermal electron energy flux can be derived using Equation (4.1),

$$F_{nt} \cong 1.6 \times 10^{-9}(\frac{\delta - 1}{\delta - 2})N \cdot E_c \tag{4.1}$$

where $\delta = 5.2$ is the power-law index, N $= 1.44 \times 10^{35}$ electrons s^{-1} is the fitted electron density, and $E_c = 20.6$ keV is the low energy cut-off. The non-thermal

electron energy was estimated to be 10^{11} erg cm^{-2} s^{-1}. Thanks to the work done and published by F-CHROMA (http://www.fchroma.org/) project, RADYN results were ready for use.

According to the HXR parameters described above, we chose the closest available model in F-CHROMA database with the spectral index of 5 and lower cut-off energy of 20 keV. A total flux of 10^{12} erg cm^{-2} was deposit during 20 seconds with a triangular temporal profile (i.e., the peak flux is 10^{11} erg cm^{-2} s^{-1}), and the computation covers 50 s with output at every 0.1 s.

The corresponding atmosphere snapshot from F-CHROMA (RADYN output) was then used as the input of the RH code. The entire atmosphere is involved, and the RH model is initiated with a micro-turbulence velocity set to zero. In particular, we activate the $atoms/MgII\_hk\_PRD.atom$ in RH package, including four levels (one 3S level, two 3P levels, and the Mg III ground level), 2 lines and 3 bound-free transitions, for preparing the atom input for RH. Besides, $H\_6.atom$ is set as active and $C.atom, O.atom, Si.atom$ are set as passive. Figure 4.4 shows the simulated Mg II k line for the moment right before (red) and during (blue) the time when the enhance blue-wing appeared, at t = 7.5 s and t = 8.9 s respectively. We attempted to determine the parameters that make the observed blue-wing enhancement and broadening possible. As shown in Figure 4.4, a thin layer in upper chromosphere with column mass of $10^{-4} - 10^{-3}$ g/cm^2 is around 10^4 K, the typical formation temperature of Mg II line. Compared with the previous time-step (red curves), the atmosphere condition varies significantly when the blue-shift is seen. In particular, the electron density increased by 1.5-2 times and velocity field increased over 4 times, but the change of temperature is minor. This indicates a non-thermal process plausibly caused by precipitating electrons.

One additional adjustment is the micro-turbulence with velocity V_{turb}, suggested by Rubio da Costa et al. [150]. Figure 4.5 (a)-(c) show three Mg II profiles with V_{turb}

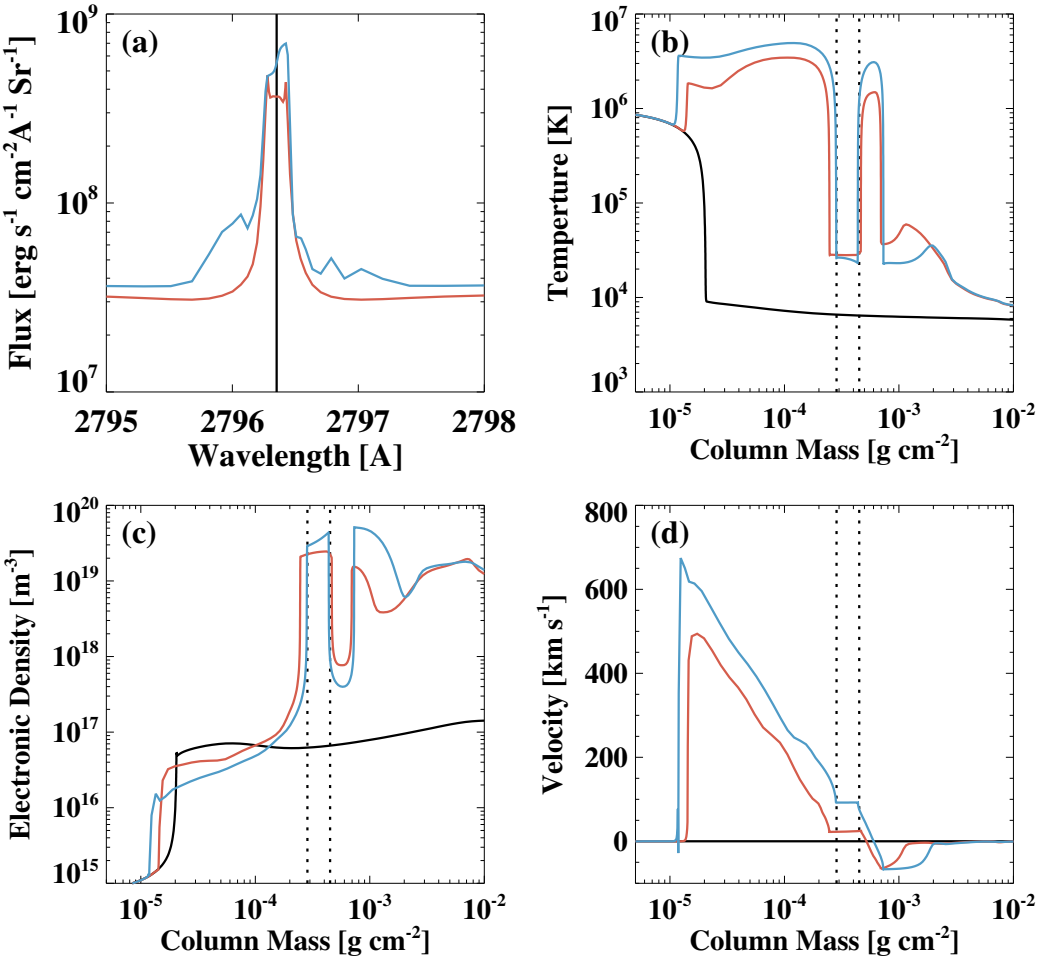

Figure 4.4 Simulation results from RADYN plus RH. Panel (a): Modeled Mg II k line at the initiation period (red), and with blue wing enhancement (blue). Panels (b)-(d): RADYN outputs of atmosphere snapshots as inputs for RH code, in temperature, local electron density and velocity, as functions of column density (height), respectively. Mg II lines are formed within the height range indicated by the vertical dotted lines.

of 10/20/30 km s^{-1}. And in Panel (d), the weighted combination of these three profiles was plotted, showing similar broadening as the observed profile (red). Since there may be multiple drives for line broadening, above are considered to be the upper limit of the micro-turbulence velocity. On the other hand, the strong micro-turbulence removes the blue 'bumps' and convert it into the blue-wing enhancement, which matches the observation. Other parameters that can cause shift and broadening were suggested by previous studies [150, 149], such as the electron density. It is 'pre-determined' by the RADYN results and, therefore, not considered in this study. Note that the modeled intensity could be several times stronger than the observations [150], or even an order of magnitude higher. However, the broadening and Doppler shifts usually match better and are more instructive. We multiplied the intensity of the observed profile by 50 to scale it to the same level of the simulated profile.

In addition, Hα line profiles are extracted directly from the RADYN output. The modeled profiles at different times were shown in the left panel of Figure 4.6. Kuridze et al. studied the Doppler asymmetries in Hα and suggested multiple Doppler components to fit the observed Hα profile [103]. Our Hα observations provide five spectral points, and a comprehensive comparison to modeling is not realistic. Therefore, we construct similar pseudo Doppler signals using $\pm$1.0 Å data from the simulation. The temporal variation of the pseudo Doppler signals was plotted in the right panel of Figure 4.6. The red and blue vertical sticks are marking the timing corresponding to the red and blue plots in Figure 4.4, at t = 7.5 s and t = 8.9 s, when the Mg II line wing is symmetry and has a blue-wing enhancement, respectively. The Mg II blue-wing enhancement occurred shortly before the robust redshift signal of Hα. These evolutions agree with the observations shown in Figure 4.3.

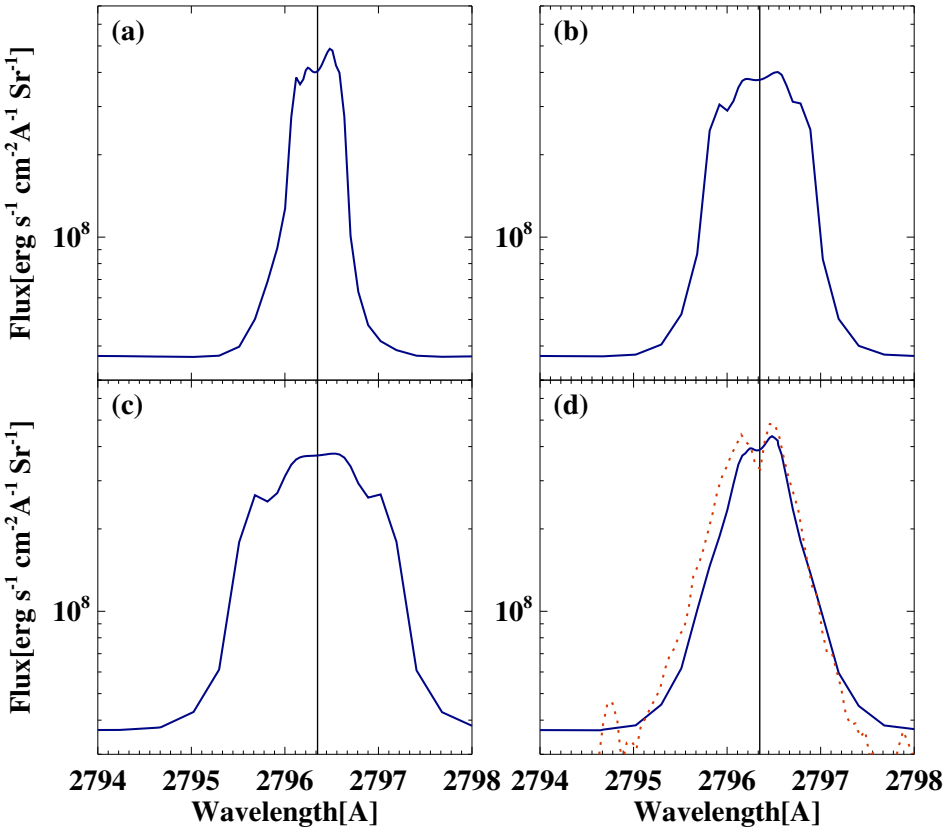

Figure 4.5 Mg II k profiles with different micro-turbulence velocities at 10, 20, 30 km/s in Panels (a)-(c), respectively. Panel (d): The solid blue curve shows the synthetic line profile from the simulation, and the observed profile is shown in red dotted curve

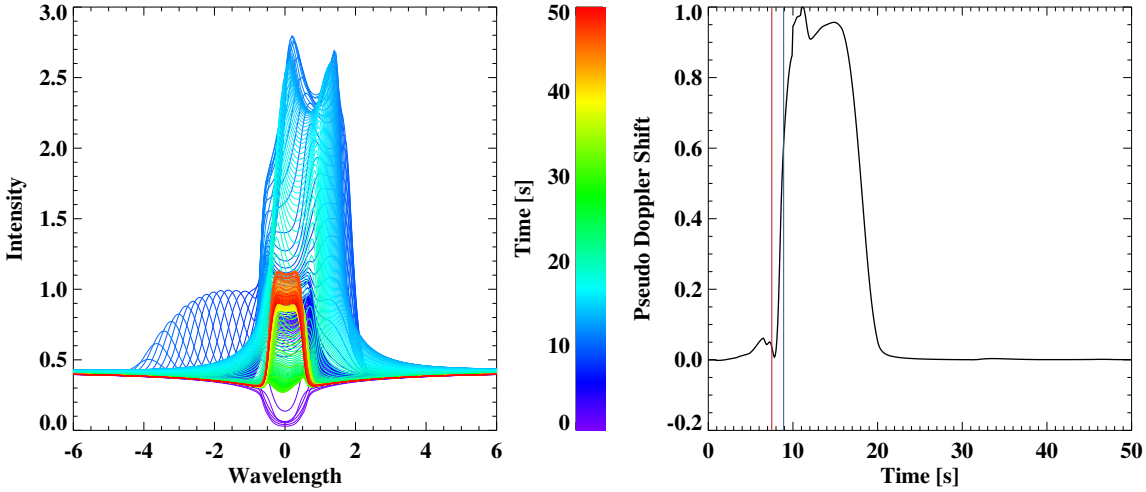

Figure 4.6 Left panel: Hα spectral profiles produced by RADYN at different time, which is shown in the color bar. Right panel: Normalized pseudo Doppler shift of H$\alpha \pm 1.0$Å. The red and blue vertical lines are marking the timing corresponding to the red and blue plots in Figure 4.4, at t = 7.5 s and t = 8.9 s, respectively.

4.4 Summary and Discussion

This study presents observations of an M6.5 flare on 2015-06-22, obtained by IRIS and BBSO/GST. Blueshift and broadening of the Mg II lines are seen prior to the typically observed redshifts in Hα and Mg II lines. The second precursor of this flare occurred right before this blue-asymmetry, which is likely caused by chromospheric evaporation. Numerical modeling by RH, using the results from RADYN, suggests that the broadening is caused by spatially unresolved micro-turbulence, with velocities from 10 to 30 km/s. This is consistent with one of the possible mechanisms discussed in [166]. Strong redshifts are seen in modeled Hα pseudo Doppler diagram, occurred after Mg II blueshift, which agrees with the observations.

The blue wing enhancement in Mg II k line is likely due to the increase of local electron density and velocity field in the atmospheric layer that emits Mg II radiation. We try to construct a physical picture of the reaction of the lower atmosphere to the precipitating electron beams. At the initial stage of the flare, following the second precursor of flare, energetic electrons propagate downward and stop at the

chromosphere. As consequences, the atmosphere around the precipitation site is heated from 10^4 to 10^6 K and the electron density increase continuously, leading to an expansion of this layer, both upward and downward. This layer is then quickly cooled down to 10^4 K, which is favorable to produce Mg II lines. Because of the higher density in the lower layers, the downward expansion is slower and weaker than the upward expansion. Therefore, a broadened Mg II profile is seen with blue wing more enhanced. The downward propagation of heating compresses the lower layer where Hα formed, reflected as strong red-shift Hα line. When the plasma reached the balance, the momentum deposit by the accelerated electron beam dominated and the downward plasma produced the following Mg II lines redshift.

The calculated emission is about an order of magnitude higher than that in previous studies, such as [150]. A standard procedure starts from deriving parameters of the electron beam from HXR observations. One of the initial key parameters is the total flux of electron beam, which is the total number of electrons per second divided by the area of precipitation site. The area estimation varies by the resolution. Note that the background emission also increased proportionally, the normalized line profile is still valuable in qualitative analysis.

Kuridze et al. [103] and Brown et al. [19] studied different hydrogen lines and show asymmetries of optically thick lines in flaring atmosphere. Kerr et al. [94] computed Mg II k line using wave-heated and beam-heated simulations reported a noticeable difference. The line profiles behave in a complicated way, which requires the caution in study. The RH code is time independent, it uses statical equilibrium, which means the populations are equilibrium. Carlsson & Stein [26] studied dynamic hydrogen ionization and noted the effect on hydrogen. To achieve comprehensive understanding of the modeled spectral profiles, more details of population equilibrium for Mg II lines are needed.

CHAPTER 5

COMPARISON OF ENHANCED ABSORPTION IN HE I 10830 Å IN OBSERVATIONS AND MODELING DURING THE EARLY PHASE OF A SOLAR FLARE

The He I 10830 Å triplet is a very informative indicator of chromospheric activities as the helium is the second most abundant element in the solar atmosphere. In Chapter 4, synthetic spectral diagnosis in UV (Mg II) and Hα lines, were presented for the flare emission on the leading front of flare ribbons, where enhanced absorption in He I 10830 Å was reported. In this chapter, more fundamental investigations of the behaviors He I 10830 Å line during flares are carried out. We analyzed the evolution of the He I 10830 Å emission in numerical models and compare it with observations. The F-CHROMA database includes 80 models, with different input parameters, of radiativehydrodynamical (RHD) modeling using RADYN code. The models with injected electron fluxes close to observations are taken into consideration, in particular for the 2013-August-17 flare. The four key models have input parameters of $\delta = 8$, E_c= {15, 20} keV, F = {1$\times$ 10^{11}, 3 $\times$ 10^{11} } erg $\cdot$ cm^{-2}. The modeling results agree well with GST observations in He I 10830 Å , in terms of both the maximum decrease of intensity (-17.1%, compared to the observed value of -13.7%) and the trend of temporal variation (initial absorption phase followed by the emission). All models demonstrate the increased number densities and decreased ratio of the upper and lower level populations of He I 10830 Å transition in the initial phase, which enhances the opacity and forms an absorption feature. Models suggest that the temperatures and free electron densities at heights of 1.3-1.5 Mm should be larger than $\sim 10^4$ K and 6$\times$10^{11} cm^{-3} thresholds for the line to start being in emission. [1]

[1]This chapter is based on the following paper: Huang, N.; Sadykov, V. M.; Xu, Y.; Jing, J. & Wang, H., Comparison of Enhanced Absorption in He I Å in Observations and Modeling

5.1 Introduction

The He I 10830 Å triplet, centered at wavelengths of 10829.081 Å, 10830.250 Å and 10830.341 Å respectively is relatively weak in comparison with other prominent chromospheric lines but represents a powerful diagnostic tool for the chromospheric processes. Since the formation requirements of this line match the condition of upper chromosphere and lower corona, it provides rich information of many observational phenomena, including flares, coronal mass ejections (CMEs), solar oscillations, magnetic field dynamics, and filaments/prominences [198, 70, 104, 71, 192, 51, 151, 109, 185, 7, 108].

Usually, the He I 10830 Å line is seen in absorption against the bright solar disk: in filaments, Hα network, and coronal holes [198, 164, 71, 72]. This line is believed to form in a wide range of heights, from 1.1 Mm [130] to 2.4 Mm [153], and corresponds to the transition between 2^3S_1 and $2^3P_{0,1,2}$ (see Figure 5.1 for term diagram of He I) atomic levels of non-ionized helium. To populate atoms from the ground state parahelium to those higher triplet states, which are so-called orthohelium states, high temperature, and density are required [129, 198, 195]. Such conditions can be provided by radiative or collisional mechanisms [11]. During flares, the He I 10830 Å line turns into emission as the majority of other spectral lines do. Strong emission, several times larger than the background intensity, and corresponding enhanced line broadening, have been reported in several flares of the GOES classes ranging from C-class to X20 [192, 142, 141, 194]. In contrast to the typically-observed enhanced emission, there are reports of the enhanced absorption of spectral lines or continua, also known as "negative flares" [52, 74, 196]. In particular, for the He I 10830 Å line, [185] presented the analysis of two M-class flares showing enhanced absorption appearing on the leading edge of the flare ribbons. Since the two ribbons propagate away from the local magnetic polarity inversion line, their leading edges represent the

during the Early Phase of a Solar Flare, *The Astrophysical Journal Letters, American Astronomical Society*, 2020, 897, L6 [78]

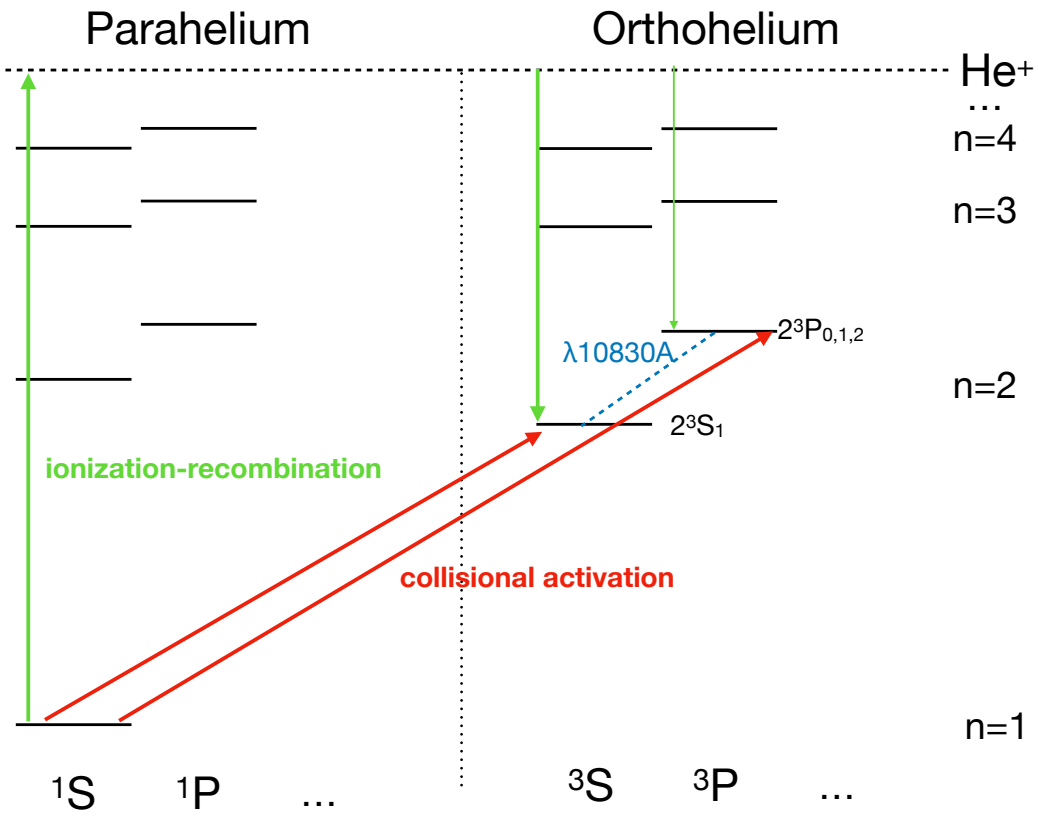

Figure 5.1 The term diagram of He I and schematic transitions. Only transitions directly related to 10830 Å formation are sketched. This line is generated by transition between 2^3S_1 and $2^3P_{0,1,2}$, two orthohelium states. The red arrows denote the collisional activation process, and the green arrows present the ionization-recombination mechanism.

footpoints of the newly-reconnected magnetic loops. In other words, the enhanced absorption occurs at the very beginning of the localized flare heating process.

Theoretical studies mention three mechanisms to populate the orthohelium, namely collisional-activation mechanism (CM), photoionization recombination mechanism (PRM), and collisional-ionization recombination mechanism (CRM) [58, 195, 8, 29]. Photon-activation is forbidden by the selection rule, therefore, only collisional-activation and two ionization-recombination mechanisms are working to populate triplet helium atoms (see Figure 5.1). Under flare conditions, excessive energy input leads to the enhanced absorption of the line at the initial phase, and the strong

emission afterward. Such behavior has been studied numerically by [42], by assuming non-LTE statistical equilibrium approximation for the atomic level populations and hydrostatic equilibrium of the atmosphere in calculations. In this study, we use the advantage of the state-of-the-art RADYN [25, 5, 32, 6] radiative hydrodynamics code results publicly-available under F-CHROMA project. The RADYN models the dynamically-evolving atmospheric response to the energy deposit as a function of time, under the non-LTE non-equilibrium condition (NEC). We make a comparison between one of the observed He I negative flares by [185] with the He I 10830 Å line emission from RADYN simulations with the closest-matching electron beam heating parameters. Then we discuss the possible physical conditions in the chromosphere in reaction to electron beam heating that generate the enhanced He I 10830 Å absorption.

5.2 Description of Observations and Models

Xu et al. [185] presented two M-class flares with the negative contrast in He I 10830 Å, observed by the 1.6 m GST at BBSO. The high-resolution observations showed enhanced absorption in a very narrow spatial region (about 500 km), in front of the normal flare ribbon with strong emission. The maximum decreased in intensity is about -13.7%, comparing with the pre-flare condition. The duration of the intensity drop was about 90 s.

It is well accepted that the energetic electrons precipitating into the atmosphere along the magnetic field lines represent one of the mechanisms of the lower atmosphere heating during flares. To understand the details of how the atmosphere is heated, it is helpful to consider radiative hydrodynamic modeling. RADYN code is one such modeling approach and has been widely used in the community. By assuming non-LTE NEC, RADYN solves hydrodynamic equations and the radiative transfer of the dominating atoms in the solar atmosphere, including helium. Thanks to the

F-CHROMA project, a database of RADYN simulations of flares driven by different electron beams is publicly available online[2]. In these models, the atmosphere heating is caused by the precipitating electron beam with the power-law spectra described by the power-law index (δ), total energy flux (F) and lower energy cut-off (E_c). The output consists of the intensities in different spectral windows, including both spectral lines and continua, the corresponding energy terms, and the stratification of physical parameters of the atmosphere. Each F-CHROMA model outputs 500 time-steps with 0.1 s time interval. The electron heating lasts for 20 s (200 time-steps) and follows an isosceles triangular shape, in which the electron flux increases monotonically from zero to the peak in 100 steps and then decreases back to zero in the next 100 time-steps. For instance, for a model with the total deposited energy of $E_{tot} = 1 \times 10^{11}$erg $\cdot$ cm^{-2}, the electron energy flux, F, reaches 1×10^{10}erg $\cdot$ cm$^{-2}\cdot$s^{-1} value. The starting atmosphere was fixed to VAL-C [171], and the energetic electron transport is solved using the Fokker-Planck equation. In RADYN calculation, the lowest five energy levels of He I, the lowest three energy levels of He II, and the continuum helium are included. These include the ground state helium, the orthohelium states that generate the He I 10830 Å line, and the excited helium.

In order to achieve transitions between 2^3S_1 and $2^3P_{0,1,2}$ levels, the helium atoms need to be populated from parahelium (with two electrons spinning in the opposite direction) ground state to the corresponding triplet states of orthohelium (with two electrons spinning in the same direction). Figure 5.1 presents the schematic transitions in the helium term diagram. According to Pauli's Rule, the direct activating mechanism is limited to the collisional progress, which enables the change of the total spin number. On the other hand, recombination following ionization is also possible to produce orthohelium to generate triplets. Either the PRM by extreme ultraviolet (EUV) back-warming effect from heated corona or CRM by high

[2]`http://www.fchroma.org/`

energy non-thermal electron beams should be considered. In Figure 5.1, the green and red arrows denote the ionization-recombination mechanism and CM, respectively. RADYN is comprehensive for the simulation of He I 10830 Å since it not only includes the transitions that generate the He I 10830 Å triplet explicitly from the numerical perspective, but also considers effects important for the line formation to a certain extent. The F-CHROMA RADYN runs utilized in this work consider the photon-ionization from coronal heating (EUV radiative back-warming) to enable the PRM. The non-thermal as well as thermal collisional ionization rates for the He I and He II species contributing to the CRM are included explicitly in the models [6], but only thermal collisional excitation rates of He I are included in CM.

The electron beam heating parameters for RADYN can be estimated from hard X-ray (HXR) observations taken by the RHESSI [111]. One of the two flares studied by Xu et al. was partially covered by RHESSI on 2013-August-17 [185]. The spectrum of the flare in the initial phase, i.e., during 18:33:16 UT - 18:33:20 UT, was used to retrieve the quantities to describe the precipitating electron beam. The spectrum was fitted using the combination of thermal and non-thermal thick-target (version 2) models in OSPEX (see Figure A.2 in Appendix for the HXR fitting plot). The parameters of the non-thermal distribution of electrons are found to be $\delta = 8.23$, $E_c = 16.9$ keV, and total number of electrons $= 6.58E^{35}$ electrons s^{-1}. Considering the electron precipitation area of $\sim 10^{18}cm^2$ (estimated as the area of RHESSI 25-50 keV sources reconstructed using the CLEAN algorithm), the peak energy flux, F, was calculated using Equation 4.1. It was about 10^{10} erg $\cdot$ $cm^{-2}\cdot$ s^{-1}. Since these parameters are derived using the HXR spectrum not obtained simultaneously with the enhanced absorption of He I 10830 Å, we consider the following multiple values of the parameters of the F-CHROMA model grid: $\delta = 8$, $E_c = 15$ keV and 20 keV, $E_{tot} = 1 \times 10^{11}$erg $\cdot$ cm^{-2} and 3×10^{11}erg $\cdot$ cm^{-2}.

5.3 Results

The F-CHROMA database includes 80 sets of RADYN runs, with different characteristics of electron beams as inputs. As mentioned previously, the exact match of parameters from the RHESSI observation is not available in the F-CHROMA database. Because of that we choose to investigate multiple sets of RADYN runs. RADYN results from four sets of beam parameters with $\delta = 8$, $E_c = 15$ keV and 20 keV, and $E_{tot} = 1 \times 10^{11}$ erg cm^{-2} and 3×10^{11} erg cm^{-2} (also listed in Table 5.1) were considered in detail. We also use the model "val3c_d8_1.0e11_t20s_20keV" (with $\delta = 8$, $E_{tot} = 1 \times 10^{11}$ erg $\cdot$ cm^{-2} and $E_c = 20$ keV) as a representative model which has the closest values to the parameters derived from RHESSI observations in terms of the deposited electron spectra.

Table 5.1 Parameters of The Injected Electron Spectra From The F-CHROMA RADYN Grid Selected According to The Observational HXR Spectrum

F-CHROMA Model #	Total Energy ($erg\ cm^{-2}$)	Low energy Cut-off (keV)	Power-law Index
24	1×10^{11}	15	8
42	1×10^{11}	20	8
30	3×10^{11}	15	8
48	3×10^{11}	20	8

Examples of He I 10830 Å line profiles at five different times for this model are shown in the Panel (a) of Figure 5.2. The BBSO/GST observations were obtained using a tunable Lyot Filter [22] at a fixed bandpass at the blue wing of He I line at 10830.05 $\pm$ 0.25 Å. To make a comparison between modeling and observation, the same spectral window is used for modeled spectra, as shown by the two vertical lines in Panel (a) of Figure 5.2. By integrating the intensities within this bandpass

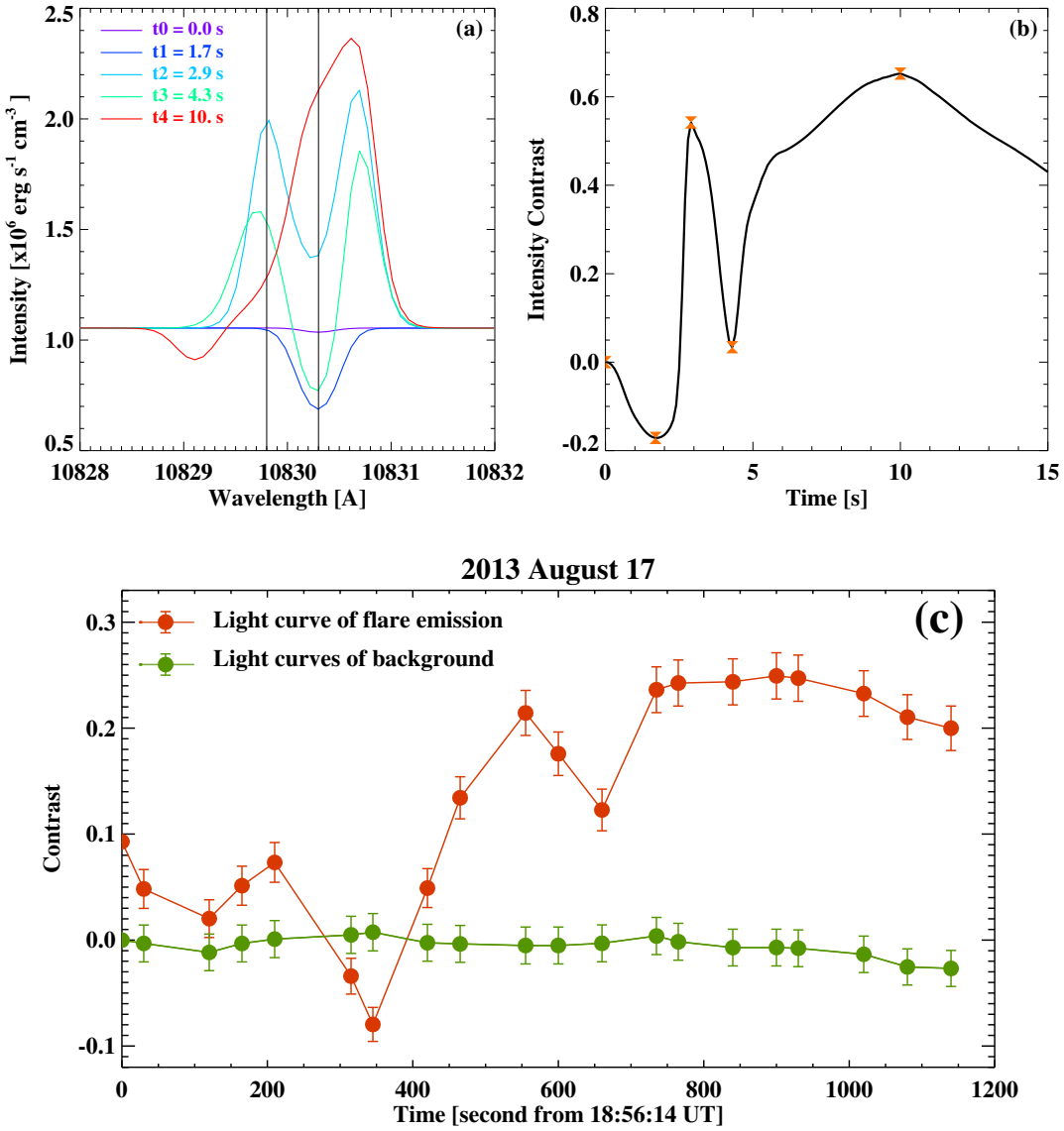

Figure 5.2 Panel (a): He I 10830 Å line profiles at different times, for the RADYN model with $\delta = 8$, total energy of 1×10^{11} erg cm^{-2} and low energy cutoff of 20 kev. Enhanced absorption is seen at t = 1.7 s and turn into strong emission at t =2.9 s. Panel (b): The modeled contrast light curve obtained within the same spectral window as for the observation, shown between the black vertical lines in the left panel. Panel (c): Reproduced light curves of the flaring area and a quiet Sun area (background) from BBSO/GST observation following Xu et al. 2016 [185].

at different times, the intensity from the model was defined. The modeled contrast was calculated referring to the first point, which is considered the pre-flare condition, and the time profile was plotted in Panel (b). During the first 10 s of the pulsation, in which the electron flux was injected increasingly, the line profile developed. For the five sampling timings, representing for pre-flare (t = 0 s), the deepest absorption (t = 1.7 s), the first peak of emission(t = 2.9 s), the second dip (t = 4.2 s), and the maximum of flux injection(t = 10 s), the modeled spectrum lines were plotted in Panel (a) and the timings was marked in Panel (b). In Figure 4 of Xu et al. (2016) [185], the light curve obtained from BBSO/GST observation showed that the enhanced absorption occurred at the initial stage of the flare, and it was followed by emission afterward. We also reproduce this figure in the Panel (c) of the Figure 5.2. It is obvious that the modeled results show a rapid drop of intensity followed by emission, which is similar to the observed temporal variation pattern, although their timescales are different. More importantly, the maximum dimming of the modeled intensity is about -17.1% in contrast to the pre-flare level, which is comparable to the value of -13.7% found in the observation. In addition to the initial absorption feature, we can also see the second dip of the passband emission, which also agrees with the observed behavior. On the other hand, the timescale of the modeled intensity differs from the observations. The duration of the enhanced absorption in observation lasted about 90 s, and the modeled absorption vanishes in several seconds. This discrepancy is likely a result of short timescales of the electron heating (20 s) in the F-CHROMA RADYN runs. The previous study suggested that the timescale of an electron thread heating the atmosphere is on the order of 200 s, and a shorter time span can lead to over-speed and non-realistic evolution [181].

Figure 5.3 shows the light curves of He I 10830 Å blue wing for the four models (see Table 5.1). They are normalized to the first points (which all have the same intensity of 1.037×10^6 erg cm^{-2} s^{-1}). As we can see, all four models give an enhanced

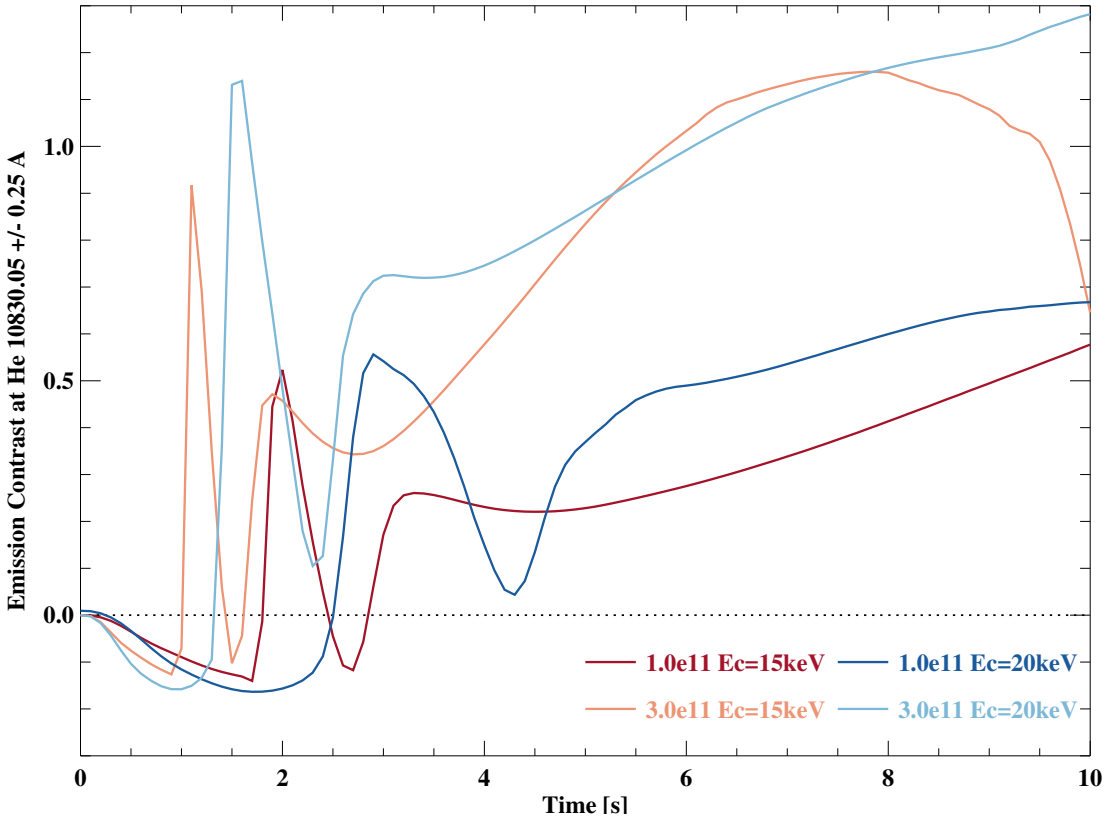

Figure 5.3 The normalized light curves obtained for 4 F-CHROMA models closest to the observations in terms of the HXR spectra parameters. The intensity was integrated over 10830.05 ± 0.25 Å spectral window and normalized with respect to the a same reference level of 1.037×10^6 erg cm^{-2} s^{-1}.

absorption right after the start of the injection of electron beams and turn to emission as most of the solar flares do due to continued precipitation of electrons later in the heating. On the other hand, the duration of enhanced absorption differs from model to model. The trend is that the lower F tends to have a longer duration. Moreover, they are accompanied by weaker emission afterward. The E_c seems to affect the second dip–the short-term decrease of emission. The lower E_c is, the stronger the second dip would be.

To understand the conditions of the atmosphere corresponding to the line absorption and emission phases, we illustrated the temperatures, electron densities, population ratios for levels forming the He I 10830 Å transition, and the contribution

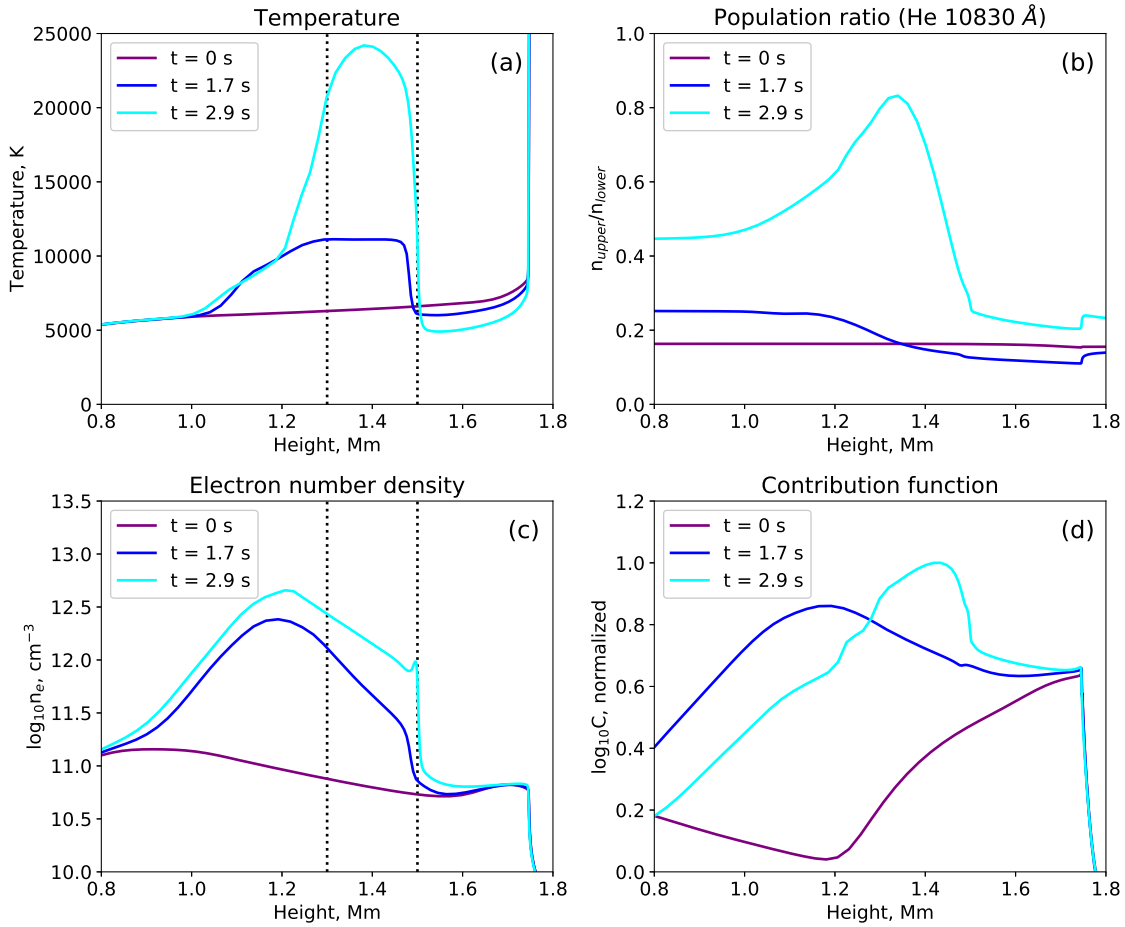

Figure 5.4 Illustration of the (a) temperature profiles, (b) population ratios for He levels forming He I 10830 Å transition, (c) electron number density profiles, and (d) normalized He I 10830 Å line contribution functions averaged over the 10830.05±0.25 Å passband for the selected RADYN model. The electron beam parameters in the model are $\delta = 8$, $E_{tot} = 1 \times 10^{11}$ erg cm-2andE$_c$ = 20 kev. Plots are colored according to the timings using the same color code as in Figure 5.2 (a): the beginning time (dark purple), the time of deepest absorption t = 1.7 s (dark cyan) and the time that the line turns into strong emission t= 2.9 s (cyan). Dotted vertical lines in Panels (a) and (c) mark the 1.3-1.5 Mm height range.

function averaged in 10830.05±0.25 Å passband, for the previously discussed model "val3c_d8_1.0e11_t20s_20keV" in Figure 5.4. As one can see, both the temperature and the density of free electrons become enhanced even during the initial absorption phase of the line evolution. Interestingly, although both number densities of He 2^3S_1 and $2^3P_{0,1,2}$ levels significantly increase, the ratio of populations of He I 10830 Å upper level to lower level (n_{upper}/n_{lower}) decreases at the heights above ∼1.35 Mm during the line absorption phase, and significantly increases when the line is in emission. The contribution function presented in Figure 5.4 (d) also has a significant component at heights above 1.0 Mm, during the line absorption/emission phase.

5.4 Discussion

In this chapter, we presented the analysis of numerical models of He I 10830 Å line emission during the flare heating and compared them with BBSO/GST observations of the M-class flare. We found that:

- An enhanced absorption is reproduced by RADYN simulation at the initial stage of the flare.
- The level of modeled absorption is about 17%, which is comparable with the observed level of 13%.
- A second dip, which was neglected by the previous models but noticed by observations, is also reproduced by the considered models and motivates further analysis.

Theoretically, the He I D3 line turns from absorption to emission at high temperature (T> 2×10^4 K) and plasma density (N> 5×10^{12} cm^{-3}) [197]. In principle, the populations at the two triplet states of $2^3P_{0,1,2}$ and $3^3D_{1,2,3}$, determine whether the D3 line is absorption or emission. A straightforward hypothesis is that similar thresholds may exist for the He I 10830 Å line. The outputs of a RADYN run include the condition of the heated atmosphere (i.e., 'snapshot') and the corresponding spectral line/continuum profiles emitted from such atmosphere snapshots. Figure 5.4

shows an example of the atmospheric stratification in terms of the temperature (a), the ratio of the atomic level populations forming He I 10830 Å transition (b), and electron densities (c). The colors indicate the timing using the same color code as Figure 5.2. Curves from purple to dark cyan to cyan corresponds to the system time from 0 s to 1.7 s to 2.9s, representing for the atmosphere of pre-flare, the deepest absorption, and the first peak, respectively. According to the literature, the formation heights of He I 10830 Å were found to range from 1 Mm to 1.5 Mm [130, 153]. As we see, this agrees well with the behavior of the passband contribution function presented in the Panel (d) of the Figure 5.4, which becomes significantly enhanced above 1 Mm, with the clear peak at ∼1.4 Mm during the emission phase (cyan). As one can see, conspicuous steeps appeared at the height of about 1.5 Mm for all the terms in Figure 5.4, especially in the emission atmosphere. Therefore we determined 1.5 Mm as the upper boundary of formation height in the study. Meanwhile, the lower boundary was set as 1.3 Mm based on the height that (n_{upper}/n_{lower}) decreased. The two thermodynamic parameters, temperature and electron number density, presented a significant increase within this height range. In the first 1.7 seconds of the heating, the electron number density increased rapidly from about $1.4\times10^{11} cm^{-3}$ to $2.4\times10^{12} cm^{-3}$, while the temperature changes from about 6,500 K to 11,000 K. During the following seconds (dark cyan to cyan, t = 1.7 s to t = 2.9 s) the number density increases less intensively to about $4.4\times10^{12} cm^{-3}$, while the temperature kept constantly increasing to around 23,000 K. During this period, the integrated line intensity of He I 10830 Å changes from enhanced absorption to emission. Therefore, the inferred watershed of emission and absorption in the He I 10830 Å line for the representative run is the condition of $T>2\times10^4$ K and $n_e\geq 4\times10^{12} cm^{-3}$.

To confirm the existence of thresholds in general, we consider all 80 RADYN models available in F-CHROMA. It is necessary to mention that all models demonstrate the initial absorption in the He I 10830 Å passband, followed by the

htpb]

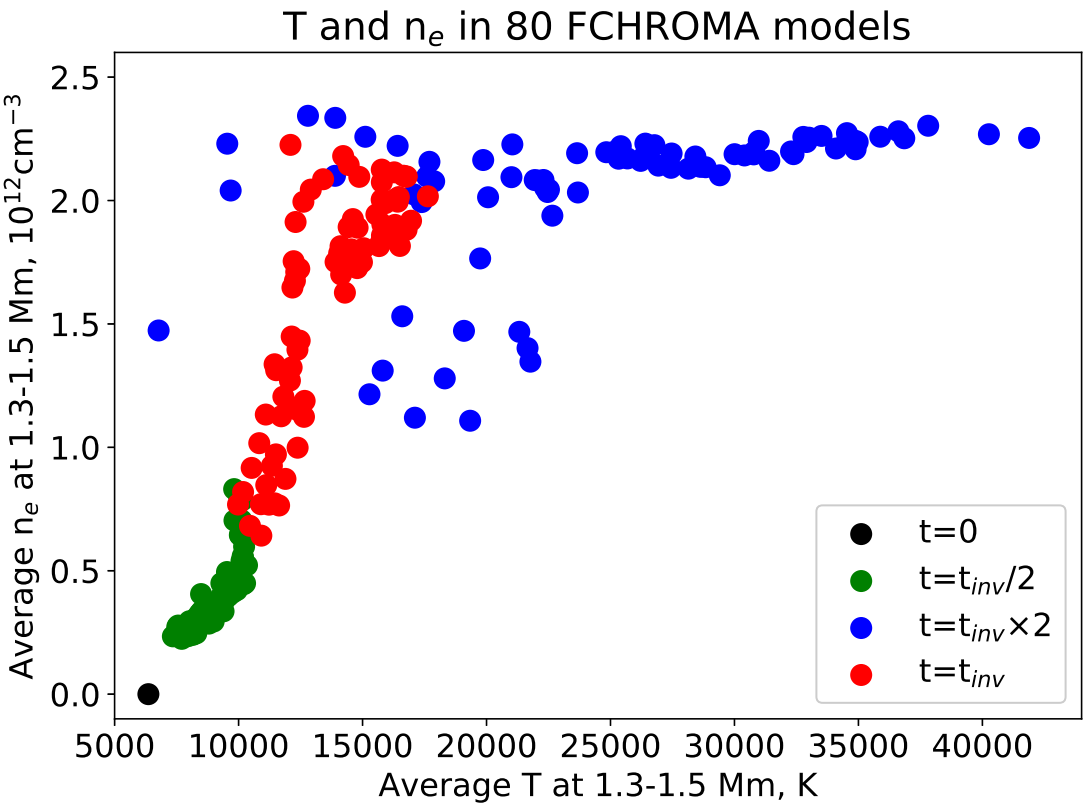

Figure 5.5 Distribution of temperatures (T) and electron number densities (n_e) averaged at 1.3-1.5 Mm height for 80 available RADYN F-CHROMA models. Red points correspond to the T and n_e values at the time when the line intensity obtained at 10830.05±0.25 Å turns from absorption to emission (t_{inv}), green points — to twice shorter time ($t_{inv}/2$), blue points — to twice longer time ($t_{inv}\times2$). Black point marks the initial atmospheric conditions for each run.

emission. We consider the temperatures and electron densities averaged at 1.3-1.5 Mm heights for these models at the time when the absorption changes to the emission (t_{inv}), as well as at the twice shorter and longer times. The scatter plot presented in Figure 5.5 demonstrates that temperatures and electron densities during t_{inv} are distinguishable from those during the absorption (green) and emission (blue) phases. On average, the temperature at 1.3-1.5 Mm heights should be above 1.3×10^4 K, and the electron density should be above $1.4\times10^{12}\, cm^{-3}$ for the line to turn into emission. It is also important to mention that the temperatures and electron densities averaged over other heights demonstrate less clear separation between the absorption and emission phases with respect to 1.3-1.5 Mm range.

Both energetic non-thermal electrons and EUV shortward of 504 Å from heated corona can ionize the helium atoms from the ground state. A high ionization-recombination rate would populate the orthohelium. Especially for the metastable state of 2^3S_1, it occupies 2/3 of the orthohelium atoms and can be "overpopulate". This overpopulation of the lower level of He I 10830 Å transition (see Figure 5.4c for details) would result in enhancement of the absorption [195]. Previous studies often focus on CRM [42, 185] for flare emission. Our study confirms that the non-thermal atomic level populations corresponding to the He I 10830 Å transition increase fast during the absorption enhancement at the formation heights of He I 10830. This would increase the collisional-ionization and recombination rate and overpopulate the lower level of the He I 10830 Å transition with respect to pre-flare (initial) conditions, as evident in Figure 5.4b. On the other hand, PRM was believed to be dominant in the formation of He I 10830 Å line. During the flare initial phase, the back-warming effect, resulting in a stronger photoionization effect, would also contribute to the population of helium 2^3S_1 state. Theoretically, the amount of triplet triplet helium should be proportional to the EVU shoter than 504 Å, which is generated in the preheated corona. When the upper chromosphere

was heated, the higher rate of direct collisional excitation by thermal electrons would raise the occupation of both excited energy level and turn the line into emission. The temperature we retrieved from the model, 23,000 K, agreed with the theoretical required temperature of Lyman plateau around 25,000 K [126].

In this study, the electron precipitation area is estimated as a RHESSI 25-50 keV HXR source area (within 50% contour level) reconstructed with the CLEAN algorithm. This is a widely-used but simplified approach that likely leads to overestimated precipitation areas. Correspondingly, the derived energy flux of F = $10^{10}\ erg \cdot cm^{-2} \cdot s^{-1}$ is likely a lower limit. The precipitating electrons are confined by the magnetic field lines, which are converging from the corona to the chromosphere. As a consequence, the flaring areas become smaller in the deeper atmosphere [187]. For instance, considering the width of the flare ribbon measured by [185] and the ribbon length observed by SDO/AIA 1700 Å, the source area is about $3 \times 10^{17}\ cm^2$. Consequently, the energy flux becomes F = $\sim 10^{11}\ erg \cdot cm^{-2} \cdot s^{-1}$ as estimated from observations. This should be compared against the F-CHROMA models of at least $E_{tot} = 1 \times 10^{12}\ erg\ cm^{-2}$, $\delta = 8$, E_c = 15 keV and 20 keV, which are not currently available in the database. On the other hand, the total energy flux does not appear to impact the presence of the absorption or the formation condition of the He I 10830 Å line. The higher energy flux may be able to bring the absorption forward due to its faster electron injection rate. For a better understanding of the impact of different electron injection on the time evolution of He I 10830 line, a further study focusing on evolution and expanded to more models is required.

CHAPTER 6

TRANSIENT ROTATION OF PHOTOSPHERIC VECTOR MAGNETIC FIELDS ASSOCIATED WITH A SOLAR FLARE

The fundamental physics involving the flare energy release, transfer, and deposition have been studied extensively. As discussed in the previous chapter, special characteristics, such as the enhanced absorption, Dopplar shift, line broadening, have been observed and studied on the leading ribbon front. It is known that the leading ribbon front represents the newly connected flare loops and therefore their footpoints are the signatures of the initial pulsation of electron beams. Besides the spectral signals, this chapter presents a sudden rotation of vector magnetic fields, about 12°-20° counterclockwise, on the leading front of the flare ribbons. Unlike the permanent changes reported previously, the azimuth-angle change is **transient** and co-spatial/temporal with Hα emission. The measured azimuth angle becomes closer to that in potential fields, suggesting untwist of flare loops. The magnetograms were obtained in the near-infrared at 1.56 μm, which is minimally affected by flare emission, and no intensity profile change was detected. The results suggest that these transient changes are real and discuss the possible explanations in which the high energy electron beams or *Alfvén* waves play a crucial role. [1]

6.1 Introduction

It is well accepted that many solar flares, and other violent eruptions, such as coronal mass ejections (CMEs), result from magnetic reconnection occurring in the corona. However, many manifestations are visible in the lower solar atmospheres, i.e., the

[1]This chapter is based on the following paper: Xu, Y.; Cao, W.; Ahn, K.; Jing, J.; Liu, C.; Chae, J.; Huang, N.; Deng, N.; Gary, D. E. Wang, H. "Transient rotation of photospheric vector magnetic fields associated with a solar flare", *Nature Communications, Springer Science and Business Media LLC* ,2018, volume 9, 46 [184]

chromosphere and photosphere. In addition to the radiation, significant changes in the magnetic fields have been observed in the literature [176, 191, 163, 49, 178, 20]. Most of them are permanent changes, while transient changes are rarely reported, and are suspected of being instrumental artifacts.

Permanent magnetic changes are irreversible phenomena of photospheric fields in reaction to the flare impacts, usually during strong flares higher than M-class. Shear flows measure horizontal motions of magnetic features along both sides of the magnetic polarity inversion line (PIL). Previous observations show the spatial correlation between strong shear flow and flare emission [191, 38]. More importantly, shear flow can drop significantly after the flare [163, 179, 178], indicating that a certain amount of magnetic free energy has been released. Tilt angle, also known as the inclination angle, is determined by the ratio between vertical and horizontal magnetic components. During flares, the reconnection rearranges the topology of magnetic loops and the tilt changes consequently. Direct measurements of vector fields have shown that horizontal fields increase near the PIL and decrease in the nearby penumbral regions during flares [193, 179, 20]. As a consequence, sudden intensity changes of magnetic features (usually the penumbra) are observed [176, 175, 177, 113]. Bodily rotation is one of the intrinsic properties of sunspots or sunspot groups first observed by Evershed (1910) [46], which are usually gradual and continue during the entire lifetime. On the other hand, rapid rotations associated with X-class flares were reported [9, 178] and attributed to the torque introduced by the change of horizontal Lorentz force [85]. Using the data with higher spatiotemporal resolution obtained by the 1.6 m BBSO/GST [60, 22], the sudden rotation is found to be nonuniform and synchronous with the flare ribbon propagation [114].

In contrast to the stepwise temporal profile in permanent changes, the characteristic profile of a transient change is more like a δ function in time. Transient changes were rarely observed in the literature. An example is a magnetic anomaly or magnetic

transient, a temporal reversal of magnetic polarities measured simultaneously with flare emission, first reported using BBSO data [140, 199]. The plausible explanation is that the profile of the Fe I line at 5324 Å, used for the magnetic measurements, turned from absorption to emission due to the flare heating at lower layers of solar atmosphere [140]. From space-based observations, magnetic anomalies were reported during an X5.6 flare observed by the Michelson Doppler Imager (MDI) on board SOHO [146] and an X2.2 flare observed by the SDO/HMI [122]. The authors drew similar conclusions that the apparent polarity reversal is a consequence of the line profile change. Thus, these magnetic anomaly/transient reported not intrinsic to the Sun, but an artifact in magnetic measurements due to the change of line profile.

In this chapter, we present 1.56 μm vector magnetograms with the highest cadence and resolution ever obtained, which are much less subject to line profile changes, yet reveal a sudden increase of the azimuth angle. An M6.5 flare was well observed on 2015-June-22, with BBSO/GST using multiple channels, VIS tuned to the Hα line, BFI tuned to a continuum near the TiO line at 7057 Å (see Figure 2.7), and the NIRIS providing vector magnetograms using the Fe I line at 1.56 μm. The image scale of the vector magnetograms was about $0''.083$ pixel^{-1} and the cadence was about 90 s for a full set of Stokes measurements. The Fe I Stokes profiles were measured at 40 different spectral positions. The spectral resolution is much higher than that on space-based spectropolarimeters (e.g., MDI and HMI), and it permits a check of possible changes in line profile due to enhanced emission, which is not seen.

The flare started around 17:39 UT and peaked at 18:23 UT in GOES 1-8 Å soft X-rays. It lasted for several hours, and our interest in this study focuses on the initial phase within the core region of the flaring areas. The host active region NOAA 12371 was close to the solar disk center at that time, and therefore the geometric projection effect is small and was corrected easily. From the time sequence of azimuth maps, we clearly see a ribbon-like structure moving co-spatially and co-temporally with the

flare emission in the Hα line. On average, the azimuth angles increased by about 12° - 20°, indicating the local magnetic fields rotated counterclockwise. In contrast to the permanent changes of magnetic field, the azimuth change is a transient variation, which restored quickly to its original value after the flare ribbons swept through. By reviewing the existing models, such as *Alfvén* waves and induced magnetic fields, we found that they may play important roles but can not solely explain the observation.

6.2 Results

6.2.1 Overview of the Flare

Two major flare ribbons were identified in the core area of the flare. The eastward-moving ribbon resides in the area of positive magnetic polarity, and the westward-moving ribbon propagates in the region with negative magnetic polarity. We focus on the eastern ribbon, where azimuth angle increases are much more apparent. A change of azimuth angle can also be identified with the conjugate flare ribbon within negative magnetic fields, but it is dispersed and too weak to be precisely measured. The elongated flare ribbons represent multiple footpoints of parallel flare loops. For each individual loop, the change of azimuth angle on its footpoints indicates a twisting or untwisting of the loop. To determine whether the twist of the loop is increased or decreased, the difference between the azimuth angles of the measured magnetic field and that of the extrapolated potential fields are calculated, in which the latter was extrapolated with the Fourier transformation method [4, 57]. As one will see below, the vertical component of the magnetic field ($\mathbf{B}_z$) and the extrapolated potential field ($\mathbf{B}_p$, derived from $\mathbf{B}_z$), remains nearly constant during the flare. Therefore, the comparison of transverse components of observed and extrapolated fields, represented by the azimuth angle, can, in principle, indicate the variation of the twist.

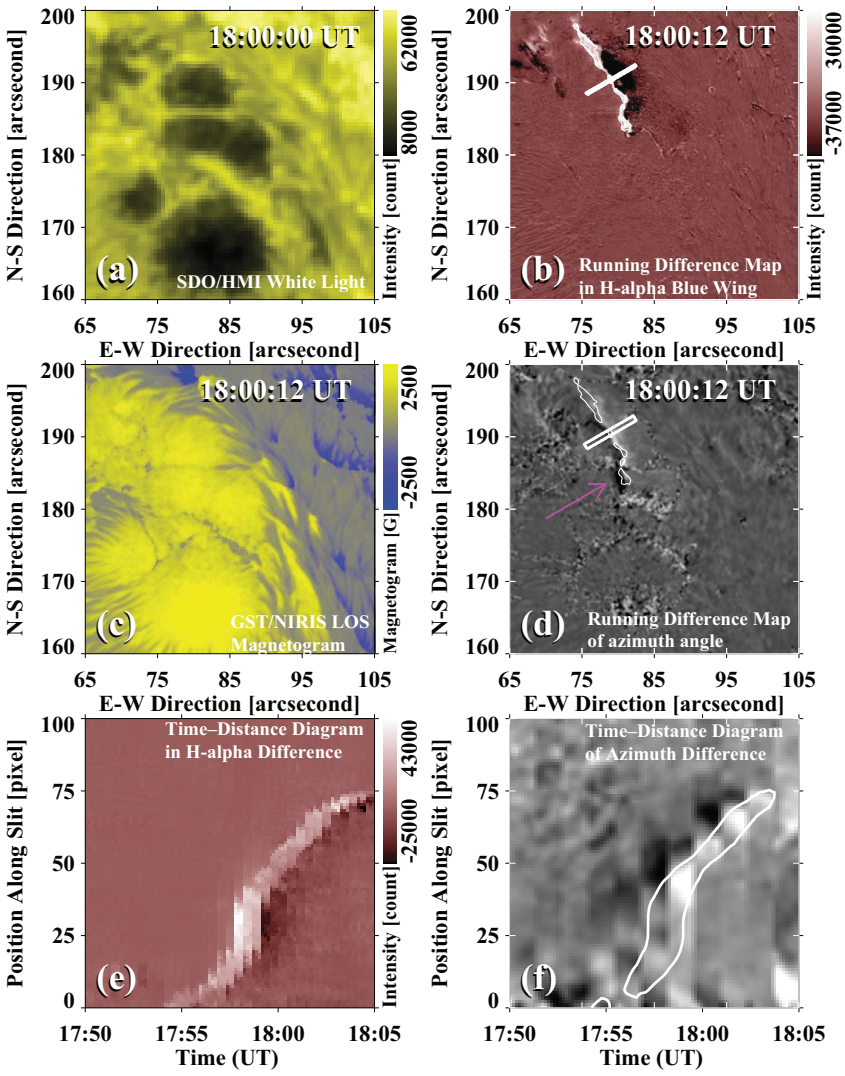

Figure 6.1 Azimuth angle changes in association with flare emission. All of the four images (first and second rows) were taken simultaneously at the flare peak time (18:00 UT) in a common FOV of 40″ by 40″. **(a)**: SDO/HMI white light map.(b): Running difference image in Hα blue wing (-1.0 Å), showing the eastern flare ribbon. The bright part is the leading front and the dark component is the following component. **(c)**: GST/NIRIS LOS magnetogram, scaled in a range of -2500 (blue) to 2500 G (yellow). **(d)**: Running difference map of azimuth angle generated by subtracting the map taken at 17:58:45 UT from the one taken at 18:00:12 UT. The dark signal pointed to by the pink arrow represents the sudden, transient increase of azimuth angle at 18:00:12 UT. The white contours outline 60% of the maximum emission of the Hα ribbon front. **(e)**: Time–distance diagram of Hα difference maps. The slit position is shown in Panel (b). The time period is from 17:50 UT to 18:05 UT. **(f)**: Time–distance diagram of azimuth difference maps. The slit position is shown in Panel (d). The time period is from 17:50 UT to 18:05 UT. The white contours outline 15% of the maximum emission of the Hα ribbon front in Panel (e).

6.2.2 Characteristics of the Azimuth Angle Variation

From a movie that shows the time sequence of azimuth angle within a field of view (FOV) of the flare core region, one can see a ribbon-like feature propagates from right to left. [2] This disturbance of azimuth angle along a narrow ribbon is co-spatial and co-temporal with the flare emission seen in Hα. In the Panel (d) of Figure 6.1, a running difference map of azimuth angle is shown at 18:00:12 UT. The dark feature indicated by the pink arrow represents the change of azimuth angle, and the white contours show the leading front of the Hα emission, indicating a close relationship with precipitating electron beams [185]. The slight offset of about 300 $\sim$ 500 km could be a projection effect, because the formation height of Hα is about a few thousand km higher than the formation height of the NIR line at 1.56 μm.Other Panels show the SDO/HMI WL image (Panel (a)), a running difference image of Hα blue wing (-1.0 Å) (Panel (b)), and LOS magnetogram derived from NIRIS data (Panel (c)). All of the images are within the same FOV, where the ribbon of interest resides. To examine the azimuth change, we resolved the 180° azimuthal ambiguity in the transverse field using the minimum-energy method [123] and removed the projection effects by transforming the vector magnetogram from observational image plane to heliographic-cartesian coordinate. Panel (e) presents a time-distance diagram of the running-difference Hα images. The slit is 3-pixel wide, and its position can be found in Panel (b). The bright feature represents the ribbon front of Hα emission, similar to the one in Panel (b). In Panel (f), we display the time-distance diagram of running-difference images of the azimuth angle. The slit width was 9 pixels, because the cadence of the vector magnetogram is 90 s, about 3 times of the cadence of Hα images. The white contour indicates the location of Hα enhancement in Panel (e). It shows a good correlation between Hα emission and azimuth-angle change at different times. Such a correlation does not vary much at different slit positions.

[2]See the link for Supplementary Movie://www.nature.com/articles/s41467-017-02509-w

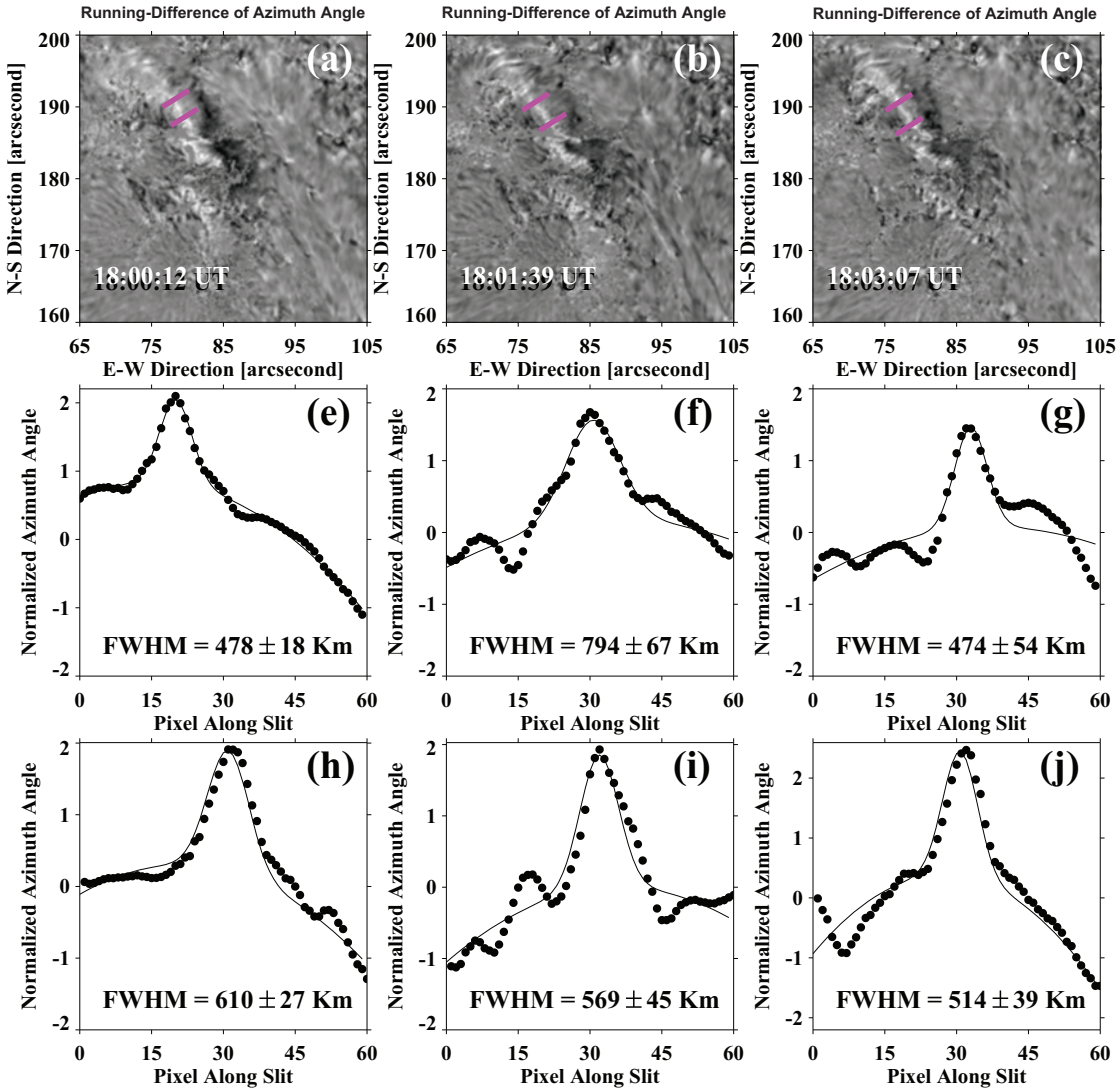

Figure 6.2 Characteristic sizes of the region of azimuth angle deviation. **(a) - (c)** Sparse running-difference maps of azimuth angles, taken at three representative times. (d) - (f): Azimuth angle profiles along the top slit shown in each image in Panels (a) - (c) and the corresponding Gaussian fits. (g) - (i): Azimuth angle profiles along the lower slit shown in each image in Panels (a) - (c) and the corresponding Gaussian fits. The FWHM, derived from the fitting, is used as the ribbon width of azimuth change, which is about 570 km on average.

The characteristic sizes of ribbon-like features are fundamental parameters. For instance, the ribbon front, which is the precipitation site of electrons, is found to be very narrow [92, 157]. We follow the method described in Xu et al. (2016) [185] and Jing et al. (2016) [92] to measure the width of the azimuth ribbon, as shown in Figure 6.2. We use sparse running difference maps (the reference image is taken several frames prior to the target) to minimize the background noise. On average, the width of the region of azimuth angle deviation is about 570 km, which is comparable to the size of the dark ribbon (340 - 510 km) in helium 10830 Å [185]. It is not easy to measure the ribbon length quantitatively as the ribbon is segmented and noisy near the two ends. We estimate the length manually using the image taken at 18:00:12 UT and the result is about 13,300 km.

6.2.3 Temporal Evolution of the Azimuth Angle Change and Correlation with Hα Emission

In order to study the temporal evolution of the disturbance, three representative regions (R1, R2, and R3, marked using white color) are selected on the propagating path of the azimuth transient, as shown in Panel (a) of Figure 6.3. These representative slits are selected in the middle of the ribbon and away from the sunspot boundary, where the magnetic fields are also affected by the sudden sunspot rotation [114] in a more gradual manner. The corresponding temporal profiles are plotted in Panel (b). The uncertainties are estimated using the points prior to the initiation of the flare. For instance, the standard deviation of the first 12 points is used as the error in R1. Let us use R3 as an example. The average azimuth angle suddenly increases by about 20°, from the pre-flare value of 11.7° to the flare peak time value of 31.5°, with an uncertainty of 6.6°. Therefore, the azimuth peak is significant as it is about three times of the uncertainty. In particular, we see that the azimuth peak coincides with the Hα emission (dashed curve), based on the results shown in Figures 6.1 and 6.3. For the other two regions, R1 and R2, the horizontal field rotates

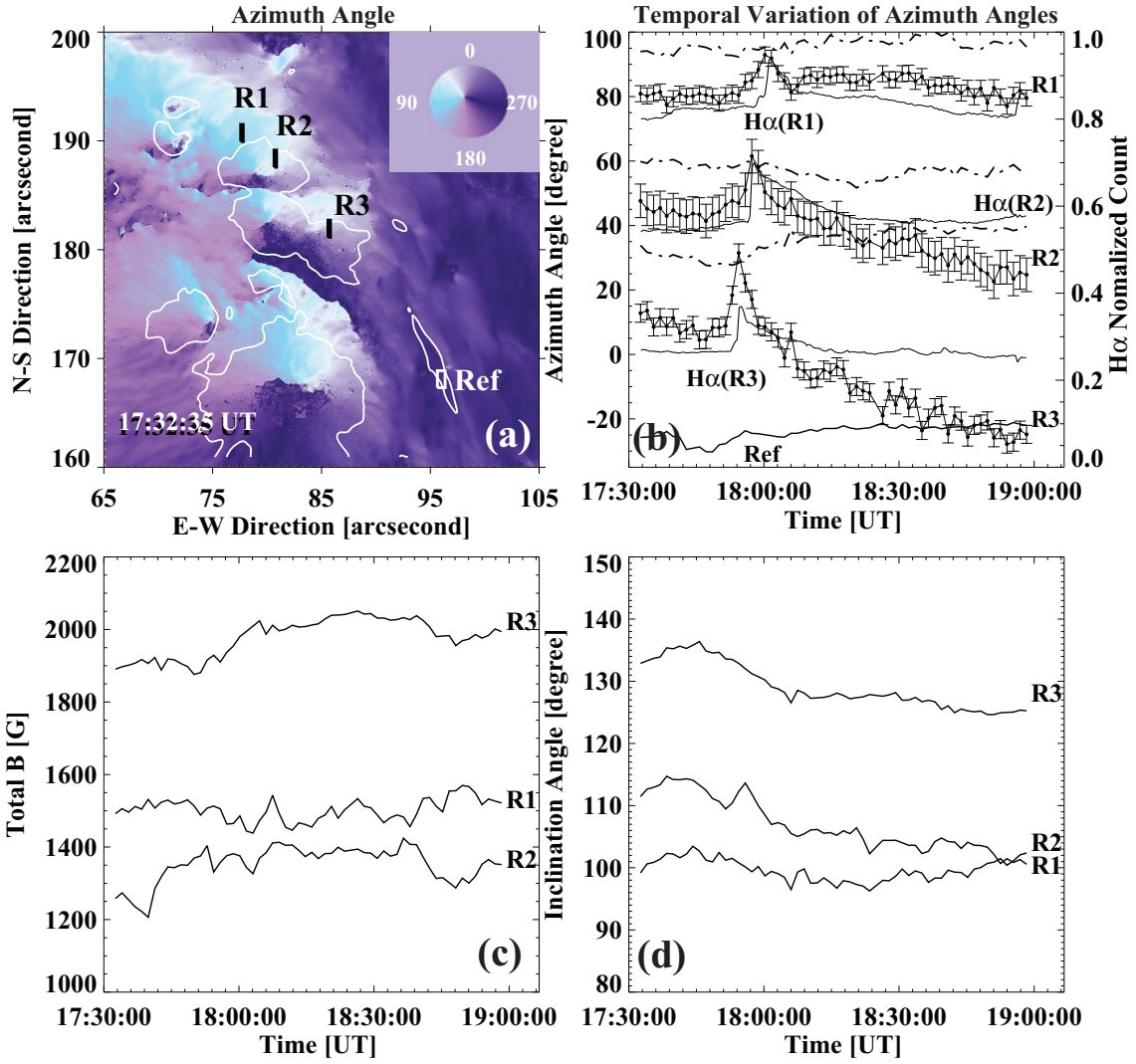

Figure 6.3 Temporal evolution of azimuth angle deviation. **(a)**: Azimuth angle map taken before the flare at 17:32:35 UT. Three slits are put on the regions of interest (R1-3), plus a reference region in the lower right corner. The white contours outlines the sunspot umbral areas (>1800 G). **(b)**: The curves with error bars are the temporal variation of averaged azimuth angle within regions of R1-3. The uncertainties are estimated using the standard deviation of the pre-flare data points. The peaks are more than three times of the uncertainties render themselves statistically significant. The flare time is determined by the Hα light curve, for instance the dashed line is the Hα light curve of R3, in which the peak matches with azimuth angle peak in R3. All Hα light curves are in natural log space and self-normalized to their peak emission. In the bottom, the temporal variation of the azimuth angle in the reference region is plotted, which is manually increased by 50° to match the plotting range (50° - 190°). The dotted-dash curves are the azimuth angles of extrapolated potential fields that remain certain levels above the azimuth angles of real fields. **(c)**: Temporal variation of averaged magnetic flux strength within the representative areas. **(d)**: Temporal variation of averaged inclination within the representative areas.

by 12° and 18°, with uncertainties of 2.5° and 5.2°, respectively. Using the potential field extrapolation, the azimuth angle of the potential field is determined and plotted as dot-dash curves in Panel (b). We see that the potential field azimuth remains at a certain level above the azimuth angle of the vector fields. Only at the flare peak time, the measured azimuth angle becomes closer to that in the potential field due to the sudden rotation. This is a 2D comparison but is a good proxy of the 3D configuration because the extrapolated potential fields are based on the measured vertical component, which did not vary as the azimuth angle did during the flare. Therefore, the difference of the magnetic shear between the measured field and the potential field can be represented by the azimuth angle, which is determined by the horizontal components of B_x and B_y. In the Panels (c) and (d) of Figure 6.3, the total magnetic strength and the inclination angle are plotted as a function of time, respectively. These curves contain noise-induced fluctuations, and no impulsive peak is identified as in the azimuth transient. An area (white box) is selected far away from the flare ribbons and used as a reference compared to the regions with significant azimuth angle changes. We see irregular fluctuations but indeed no obvious peak associated with flare emission.

6.3 Discussion

In summary, this chapter present a clear transient change of azimuth angle, associated with propagating flare ribbons, which are footpoints of 3D magnetic loops. The major results are as follows:

- The local magnetic vectors rotated about 12° to 20° simultaneously with flare emission.
- The strong correlation between the azimuth transient and flare ribbon front indicates that the energetic electron beams are very likely to be the cause.
- The measured azimuth angle becomes closer to that in the potential field indicating a process of energy release (untwist) of the flare loop.

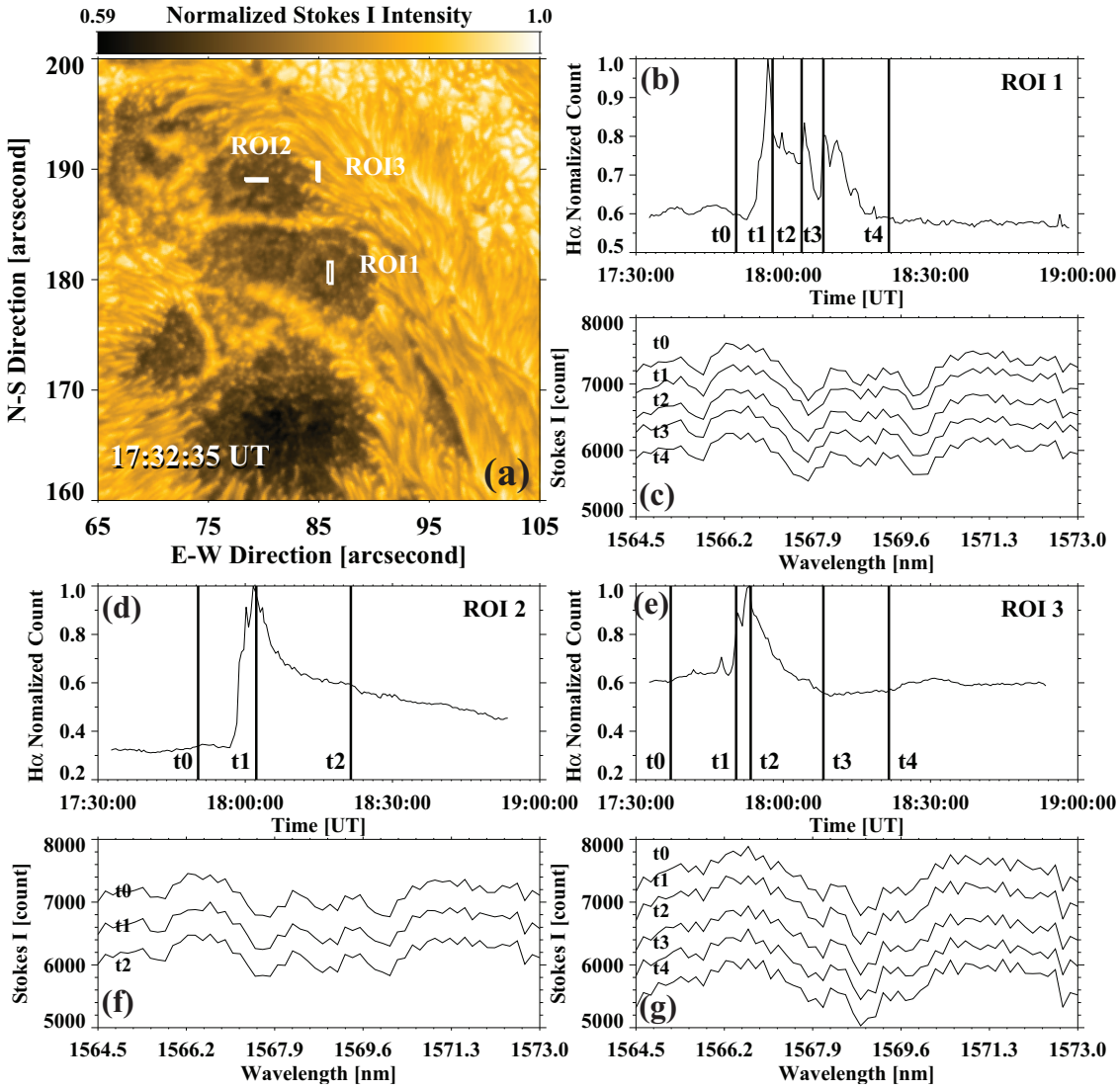

Figure 6.4 Intensity profiles of the NIR line at 1.56μm during the flare. **(a)**: Stokes I component taken at 17:32:35 UT. The intensity is normalized to the maximum count as shown in the color bar. Three representative areas are mark using white boxes (ROI1, ROI2 and ROI3). **(b)**: Hα light curve in ROI 1. The vertical lines indicates five time points before, during and after the flare. The corresponding NIR intensity profiles (Stokes I) are plotted in **(c)**, from which we see almost identical line profiles indicating that the flare heating almost has no effect in this deep layer of solar atmosphere. (d): Hα light curve in ROI 2. The corresponding NIR intensity profiles, at t0, t1 and t2, are plotted in **(f)**. **(e)**: Hα light curve in ROI 3. The corresponding NIR intensity profiles, at t0, t1 and t2, are plotted in **(g)**.

Firstly, the observed field change is different from the magnetic anomaly reported previously. In that scenario, the profile of the spectral line used to measure the magnetic fields has changed. In our case, the line profiles remain in absorption and unchanged during the flare, as shown in Figure 6.4. It is not surprising as the spectral line used by NIRIS is the Fe I line at 1.56 μm, which is formed very deep in the photosphere where almost no flare heating can reach except in some extremely strong flares [188]. In addition, we investigate the polarized raw data before inversion is done. On the Stokes I, Q, U and V maps as shown in Figure 6.5, an area similar to R3 is selected, and the corresponding profiles before and during the flare are plotted. As we can see, the Stokes I and V components, in which V represents the circular polarization and determines the LOS magnetic fields, remain almost identical. However, the Stokes Q and U components that determine the transverse fields, vary significantly. Therefore, we believe that azimuth change is real from Stokes Q and U components and not affected by either flare emission or circular polarization.

This is the first time that transient field rotation is observed. We attempt to explain the effect by considering several existing models, which are discussed below.

The *magnetic field induced by the electron beams* is the most straightforward and intuitive model. The basic idea is that the penetrating electrons produce induced magnetic fields, which act on the original fields such that the combined fields point to new directions. This is equivalent to a field rotation. The downward precipitation of electrons, with negative charges, is equivalent to an upward current. According to Ampère's circuit law, the self-induced magnetic field is generated around the ribbon. The ribbon width is much smaller than its length so that the latter can be treated as a half infinite wall. Therefore, to the left side of the ribbon front, the self-induced magnetic field points to the south (in solar coordinates), and the overall field will rotate counterclockwise. To the right side, the overall field will rotate oppositely, which, however, will be balanced by the self-magnetic field of the trailing electron

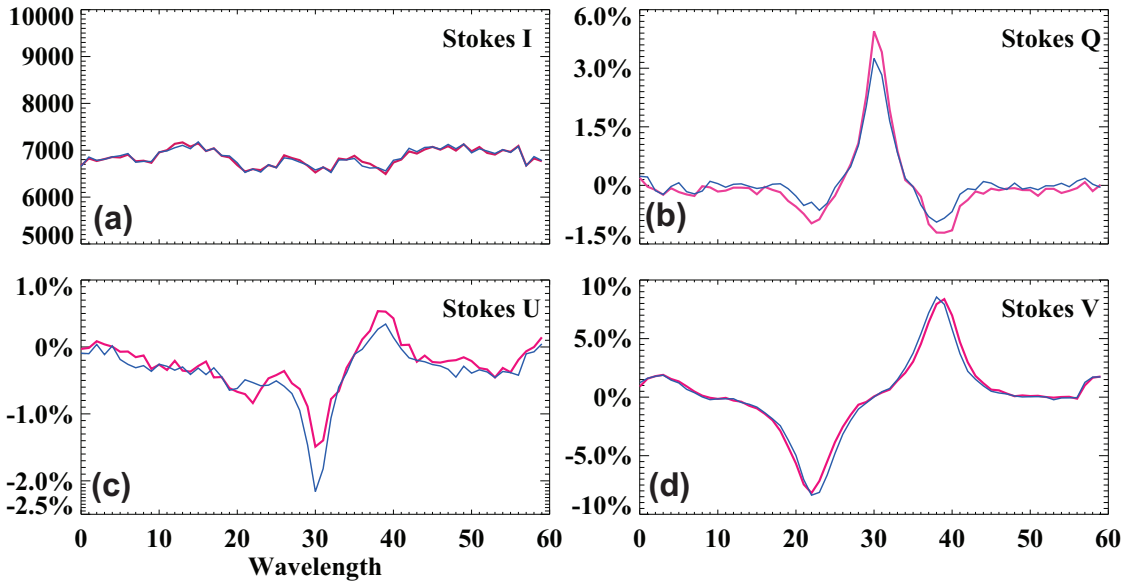

Figure 6.5 Stokes profiles before and during the flare. Stokes components (I, Q, U, & V) taken near R3 before (blue) and during (pink) the flare. **(a)**: Stokes I. **(b)**: Stokes Q. **(c)**: Stokes U. **(d)**: Stokes V. It is clear that the Stokes I and V components remains almost unchanged but Q and U components are significantly affected during the flare.

beams that have decreased but have not been turned off. We can estimate the required current I using Ampère's law, $\oint \mathbf{B} \bullet d\mathbf{s} = \mu_0 I$, in which the integration loop is $2l$ (two times the ribbon length, which is about 2×10^7m). In order to induce a magnetic field of order 100 G, the required current is about 1.6×10^{11} A, or an electron flux of 10^{30} s^{-1}, a tiny fraction of the total electron flux ($\sim 10^{35}$) with energy greater than 20 keV derived from the RHESSI HXR spectra. The relative orientation between the original fields and the flare ribbon determines whether the azimuth angles of the combined fields increase or decrease. If this angle is larger than 90°, an increase is seen in front of the flare ribbon. The rotation effect is canceled out behind the flare ribbon by the following opposite rotation effect. Since the fields point outward from a sunspot center, when the ribbon passes through the sunspot, the relative orientation changes and the azimuth angle should decrease. However, such an increase-decrease

pattern was not observed. Although the magnitude of the induced field matches with observations, the direction does not match.

The second model considers the effect of *downward-drafting plasma* [165], which in our case is the precipitating electron beams. The authors modeled a scenario in which the cooling plasma moving down from the top of hot granules amplifies the magnetic twist when entering into denser layers, which is similar to our case. However, we see the flare loops become less twisted. Nevertheless, this model suggests that the hydrodynamic effects may be coupled with electrodynamic effects to affect the pre-flare magnetic fields.

By analyzing and modeling the Hα and Hβ data, Hénoux and Karlický, (2013) [76] found that emission lines can be polarized linearly by multiple effects, such as electron beams, return current and filamentary chromospheric evaporation. They found the degree of linear polarizations was about $3 \sim 9\%$. However, in our case, there was no emission detected in the NIR line at 1.56 μm. The NIR line intensity profile remains in absorption during the flare. In addition, the azimuth change, or say the enhanced linear polarization was only found in front of the propagating flare ribbons in our event. Nevertheless, the polarized signal was identified on both sides of the flare ribbons in Hénoux and Karlický, (2013) [76]. Therefore, again we cannot draw a conclusion based on their model.

Alfvén waves [3] also have impacts on the magnetic fields. They are well known in heating the corona [159], accelerating electrons during flares [54] and solar winds [120]. *Alfvén* waves can be generated by magnetic reconnection during flares [13, 54]. In open magnetic field regions, for instance, in solar wind, *Alfvén* waves were found in untwisted field lines both in observations [62] and simulations [112]. For closed field regions, such as the flare loops, Fletcher et al. (2008) [54] presented the large-scale *Alfvén* wave pulses, which accelerate electrons locally. Within non-uniform plasma, *Alfvén* waves appear as torsional waves [170], which can create rotational

perturbations of the plasma and the magnetic fields frozen in the plasma [158]. The perturbations are usually torsional oscillations [119], which should appear periodically but were not observed in our event. However, in the deep atmosphere, these waves can be damped locally by ion-neutral or resistive damping [45], and therefore only the effect of the initial pulse is observed as a transient event. *Alfvén* waves are plausible candidates, but most previous modeling was done for coronal flux tubes, and no quantitative description is available for their effects on photospheric magnetic fields.

In conclusion, the observed field change cannot be explained by existing models. The new, transient magnetic signature in the photosphere that we describe in this paper offers a new diagnostic for future modeling of magnetic reconnection and the resulting energy release. Such observations require high cadence and high resolution. Our results motivate further observations using GST and the Daniel K. Inouye Solar Telescope (DKIST) in probing the mystery of solar flares.

Methods

Magnetic Inversion

After dark and flat field correction, The crosstalk is removed by measuring the effect of optical elements from the telescope to the detector. Pure states of polarization are fed into the light path and their response at the detector tells how the incoming polarization from the Sun would be changed by the optics [43] (and references therein). After careful elimination of the crosstalk among Stokes Q, U, and V, the NIRIS data undergoes Milne-Eddington inversion to fit the Stokes line profiles based on an atmospheric model. The source function with respect to optical depth is simplified to a 1st order polynomial. As results, several key physical parameters can be extracted - B_{tot}, azimuth angle, inclination, Doppler shift, and so forth. For successful fitting into ME-simulated profiles, initial parameters are pre-calculated to be in proximity

to the observed Stokes profiles. This code was specifically designed for BBSO/NIRIS and written by Dr. Jongchul Chae using IDL language.

180° Ambiguity Correction

In order to streamline the analysis of vector magnetogram data, data processing tools have been developed and implemented, including the 180° ambiguity resolution and NLFF coronal magnetic field extrapolation. The 180° azimuthal ambiguity in the transverse magnetograms is resolved using the minimum-energy algorithm that simultaneously minimizes both the electric current density J and the field divergence $|\nabla \cdot \mathbf{B}|$ [123]. Minimizing $|\nabla \cdot \mathbf{B}|$ gives a physically meaningful solution and minimizing J provides a smoothness constraint. A magnetogram is first broken into small sub-areas with which to compute a force-free α parameter. Then a linear force-free field is effectively constructed with which to infer the vertical gradients needed to minimize the divergence. Since the calculation of J and $|\nabla \cdot \mathbf{B}|$ involves derivatives of the magnetic field, the computation is not local, the number of possible solutions is huge and the solution space has many local minima. The simulated-annealing algorithm [96] is used to find the global minimum. This minimum-energy algorithm is the top-performing automated method among present state-of-art algorithms used for resolving the 180° ambiguity [125].

CHAPTER 7

DISSERTATION SUMMARY AND FUTURE WORK

This dissertation focuses on flare energetics, including statistical analysis of energy release in macro-scope and fine structures observed with high resolutions and numerical modeling. Taking the advantages of advanced instrumentation, which provide high spatial, temporal, and spectral resolutions, as well as novel numerical modeling packages, multiple types of emissions were observed and studied. Compact and impulsive WL flare kernels are identified and compared with HXR emission and with SEP events. These statistical comparisons were trying to help in understanding the downward and upward particle acceleration driven by magnetic reconnection, respectively. On the typical flare ribbons, unique features were reported in the leading edges using high-resolution observations. Distinct spectral properties on the well-defined ribbon front are investigated, and state-of-the-art numerical modeling was involved in studying the physical conditions of the heated atmosphere that produces the UV emission and NIR enhanced absorption. Additionally, the magnetic field of the ribbon front was observed using high-resolution magnetograms, and a unique feature was reported. The following two sections summarize the results in two groups, macro-scope energetics, and comparison between observations and modelings.

7.1 WL Flares and the Acceleration of Electrons and SEPs

Free magnetic energies are released via reconnections, which produce a tremendous number of high energy electrons. These electrons travel both downward and upward along with magnetic field lines. The downward group is well known for producing flare heating. One of the controversial issues is that if the upward group is the source of SEP events, which are usually associated with large flares. In studies presented in Chapters 2 and 3, WL emissions in multiple flares were surveyed using images

from SDO/HMI intensity continuum data. Chapter 2 shows a statistical analysis of the correlation between WL and HXR emission. The WL events were identified from SDO/HMI visible continuum and HXR data was obtained from RHESSI. For each event, the contrasted equivalent area (EA) was calculated to define WL emission intensity. Additionally, by fitting HXR data into classic *variable thermal (vth)* plus non-thermal *broken power-law (bpow)* spectrum, the power-law index for each flare peak was retrieved to describe the distribution of high-energy non-thermal electrons. This study confirmed the major role of high energy electrons in producing WL emission. In the second study described in Chapter 3, the WL emission, which here was a good proxy of energetic electrons, was compared with the SEP that was presumed to be accelerated upwards by reconnection. The major results in Chapters 2 and 3 are listed below:

First, the WL emission has an obvious correlation to the HXR spectrum, especially to the high-energy distribution. The EA is inversely proportional to the power-law index of HXR emission, and no strong correlation is found between WL emission and flux of non-thermal electrons at 50 keV. Besides, the group of flares above M5.0 class without detectable WL emission generally have softer HXR spectrums (higher power-law index). *This suggested that direct heating by high-energy non-thermal electrons dominates in powering WL flares.*

Second, time profiles of EA and HXR power-law index were compared, together with the HXR fluxes in energy ranges of 50-100 keV and 100-250 keV. The result confirms that WL and HXR fluxes are temporally correlated during flare evolution.

Third, the 2015-06-22 M6.5 flare was observed using SDO/HMI, GST/BFI. The WL emission was not detected in HMI intensity continuum images but was identified in TiO continuum images with much higher spatial resolution. This suggested that more WL flares would be resolved by using high-resolution observations in solar flares.

Fourth, the WL flare list was compared with the SEP event list to find *no correspondence* between WL flares and SEP events. Moreover, in a small group of SEP events associated with WL flares, no correlation between EA and energetical particle flux was found. Besides, by comparing the temporal evolutions of SEP flux and flares in the closed period, no evidence was found to support that SEPs were accelerated by magnetic reconnection of flares. Reviewing the existing SEP acceleration scenarios, the result favors CME shock waves, or combination of flare and shock waves, over solely the flare.

7.2 The Special Characteristics on Flare Ribbon Front

High-resolution observations carry the ability to resolve the sub-arcsecond structures and allow us to define the flare ribbon front. The frontiers of propagating flare ribbons are believed to represent for the sites of newly heated plasma, which has a different story from the trailing part where electrons were trapped and plasma was heated beforehand. Previous studies have reported noteworthy line features, such as the enhanced absorption in He I 10830 Å line, which is the so-called "negative flare", in ribbon fronts of two flares. Using the data from BBSO/GST and IRIS joint observation, we analyzed the Mg II h&k and Hα lines in the ribbon front of 2015-06-22 M6.5 flare. A combination of RADYN and RH codes was involved to study the line profiles and atmosphere numerically. Then we performed the RADYN simulation in studying the absorption enhancement of He I 10830 Å in the initial phase of the flare. Lastly, using the high-resolution magnetograms, the special signature of the magnetic field in a narrow ribbon front was observed.

First, using IRIS spectrograms, we analyzed the Mg II h&k lines and found the blue-wing broadening in flare ribbon front, before the strong line emission with significant redshift. That is prior to the Hα redshifts. Numerical modeling by RH, using the results from RADYN, suggests that the broadening is caused by spatially

unresolved micro-turbulence, with velocities from 10 to 30 km/s. The enhanced blue wing is likely due to evaporation caused by a decrease in temperature and an increase in electron density, as a consequence of electron precipitation. Strong redshifts are seen in modeled Hα pseudo Doppler diagram, occurring after Mg II blueshift, which agrees with the observations.

Second, we analyzed of numerical models of He I 10830 Å line emission during the flare heating and compared them with BBSO/GST observations of the M-class flare. The observed enhanced absorption is reproduced by the RADYN simulation at the initial stage of the flare. The level of modeled absorption is about 17%, which is comparable to the observed level of 13%. The modeled atmosphere suggested that watershed of emission and absorption in the He I 10830 Å line for the representative run is the condition of T>2 $\times$ 10^4 K and $n_e \geq 4 \times 10^{12} cm^{-3}$, and the special line profiles were mainly contributed by the atmosphere in the height of 1.3-1.5 Mm.

Third, using GST/NIRIS 1.56μm vector magnetogram, a transient rotation of the local magnetic field was observed in the moving ribbon front. Being analyzed carefully, the rotation was confirmed not to be induced artificially, and that was the first observation of such activity. The azimuth angle rotated 12-20 and became closer to the extrapolated potential field, which suggested an untwist of flare loops. The spatiotemporal correlations between the magnetic field variation, conjugate Hα ribbon front, and the distinct spectral lines suggested its relationship with the energetic electron beams, but cannot be well explained using existing models.

Overall, the beneficial from the resolving power of the state-of-art instruments and advanced codes, important constraints were provided in understanding the flare emission and instructive for future observations and developing new modeling

7.3 Future Work

Here I am foreseeing the directions of future research motivated by the work in this dissertation.

Statistical studies of WL flares using high-resolution instruments, such as BBSO/GST and the DKIST, are looked forward to. The comparatively rare WL emissions would be more commonly resolved. Furthermore, the high-resolution images will benefit us in defining the WL flare kernel, which can increase the accuracy in flare models.

The correlation between WL flares and SEPs was not found in work presented in this dissertation, and CME shock wave was suggested to be the main driver of SEPs. However, the SEP acceleration could be a complicated question. Particles in different energy levels may get acceleration from different sites. A comparison of WL flare and SEP events in different characteristics can be performed. E.g., Parker Solar Probe would provide observations of SEPs much closer to the Sun, which may be compared with flares more meaningfully.

Besides the Mg II h&k, there are many lines observed by IRIS. A more comprehensive study, including more lines in the observation, should be able to reveal much more information. Moreover, the RH code is using statistical equilibrium, which means the populations are in equilibrium. This may include inaccuracy in the computation. A more complete synthetic code would improve such numerical study.

Other than the absorption enhancement, there are several noteworthy signatures on the time profile of He I 10830 Å during the atmosphere heating of flare. Extending the modeling to cover a larger time span of evolution should be helpful for understanding the atmosphere's response to the heating. Furthermore, the study about He I 10830 Å presented in this dissertation used the database in F-CHROMA, which provides RADYN output for models within a grid of heating pulsation. This

can result in a discrepancy between the available models and realistic. Performing RADYN simulations for specific flare can improve accuracy.

For the first time that the transient rotation of the vector magnetic field was reported, many possible theories were considered, but no perfect explanation was found. At this time, a new scenario is in need. More high-resolution observations of flare magnetic field are desire, to expand the database of observation of this kind.

Overall, high-resolution observations have proven to be powerful in revealing the physics behind solar flares. Deepening and extending the research using existing data, and performing more high-resolution observations in the future should be helpful in our understanding of the solar flare.

APPENDIX A

SUPPLEMENTARY FIGURES

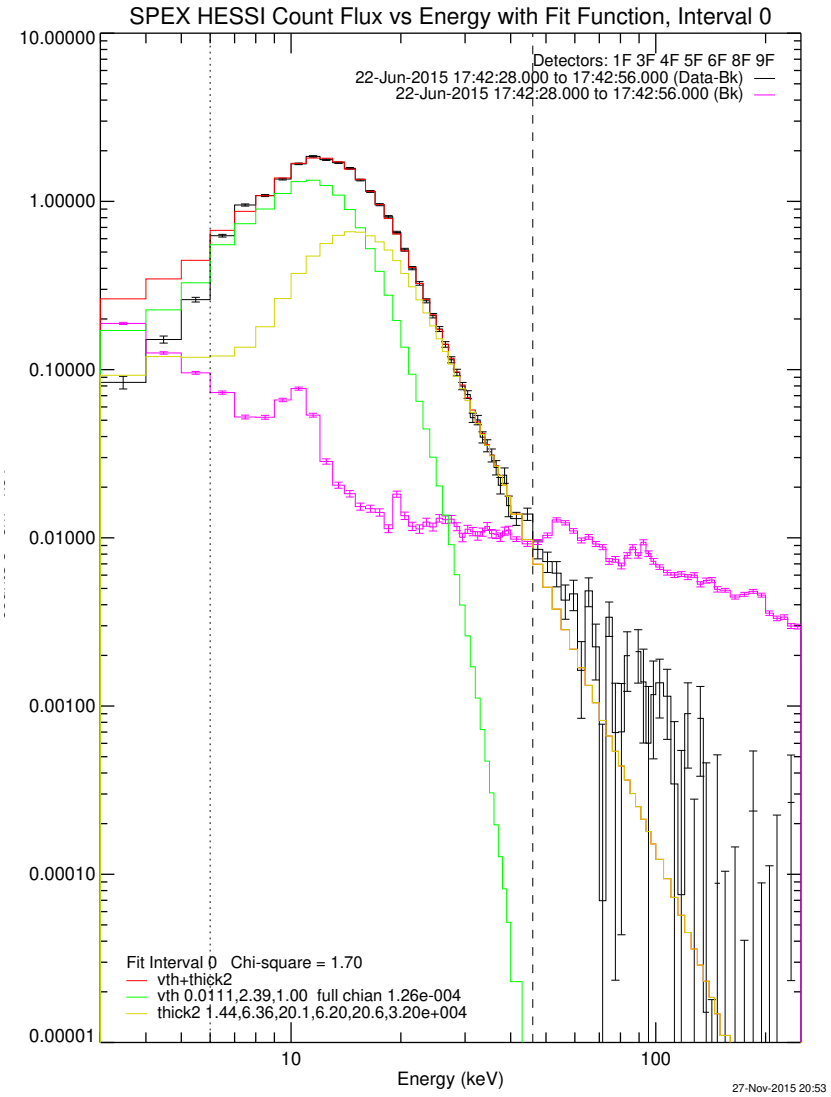

Figure A.1 Fitting of HXR spectrum before the flare peak at 17:42:28 UT, on 2015 Jun 22nd, using two components of Variable Thermal *vth* and Non-thermal *thick2*. The blackcurve is the spectrum data after subtracting the background (pink). The modeledthermal component, non-thermal component, and the overall spectrum are plotted ingreen, yellow, and red, respectively.

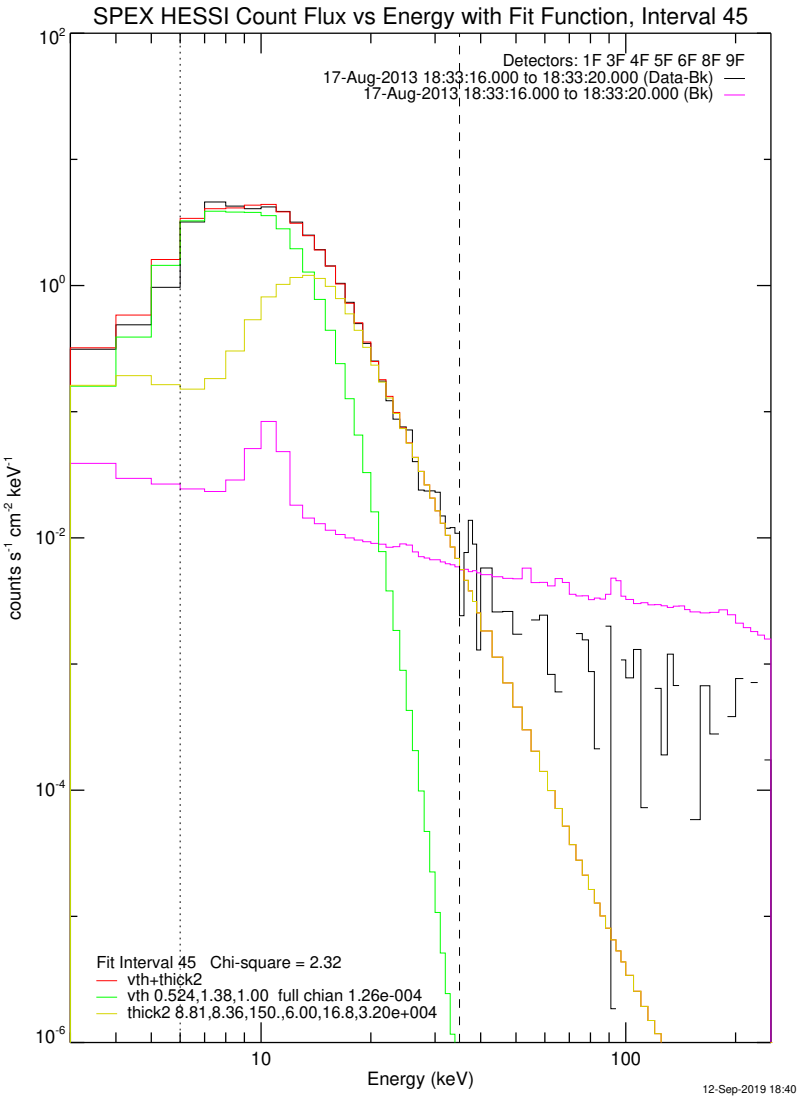

Figure A.2 Fitting of HXR spectrum in 18:33:16 UT–18:33:20 UT 2013-August-17, in the initial phase of the flare. This fitting adopted two components: Variable Thermal *vth* and Non-thermal *thick2*. The blackcurve is the spectrum data after subtracting the background (pink). The modeledthermal component, non-thermal component, and the overall spectrum are plotted ingreen, yellow, and red, respectively.

BIBLIOGRAPHY

[1] Abbett, W. P., and Hawley, S. L. Dynamic Models of Optical Emission in Impulsive Solar Flares. *Astrophysical Journal 521* (1999), 906–919.

[2] Aboudarham, J., and Henoux, J. C. Non-thermal collisional excitation and ionization by electron beams - Effect on the atmospheric energy balance and white-light emission in solar flares. *Advances in Space Research 6* (1986), 131–134.

[3] Alfvén, H. Existence of electromagnetic-hydrodynamic waves. *Nature 150*, 3805 (1942), 405–406.

[4] Alissandrakis, C. E. On the computation of constant alpha force-free magnetic field. *Astronomy and Astrophysics 100*, 1 (1981), 197–200.

[5] Allred, J. C., Hawley, S. L., Abbett, W. P., and Carlsson, M. Radiative Hydrodynamic Models of the Optical and Ultraviolet Emission from Solar Flares. *Astrophysical Journal 630* (2005), 573–586.

[6] Allred, J. C., Kowalski, A. F., and Carlsson, M. A Unified Computational Model for Solar and Stellar Flares. *Astrophysical Journal 809* (2015), 104.

[7] Anan, T., Yoneya, T., Ichimoto, K., UeNo, S., Shiota, D., Nozawa, S., Takasao, S., and Kawate, T. Measurement of vector magnetic field in a flare kernel with a spectropolarimetric observation in He I 10830 Å. *Publications of the ASJ 70*, 6 (2018), 101.

[8] Andretta, V., and Jones, H. P. On the role of the solar corona and transition region in the excitation of the spectrum of neutral helium. *Astrophysical Journal 489*, 1 (1997), 375–394.

[9] Anwar, B., Acton, L. W., Hudson, H. S., Makita, M., McClymont, A. N., and Tsuneta, S. Rapid sunspot motion during a major solar flare. *Solar Physics 147*, 2 (1993), 287–303.

[10] Aschwanden, M. J. GeV particle acceleration in solar flares and ground level enhancement (GLE) events. *Space Science Reviews 171*, 1-4 (2012), 3–21.

[11] Athay, R. G., and Johnson, H. R. The Excitation of he i in the Spectrum. *Astrophysical Journal 131* (1960), 413.

[12] Atwood, W. B., Abdo, A. A., Ackermann, M., Althouse, W., Anderson, B., Axelsson, M., Baldini, L., Ballet, J., Band, D. L., Barbiellini, G., Bartelt, J., Bastieri, D., Baughman, B. M., Bechtol, K., Bédérède, D., Bellardi, F., Bellazzini, R., Berenji, B., Bignami,

G. F., Bisello, D., Bissaldi, E., Blandford, R. D., Bloom, E. D., Bogart, J. R., Bonamente, E., Bonnell, J., Borgland, A. W., Bouvier, A., Bregeon, J., Brez, A., Brigida, M., Bruel, P., Burnett, T. H., Busetto, G., Caliandro, G. A., Cameron, R. A., Caraveo, P. A., Carius, S., Carlson, P., Casandjian, J. M., Cavazzuti, E., Ceccanti, M., Cecchi, C., Charles, E., Chekhtman, A., Cheung, C. C., Chiang, J., Chipaux, R., Cillis, A. N., Ciprini, S., Claus, R., Cohen-Tanugi, J., Condamoor, S., Conrad, J., Corbet, R., Corucci, L., Costamante, L., Cutini, S., Davis, D. S., Decotigny, D., DeKlotz, M., Dermer, C. D., de Angelis, A., Digel, S. W., do Couto e Silva, E., Drell, P. S., Dubois, R., Dumora, D., Edmonds, Y., Fabiani, D., Farnier, C., Favuzzi, C., Flath, D. L., Fleury, P., Focke, W. B., Funk, S., Fusco, P., Gargano, F., Gasparrini, D., Gehrels, N., Gentit, F.-X., Germani, S., Giebels, B., Giglietto, N., Giommi, P., Giordano, F., Glanzman, T., Godfrey, G., Grenier, I. A., Grondin, M.-H., Grove, J. E., Guillemot, L., Guiriec, S., Haller, G., Harding, A. K., Hart, P. A., Hays, E., Healey, S. E., Hirayama, M., Hjalmarsdotter, L., Horn, R., Hughes, R. E., Jóhannesson, G., Johansson, G., Johnson, A. S., Johnson, R. P., Johnson, T. J., Johnson, W. N., Kamae, T., Katagiri, H., Kataoka, J., Kavelaars, A., Kawai, N., Kelly, H., Kerr, M., Klamra, W., Knödlseder, J., Kocian, M. L., Komin, N., Kuehn, F., Kuss, M., Landriu, D., Latronico, L., Lee, B., Lee, S.-H., Lemoine-Goumard, M., Lionetto, A. M., Longo, F., Loparco, F., Lott, B., Lovellette, M. N., Lubrano, P., Madejski, G. M., Makeev, A., Marangelli, B., Massai, M. M., Mazziotta, M. N., McEnery, J. E., Menon, N., Meurer, C., Michelson, P. F., Minuti, M., Mirizzi, N., Mitthumsiri, W., Mizuno, T., Moiseev, A. A., Monte, C., Monzani, M. E., Moretti, E., Morselli, A., Moskalenko, I. V., Murgia, S., Nakamori, T., Nishino, S., Nolan, P. L., Norris, J. P., Nuss, E., Ohno, M., Ohsugi, T., Omodei, N., Orlando, E., Ormes, J. F., Paccagnella, A., Paneque, D., Panetta, J. H., Parent, D., Pearce, M., Pepe, M., Perazzo, A., Pesce-Rollins, M., Picozza, P., Pieri, L., Pinchera, M., Piron, F., Porter, T. A., Poupard, L., Rainò, S., Rando, R., Rapposelli, E., Razzano, M., Reimer, A., Reimer, O., Reposeur, T., Reyes, L. C., Ritz, S., Rochester, L. S., Rodriguez, A. Y., Romani, R. W., Roth, M., Russell, J. J., Ryde, F., Sabatini, S., Sadrozinski, H. F.-W., Sanchez, D., Sander, A., Sapozhnikov, L., Parkinson, P. M. S., Scargle, J. D., Schalk, T. L., Scolieri, G., Sgrò, C., Share, G. H., Shaw, M., Shimokawabe, T., Shrader, C., Sierpowska-Bartosik, A., Siskind, E. J., Smith, D. A., Smith, P. D., Spandre, G., Spinelli, P., Starck, J.-L., Stephens, T. E., Strickman, M. S., Strong, A. W., Suson, D. J., Tajima, H., Takahashi, H., Takahashi, T., Tanaka, T., Tenze, A., Tether,

S., Thayer, J. B., Thayer, J. G., Thompson, D. J., Tibaldo, L., Tibolla, O., Torres, D. F., Tosti, G., Tramacere, A., Turri, M., Usher, T. L., Vilchez, N., Vitale, V., Wang, P., Watters, K., Winer, B. L., Wood, K. S., Ylinen, T., and Ziegler, M. THE LARGE AREA TELESCOPE ON THEFERMI GAMMA-RAY SPACE TELESCOPEMISSION. *Astrophysical Journal 697*, 2 (2009), 1071–1102.

[13] Aulanier, G., Pariat, E., Démoulin, P., and DeVore, C. R. Slip-running reconnection in quasi-separatrix layers. *Solar Physics 238*, 2 (2006), 347–376.

[14] Ayres, T. R., and Linsky, J. L. The MG II h and k lines. II - comparison with synthesized profiles and CA II k. *Astrophysical Journal 205* (1976), 874.

[15] Battaglia, M., and Kontar, E. P. Height structure of X-ray, EUV, and white-light emission in a solar flare. *Astronomy and Astrophysics 533* (2011), L2.

[16] Bombardieri, D. J., Duldig, M. L., Humble, J. E., and Michael, K. J. An improved model for relativistic solar proton acceleration applied to the 2005 january 20 and earlier events. *Astrophysical Journal 682*, 2 (2008), 1315–1327.

[17] Brown, J. The temperature structure of chromospheric flares heated by non-thermal electrons. *Solar Physics 31*, 1 (1973).

[18] Brown, J. C. The Deduction of Energy Spectra of Non-Thermal Electrons in Flares from the Observed Dynamic Spectra of Hard X-Ray Bursts. *Solar Physics 18* (1971), 489–502.

[19] Brown, S. A., Fletcher, L., Kerr, G. S., Labrosse, N., Kowalski, A. F., and De La Cruz Rodríguez, J. Modeling of the Hydrogen Lyman Lines in Solar Flares. *Astrophysical Journal 862* (2018), 59.

[20] Burtseva, O., Martínez-Oliveros, J. C., Petrie, G. J. D., and Pevtsov, A. A. Hard x-ray emission during flares and photospheric field changes. *Astrophysical Journal 806*, 2 (2015), 173.

[21] Canfield, R. C., Penn, M. J., Wulser, J.-P., and Kiplinger, A. L. H-alpha spectra of dynamic chromospheric processes in five well-observed X-ray flares. *Astrophysical Journal 363* (1990), 318–325.

[22] Cao, W., Gorceix, N., Coulter, R., Ahn, K., Rimmele, T. R., and Goode, P. R. Scientific instrumentation for the 1.6 m new solar telescope in big bear. *Astronomische Nachrichten 331*, 6 (2010), 636–639.

[23] Carlsson, M., and Stein, R. F. Non-LTE radiating acoustic shocks and CA II K2V bright points. *Astrophysical Journal 397* (1992), L59–L62.

[24] Carlsson, M., and Stein, R. F. Does a nonmagnetic solar chromosphere exist? *Astrophysical Journal 440* (1995), L29–L32.

[25] Carlsson, M., and Stein, R. F. Formation of solar calcium h and k bright grains. *Astrophysical Journal 481* (1997), 500–514.

[26] Carlsson, M., and Stein, R. F. Dynamic Hydrogen Ionization. *Astrophysical Journal 572* (2002), 626–635.

[27] Carmichael, H. A Process for Flares. *NASA Special Publication 50* (1964), 451.

[28] Carrington, R. C. Description of a Singular Appearance seen in the Sun on September 1, 1859. *Monthly Notices of the RAS 20* (1859), 13–15.

[29] Centeno, R., Trujillo Bueno, J., Uitenbroek, H., and Collados, M. *Influence of Coronal EUV Irradiance on the Stokes Profiles of the He I 10830 Å Multiplet*, vol. 405 of *Astronomical Society of the Pacific Conference Series 405*. (2009), 297.

[30] Charbonneau, P. Dynamo models of the solar cycle. *Living Reviews in Solar Physics 7* (2010), 3.

[31] Cheng, J. X., Ding, M. D., and Carlsson, M. Radiative Hydrodynamic Simulation of the Continuum Emission in Solar White-Light Flares. *Astrophysical Journal 711* (2010), 185–191.

[32] Cheng, J. X., Ding, M. D., and Fang, C. Radiative Hydrodynamic Simulations of He I 10830 Å. *IAU Symposium 294* (2013), 545–546.

[33] Cheng, X., Hao, Q., Ding, M. D., Liu, K., Chen, P. F., Fang, C., and Liu, Y. D. A Two-ribbon White-light Flare Associated with a Failed Solar Eruption Observed by ONSET, SDO, and IRIS. *Astrophysical Journal 809* (2015), 46.

[34] Choudhuri, A. R., Schussler, M., and Dikpati, M. The solar dynamo with meridional circulation. *Astronomy and Astrophysics 303* (1995), L29.

[35] Cox, A. *Allen's astrophysical quantities; 4th ed.* AIP, New York, NY, 2000.

[36] Debi Prasad, C. Near infrared observations of the solar atmosphere. *Bulletin of the Astronomical Society of India 26*, 2 (1998), 253–259.

[37] Delaboudinière, J. P., Artzner, G. E., Brunaud, J., Gabriel, A. H., Hochedez, J. F., Millier, F., Song, X. Y., Au, B., Dere, K. P., Howard, R. A., Kreplin, R., Michels, D. J., Moses, J. D., Defise, J. M., Jamar, C., Rochus, P., Chauvineau, J. P., Marioge, J. P., Catura, R. C., Lemen, J. R., Shing, L., Stern, R. A., Gurman, J. B., Neupert, W. M., Maucherat, A., Clette, F., Cugnon, P., and Dessel, E. L. V. EIT: Extreme-ultraviolet imaging telescope for the SOHO mission. *Solar Physics 162*, 1-2 (1995), 291–312.

[38] Deng, N., Xu, Y., Yang, G., Cao, W., Liu, C., Rimmele, T. R., Wang, H., and Denker, C. Multiwavelength Study of Flow Fields in Flaring Super Active Region NOAA 10486. *Astrophysical Journal 644* (2006), 1278–1291.

[39] Ding, M. D. An unusually intense CA II K line wing: possible role of particle acceleration in the lower atmosphere. *Astronomy and Astrophysics 351* (1999), 368–372.

[40] Ding, M. D. Observations and Spectral Analyses of Solar Flares. *Journal of Korean Astronomical Society 36* (2003), 49–54.

[41] Ding, M. D., Fang, C., and Huang, Y. R. Analysis of 2-d flare spectra: Velocity fields derived from Hα line asymmetries. *Solar Physics 158* (1995), 81–93.

[42] Ding, M. D., Li, H., and Fang, C. On the formation of the He I 10 830 Å line in a flaring atmosphere. *Astronomy and Astrophysics 432* (2005), 699–704.

[43] Elmore, D. F. Polarization calibration of the advanced technology solar telescope. In *Solar Polarization 7* (2014), K. N. Nagendra, J. O. Stenflo, Z. Q. Qu, and M. Sampoorna, Eds., 489 of *Astronomical Society of the Pacific Conference Series*, 279.

[44] Emslie, A. G. The collisional interaction of a beam of charged particles with a hydrogen target of arbitrary ionization level. *Astrophysical Journal 224* (1978), 241–246.

[45] Emslie, A. G., and Machado, M. E. The heating of the temperature minimum region in solar flares - A reassessment. *Solar Physics 64* (1979), 129–134.

[46] Evershed, J. Radial movement in sun-spots ; second paper. *Monthly Notices of the RAS 70* (1910), 217.

[47] Falchi, A., Qiu, J., and Cauzzi, G. Chromospheric evidence for magnetic reconnection. *Astronomy and Astrophysics 328* (1997), 371–380.

[48] Fang, C., and Ding, M. D. On the spectral characteristics and atmospheric models of two types of white-light flares. *Astronomy and Astrophysicss 110* (1995), 99–+.

[49] Fisher, G. H., Bercik, D. J., Welsch, B. T., and Hudson, H. S. Global forces in eruptive solar flares: The lorentz force acting on the solar atmosphere and the solar interior. *Solar Physics 277*, 1 (2012), 59–76.

[50] Fisher, G. H., Canfield, R. C., and McClymont, A. N. Flare Loop Radiative Hydrodynamics - Part Six - Chromospheric Evaporation due to Heating by Nonthermal Electrons. *Astrophysical Journal 289* (1985), 425.

[51] Fleck, B., Deubner, F. L., Maier, D., and Schmidt, W. Observations of Solar Oscillations in He 110830 Angstrom. In *Infrared Solar Physics* (1994), D. M. Rabin, J. T. Jefferies, and C. Lindsey, Eds., 154 of *IAU Symposium*, 65.

[52] Flesch, T. R., and Oliver, J. P. Three-Color Photometry of the Flare Star EV Lacertae. *Astrophysical Journal Letters 189* (1974), L127+.

[53] Fletcher, L., Hannah, I. G., Hudson, H. S., and Metcalf, T. R. A TRACE White Light and RHESSI Hard X-Ray Study of Flare Energetics. *Astrophysical Journal 656* (2007), 1187–1196.

[54] Fletcher, L., and Hudson, H. S. Impulsive Phase Flare Energy Transport by Large-Scale Alfvén Waves and the Electron Acceleration Problem. *Astrophysical Journal 675* (2008), 1645–1655.

[55] Garcia, H. A. Temperature and emission measure from goes soft x-ray measurements. *Solar Physics 154*, 2 (1994), 275–308.

[56] Gary, D. E., Hurford, G. J., Nita, G. M., White, S. M., McTiernan, J., and Fleishman, G. D. The expanded owens valley solar array (eovsa). In *American Astronomical Society Meeting Abstracts #224* (2014), 224 of *American Astronomical Society Meeting Abstracts*,123.60.

[57] Gary, G. A. Linear force-free magnetic fields for solar extrapolation and interpretation. *Astrophysical Journal Supplements 69* (1989), 323.

[58] Goldberg, L. The Temperature of the Solar Chromosphere. *Astrophysical Journal 89* (1939), 673.

[59] Golub, L., DeLuca, E., Austin, G., Bookbinder, J., Caldwell, D., Cheimets, P., Cirtain, J., Cosmo, M., Reid, P., Sette, A., Weber, M., Sakao, T., Kano, R., Shibasaki, K., Hara, H., Tsuneta, S., Kumagai, K., Tamura, T., Shimojo, M., McCracken, J., Carpenter, J., Haight, H., Siler, R., Wright, E., Tucker, J., Rutledge, H., Barbera, M., Peres, G., and Varisco, S. The x-ray telescope (XRT) for the hinode mission. *Solar Physics 243*, 1 (2007), 63–86.

[60] Goode, P. R., and Cao, W. The 1.6 m Off-Axis New Solar Telescope (NST) in Big Bear. In *Second ATST-EAST Meeting: Magnetic Fields from the Photosphere to the Corona.* (2012), T. R. Rimmele, A. Tritschler, F. Wöger, M. Collados Vera, H. Socas-Navarro, R. Schlichenmaier, M. Carlsson, T. Berger, A. Cadavid, P. R. Gilbert, P. R. Goode, and M. Knölker, Eds., 463 of *Astronomical Society of the Pacific Conference Series*, 357.

[61] Goode, P. R., and Cao, W. The 1.6 m Off-Axis New Solar Telescope (NST) in Big Bear. In *Second ATST-EAST Meeting: Magnetic Fields from the Photosphere to the Corona.* (2012), T. R. Rimmele, A. Tritschler, F. Wöger, M. Collados Vera, H. Socas-Navarro, R. Schlichenmaier, M. Carlsson, T. Berger, A. Cadavid, P. R. Gilbert, P. R. Goode, and M. Knölker, Eds., 463 of *Astronomical Society of the Pacific Conference Series*, 357.

[62] Gosling, J. T., Skoug, R. M., McComas, D. J., and Smith, C. W. Direct evidence for magnetic reconnection in the solar wind near 1 au. *Journal of Geophysical Research (Space Physics) 110*, A1 (2005), A01107.

[63] Graham, D. R., and Cauzzi, G. Temporal Evolution of Multiple Evaporating Ribbon Sources in a Solar Flare. *Astrophysical Journal Letters 807* (2015), L22.

[64] Graham, D. R., Fletcher, L., and Hannah, I. G. Hinode/EIS plasma diagnostics in the flaring solar chromosphere. *Astronomy and Astrophysics 532* (2011), A27.

[65] Gray, L. J., Beer, J., Geller, M., Haigh, J. D., Lockwood, M., Matthes, K., Cubasch, U., Fleitmann, D., Harrison, G., Hood, L., Luterbacher, J., Meehl, G. A., Shindell, D., van Geel, B., and White, W. SOLAR INFLUENCES ON CLIMATE. *Reviews of Geophysics 48*, 4 (2010).

[66] Haigh, J. D. The sun and the earths climate. *Living Reviews in Solar Physics 4* (2007).

[67] Handy, B. N., Acton, L. W., Kankelborg, C. C., Wolfson, C. J., Akin, D. J., Bruner, M. E., Caravalho, R., Catura, R. C., Chevalier, R., Duncan, D. W., Edwards, C. G., Feinstein, C. N., Freeland, S. L., Friedlaender, F. M., Hoffmann, C. H., Hurlburt, N. E., Jurcevich, B. K., Katz, N. L., Kelly, G. A., Lemen, J. R., Levay, M., Lindgren, R. W., Mathur, D. P., Meyer, S. B., Morrison, S. J., Morrison, M. D., Nightingale, R. W., Pope, T. P., Rehse, R. A., Schrijver, C. J., Shine, R. A., Shing, L., Strong, K. T., Tarbell, T. D., Title, A. M., Torgerson, D. D., Golub, L., Bookbinder, J. A., Caldwell, D., Cheimets, P. N., Davis, W. N., Deluca, E. E., McMullen, R. A., Warren, H. P., Amato, D., Fisher, R., Maldonado, H., and Parkinson, C. The transition region and coronal explorer. *Solar Physics 187* (1999), 229–260.

[68] Hao, Q., Guo, Y., Dai, Y., Ding, M. D., Li, Z., Zhang, X. Y., and Fang, C. Understanding the white-light flare on 2012 March 9: evidence of a two-step magnetic reconnection. *Astronomy and Astrophysics 544* (2012), L17.

[69] Harrison, R. A., Sawyer, E. C., Carter, M. K., Cruise, A. M., Cutler, R. M., Fludra, A., Hayes, R. W., Kent, B. J., Lang, J., Parker, D. J., Payne, J., Pike, C. D., Peskett, S. C., Richards, A. G., Gulhane, J. L., Norman, K., Breeveld, A. A., Breeveld, E. R., Al Janabi, K. F., McCalden, A. J., Parkinson, J. H., Self, D. G., Thomas, P. D., Poland, A. I., Thomas, R. J., Thompson, W. T., Kjeldseth-Moe, O., Brekke, P., Karud, J., Maltby, P., Aschenbach, B., Bräuninger, H., Kühne, M., Hollandt, J., Siegmund, O. H. W., Huber, M. C. E., Gabriel, A. H., Mason, H. E., and Bromage, B. J. I. The Coronal Diagnostic Spectrometer for the Solar and Heliospheric Observatory. *Solar Physics 162* (1995), 233–290.

[70] Harvey, J., and Hall, D. Magnetic Fields Measured with the 10830 Å Hei Line. In *Solar Magnetic Fields* (1971), R. Howard, Ed., 43 of *IAU Symposium*, 279.

[71] Harvey, K. L., and Recely, F. He I 10830 observations of the 3N/M4.0 flare of 4 September, 1982. *Solar Physics 91* (1984), 127–139.

[72] Harvey, K. L., and Recely, F. Polar Coronal Holes During Cycles 22 and 23. *Solar Physics 211*, 1 (2002), 31–52.

[73] Henoux, C., and Nakagawa, Y. Chromospheric response to soft X-ray radiation in flares. *Astronomy and Astrophysics 57* (1977), 105–110.

[74] Henoux, J., Aboudarham, J., Brown, J. C., van den Oord, G. H. J., and van Driel-Gesztelyi, L. Black and white flares? *Astronomy and Astrophysics 233* (1990), 577–582.

[75] Henoux, J., and Nakagawa, Y. Dynamics of an atmosphere irradiated by soft x-rays in flares. *Astronomy and Astrophysics 66*, 3 (1978), 385–393.

[76] Hénoux, J. C., and Karlický, M. Flare line impact polarization. na d2 589 nm line polarization in the 2001 june 15 flare. *Astronomy and Astrophysics 556* (2013), A95.

[77] Hirayama, T. Modern observations of solar prominences. *Solar Physics 100* (1985), 415–434.

[78] Huang, N., Sadykov, V. M., Xu, Y., Jing, J., and Wang, H. Comparison of enhanced absorption in he i 10830 Å in observations and modeling during the early phase of a solar flare. *Astrophysical Journal Letters 897* (2020), L6.

[79] Huang, N., Xu, Y., Sadykov, V. M., Jing, J., and Wang, H. Spectral diagnosis of mg ii and hlines during the initial stage of an m6.5 solar flare. *Astrophysical Journal Letters 878* (2019), L15.

[80] Huang, N., Xu, Y., and Wang, H. Relationship between intensity of white-light flares and proton flux of solar energetic particles. *Research Notes of the AAS 2* (2018), 7.

[81] Huang, N.-Y., Xu, Y., and Wang, H. The Energetics of White-light Flares Observed by SDO/HMI and RHESSI. *Research in Astronomy and Astrophysics 16* (2016), 177.

[82] Hudson, H. S. Thick-Target Processes and White-Light Flares. *Solar Physics 24* (1972), 414–428.

[83] Hudson, H. S. Chasing white-light flares. *Solar Physics 291*, 5 (2016), 1273–1322.

[84] Hudson, H. S., Acton, L. W., Hirayama, T., and Uchida, Y. White-light flares observed by YOHKOH. *Publications of the ASJ 44* (1992), L77–L81.

[85] Hudson, H. S., Fisher, G. H., and Welsch, B. T. Flare Energy and Magnetic Field Variations. In *Subsurface and Atmospheric Influences on Solar Activity* (2008), R. Howe, R. W. Komm, K. S. Balasubramaniam, and G. J. D. Petrie, Eds., 383 of *Astronomical Society of the Pacific Conference Series*, 221.

[86] Hudson, H. S., Wolfson, C. J., and Metcalf, T. R. White-Light Flares: A TRACE/RHESSI Overview. *Solar Physics 234* (2006), 79–93.

[87] Hurford, G. J., Read, R. B., and Zirin, H. A frequency-agile interferometer for solar microwave spectroscopy. *Solar Physics 94* (1984), 413–426.

[88] ichi Mori, K., ichi Sakai, J., and Zhao, J. Proton acceleration near an x-type magnetic reconnection region. *Astrophysical Journal 494* (1998), 430–437.

[89] Isobe, H., Kubo, M., Minoshima, T., Ichimoto, K., Katsukawa, Y., Tarbell, T. D., Tsuneta, S., Berger, T. E., Lites, B., Nagata, S., Shimizu, T., Shine, R. A., Suematsu, Y., and Title, A. M. Flare Ribbons Observed with G-band and FeI 6302Å, Filters of the Solar Optical Telescope on Board Hinode. *Publications of the ASJ 59* (2007), 807–813.

[90] Jess, D. B., Mathioudakis, M., Crockett, P. J., and Keenan, F. P. Do All Flares Have White-Light Emission? *Astrophysical Journal Letters 688* (2008), L119–L122.

[91] Jing, J., Liu, R., Cheung, M. C. M., Lee, J., Xu, Y., Liu, C., Zhu, C., and Wang, H. Witnessing a large-scale slipping magnetic reconnection along a dimming channel during a solar flare. *Astrophysical Journal Letters 842* (2017), L18.

[92] Jing, J., Xu, Y., Cao, W., Liu, C., Gary, D., and Wang, H. Unprecedented fine structure of a solar flare revealed by the 1.6 m new solar telescope. *Scientific Reports 6* (2016), 24319.

[93] Kane, S. R. Impulsive (flash) Phase of Solar Flares: Hard X-Ray Microwave, EUV and Optical Observations. In *Coronal Disturbances* (1974), G. A. Newkirk, Ed.,57 of *IAU Symposium*, 105.

[94] Kerr, G. S., Fletcher, L., Russell, A. e. J. B., and Allred, J. C. Simulations of the Mg II k and Ca II 8542 lines from an AlfvÉn Wave-heated Flare Chromosphere. *Astrophysical Journal 827* (2016), 101.

[95] Kirchhoff, G. *Ueber die Fraunhofer'schen Linien*. 1859.

[96] Kirkpatrick, S., Gelatt, C. D., and Vecchi, M. P. Optimization by simulated annealing. *Science 220*, 4598 (1983), 671–680.

[97] Klein, K.-L., and Trottet, G. The origin of solar energetic particle events: Coronal acceleration versus shock wave acceleration. *Space Science Reviews 95* (2001), 215–225.

[98] Kopp, R. A., and Pneuman, G. W. Magnetic reconnection in the corona and the loop prominence phenomenon. *Solar Physics 50* (1976), 85–98.

[99] Koshiishi, H., Enome, S., Nakajima, H., Shibasaki, K., Nishio, M., Takano, T., Hanaoka, Y., Torii, C., Sekiguchi, H., Kawashima, S., Bushimata, T., Shinohara, N., Irimajiri, Y., and Shiomi, Y. Evaluation of the imaging performance of the nobeyama radioheliograph. *Publications of the ASJ 46* (1994), L33–L36.

[100] Kosovichev, A. G. Tomographic imaging of the suns interior. *Astrophysical Journal 461* (1996), L55–L57.

[101] Kosovichev, A. G. Helioseismic Response to the X2.2 Solar Flare of 2011 February 15. *Astrophysical Journal Letters 734* (2011), L15.

[102] Kuhar, M., Krucker, S., Martínez Oliveros, J. C., Battaglia, M., Kleint, L., Casadei, D., and Hudson, H. S. Correlation of Hard X-Ray and White Light Emission in Solar Flares. *Astrophysical Journal 816* (2016), 6.

[103] Kuridze, D., Mathioudakis, M., Simões, P. J. A., Rouppe van der Voort, L., Carlsson, M., Jafarzadeh, S., Allred, J. C., Kowalski, A. F., Kennedy, M., Fletcher, L., Graham, D., and Keenan, F. P. Hα Line Profile Asymmetries and the Chromospheric Flare Velocity Field. *Astrophysical Journal 813* (2015), 125.

[104] Landman, D. A. A study of the He λ 10830 line emission from quiescent prominences. *Solar Physics 50*, 2 (1976), 383–394.

[105] Leenaarts, J., Carlsson, M., and van der Voort, L. R. THE FORMATION OF THE h LINE IN THE SOLAR CHROMOSPHERE. *Astrophysical Journal 749*, 2 (2012), 136.

[106] Leenaarts, J., Pereira, T. M. D., Carlsson, M., Uitenbroek, H., and De Pontieu, B. The Formation of IRIS Diagnostics. II. The Formation of the Mg II hk Lines in the Solar Atmosphere. *Astrophysical Journal 772* (2013), 90.

[107] Leenaarts, J., Pereira, T. M. D., Carlsson, M., Uitenbroek, H., and Pontieu, B. D. THE FORMATION OFIRISDIAGNOSTICS. i. a QUINTESSENTIAL MODEL ATOM OF mg II AND GENERAL FORMATION PROPERTIES OF THE mg II h&k LINES. *Astrophysical Journal 772* (2013), 89.

[108] Libbrecht, T., de la Cruz Rodríguez, J., Danilovic, S., Leenaarts, J., and Pazira, H. Chromospheric condensations and magnetic field in a C3.6-class flare studied via He I D_3 spectro-polarimetry. *Astronomy and Astrophysics 621* (2019), A35.

[109] Lin, H., Penn, M. J., and Kuhn, J. R. He i 10830 Angstrom Line Polarimetry: A New Tool to Probe the Filament Magnetic Fields. *Astrophysical Journal 493* (1998), 978–995.

[110] Lin, J., and Forbes, T. G. Effects of reconnection on the coronal mass ejection process. *Journal of Geophysics Research 105* (2000), 2375–2392.

[111] Lin, R. P., Dennis, B. R., Hurford, G. J., Smith, D. M., Zehnder, A., Harvey, P. R., Curtis, D. W., Pankow, D., Turin, P., Bester, M., Csillaghy, A., Lewis, M., Madden, N., van Beek, H. F., Appleby, M., Raudorf, T., McTiernan, J., Ramaty, R., Schmahl, E., Schwartz, R., Krucker, S., Abiad, R., Quinn, T., Berg, P., Hashii, M., Sterling, R., Jackson, R., Pratt, R., Campbell, R. D., Malone, D., Landis, D., Barrington-Leigh, C. P., Slassi-Sennou, S., Cork, C., Clark, D., Amato, D., Orwig, L., Boyle, R., Banks, I. S., Shirey, K., Tolbert, A. K., Zarro, D., Snow, F., Thomsen, K., Henneck, R., McHedlishvili, A., Ming, P., Fivian, M., Jordan, J., Wanner, R., Crubb, J., Preble, J., Matranga, M., Benz, A., Hudson, H., Canfield, R. C., Holman, G. D., Crannell, C., Kosugi, T., Emslie, A. G., Vilmer, N., Brown, J. C., Johns-Krull, C., Aschwanden, M., Metcalf, T., and Conway, A. The Reuven Ramaty High-Energy Solar Spectroscopic Imager (RHESSI). *Solar Physics 210* (2002), 3–32.

[112] Linton, M. G., and Longcope, D. W. A model for patchy reconnection in three dimensions. *Astrophysical Journal 642* (2006), 1177–1192.

[113] Liu, C., Deng, N., Liu, R., Lee, J., Wiegelmann, T., Jing, J., Xu, Y., Wang, S., and Wang, H. Rapid Changes of Photospheric Magnetic Field after Tether-cutting Reconnection and Magnetic Implosion. *Astrophysical Journall 745* (2012), L4.

[114] Liu, C., Xu, Y., Cao, W., Deng, N., Lee, J., Hudson, H. S., Gary, D. E., Wang, J., Jing, J., and Wang, H. Flare differentially rotates sunspot on sun's surface. *Nature Communications 7* (2016), 13104.

[115] Lyot, B. Un monochromateur à grand champ utilisant les interferences en lumière polarisée. *Compt. Rend.Acad Sci. 197* (1933), 1593.

[116] Machado, M. E., Avrett, E. H., Vernazza, J. E., and Noyes, R. W. Semiempirical models of chromospheric flare regions. *Astrophysical Journal 242* (1980), 336.

[117] Machado, M. E., Emslie, A. G., and Avrett, E. H. Radiative backwarming in white-light flares. *Solar Physics 124* (1989), 303–317.

[118] Martínez Oliveros, J.-C., Hudson, H. S., Hurford, G. J., Krucker, S., Lin, R. P., Lindsey, C., Couvidat, S., Schou, J., and Thompson, W. T. The Height of a White-light Flare and Its Hard X-Ray Sources. *Astrophysical Journal Letters 753* (2012), L26.

[119] Mathioudakis, M., Jess, D. B., and Erdélyi, R. Alfvén waves in the solar atmosphere. from theory to observations. *Space Science Reviews 175* (2013), 1–27.

[120] Matsumoto, T., and Suzuki, T. K. Connecting the sun and the solar wind: The first 2.5-dimensional self-consistent mhd simulation under the alfvén wave scenario. *Astrophysical Journal 749* (2012), 8.

[121] Matthews, S. A., van Driel-Gesztelyi, L., Hudson, H. S., and Nitta, N. V. A catalogue of white-light flares observed by Yohkoh. *Astronomy and Astrophysics 409* (2003), 1107–1125.

[122] Maurya, R. A., Vemareddy, P., and Ambastha, A. Velocity and magnetic transients driven by the x2.2 white-light flare of 2011 february 15 in noaa 11158. *Astrophysical Journal 747* (2012), 134.

[123] Metcalf, T. R. Resolving the 180-degree ambiguity in vector magnetic field measurements: The 'minimum' energy solution. *Solar Physics 155* (1994), 235–242.

[124] Metcalf, T. R., Canfield, R. C., and Saba, J. L. R. Flare heating and ionization of the low solar chromosphere. II - Observations of five solar flares. *Astrophysical Journal 365* (1990), 391–406.

[125] Metcalf, T. R., Leka, K. D., Barnes, G., Lites, B. W., Georgoulis, M. K., Pevtsov, A. A., Balasubramaniam, K. S., Gary, G. A., Jing, J., Li, J., Liu, Y., Wang, H. N., Abramenko, V., Yurchyshyn, V., and Moon, Y. J. An overview of existing algorithms for resolving the 180 ambiguity in vector magnetic fields: Quantitative tests with synthetic data. *Solar Physics 237*, 2 (2006), 267–296.

[126] Milkey, R. W., Heasley, J. N., and Beebe, H. A. Helium Excitation in the Solar Chromosphere: he i in a Homogeneous Chromosphere. *Astrophysical Journal 186* (1973), 1043–1052.

[127] Milkey, R. W., and Mihalas, D. Resonance-line transfer with partial redistribution. II - the solar MG II lines. *Astrophysical Journal 192* (1974), 769.

[128] Milligan, R. O. Extreme Ultra-Violet Spectroscopy of the Lower Solar Atmosphere During Solar Flares (Invited Review). *Solar Physics 290* (2015), 3399–3423.

[129] Mohler, O. C., and Goldberg, L. The Width of the Infrared Helium Line in the Solar Spectrum. *Astrophysical Journal 124* (1956), 13.

[130] Muglach, K., and Schmidt, W. Height and dynamics of the quiet solar chromosphere at the limb. *Astronomy and Astrophysics 379* (2001), 592–600.

[131] Najita, K., and Orrall, F. Q. White Light Events as Photospheric Flares. *Solar Physics 15* (1970), 176–194.

[132] Nancay. The mark IV nan?ay radioheliograph. *Solar Physics 120*, 1 (1989), 193–204.

[133] Neidig, D. F. The importance of solar white-light flares. *Solar Physics 121* (1989), 261–269.

[134] Neidig, D. F., and Cliver, E. W. A catalog of solar white-light flares, including their statistical properties and associated emissions, 1859 - 1982. *NASA STI/Recon Technical Report N 84* (1983), 24521.

[135] Neidig, D. F., Kiplinger, A. L., Cohl, H. S., and Wiborg, P. H. The solar white-light flare of 1989 March 7 - Simultaneous multiwavelength observations at high time resolution. *Astrophysical Journal 406* (1993), 306–318.

[136] Neidig, D. F., Wiborg, P. H., and Gilliam, L. B. Physical properties of white-light flares derived from their center-to-limb distribution. *Solar Physics 144* (1993), 169–194.

[137] Ogawara, Y., Takano, T., Kato, T., Kosugi, T., Tsuneta, S., Watanabe, T., Kondo, I., and Uchida, Y. The SOLAR-a mission: An overview. *Solar Physics 136* (1991), 1–16.

[138] Panos, B., Kleint, L., Huwyler, C., Krucker, S., Melchior, M., Ullmann, D., and Voloshynovskiy, S. Identifying typical mg ii flare spectra using machine learning. *Astrophysical Journal 861* (2018), 62.

[139] Parker, E. N. Hydromagnetic dynamo models. *Astrophysical Journal 122* (1955), 293.

[140] Patterson, A., and Zirin, H. Transient magnetic field changes in flares. *Astrophysical Journal Letters 243* (1981), L99–L101.

[141] Penn, M. J. NAC Observations of an X1.8 Flare. In *AAS/Solar Physics Division Meeting #37* (2006), AAS/Solar Physics Division Meeting, 8.11.

[142] Penn, M. J., and Kuhn, J. R. Imaging Spectropolarimetry of the He i 1083 Nanometer Line in a Flaring Solar Active Region. *Astrophysical Journal Letters 441* (1995), L51.

[143] Pesnell, W. D., Thompson, B. J., and Chamberlin, P. C. The Solar Dynamics Observatory (SDO). *Solar Physics 275* (2012), 3–15.

[144] Pontieu, B. D., Title, A. M., Lemen, J. R., Kushner, G. D., Akin, D. J., Allard, B., Berger, T., Boerner, P., Cheung, M., Chou, C., Drake, J. F., Duncan, D. W., Freeland, S., Heyman, G. F., Hoffman, C., Hurlburt, N. E., Lindgren, R. W., Mathur, D., Rehse, R., Sabolish, D., Seguin, R., Schrijver, C. J., Tarbell, T. D., Wülser, J.-P., Wolfson, C. J., Yanari, C., Mudge, J., Nguyen-Phuc, N., Timmons, R., van Bezooijen, R., Weingrod, I., Brookner, R., Butcher, G., Dougherty, B., Eder, J., Knagenhjelm, V., Larsen, S., Mansir, D., Phan, L., Boyle, P., Cheimets, P. N., DeLuca, E. E., Golub, L., Gates, R., Hertz, E., McKillop, S., Park, S., Perry, T., Podgorski, W. A., Reeves, K., Saar, S., Testa, P., Tian, H., Weber, M., Dunn, C., Eccles, S., Jaeggli, S. A., Kankelborg, C. C., Mashburn, K., Pust, N., Springer, L., Carvalho, R., Kleint, L., Marmie, J., Mazmanian, E., Pereira, T. M. D., Sawyer, S., Strong, J., Worden, S. P., Carlsson, M., Hansteen, V. H., Leenaarts, J., Wiesmann, M., Aloise, J., Chu, K.-C., Bush, R. I., Scherrer, P. H., Brekke, P., Martinez-Sykora, J., Lites, B. W., McIntosh, S. W., Uitenbroek, H., Okamoto, T. J., Gummin, M. A., Auker, G., Jerram, P., Pool, P., and Waltham, N. The interface region imaging spectrograph (IRIS). *Solar Physics 289* (2014), 2733–2779.

[145] Pulkkinen, T. Space weather: Terrestrial perspective. *Living Reviews in Solar Physics 4* (2007).

[146] Qiu, J., and Gary, D. E. Flare-related Magnetic Anomaly with a Sign Reversal. *Astrophysical Journal 599* (2003), 615–625.

[147] Reames, D. Solar energetic particles: Is there time to hide? *Radiation Measurements 30* (1999), 297–308.

[148] Roussev, I. I., Sokolov, I. V., Forbes, T. G., Gombosi, T. I., Lee, M. A., and Sakai, J. I. A numerical model of a coronal mass ejection: Shock development with implications for the acceleration of GeV protons. *Astrophysical Journal 605*, 1 (2004), L73–L76.

[149] Rubio da Costa, F., and Kleint, L. A parameter study for modeling mg ii h and k emission during solar flares. *Astrophysical Journal 842*, 2 (2017), 82.

[150] Rubio da Costa, F., Kleint, L., Petrosian, V., Liu, W., and Allred, J. C. Data-driven Radiative Hydrodynamic Modeling of the 2014 March 29 X1.0 Solar Flare. *Astrophysical Journal 827* (2016), 1.

[151] Rueedi, I., Solanki, S. K., and Livingston, W. C. Infrared lines as probes of solar magnetic features. X. HeI 10830A as a diagnostic of chromospheric magnetic fields. *Astronomy and Astrophysics 293* (1995), 252–262.

[152] Rust, D. M., and Hegwer, F. Analysis of the August 7, 1972 white light flare - Light curves and correlation with hard X-rays. *Solar Physics 40* (1975), 141–157.

[153] Schmidt, W., Knoelker, M., and Westendorp Plaza, C. Limb observations of the HeI 1083.0 NM line. *Astronomy and Astrophysics 287* (1994), 229–232.

[154] Schou, J., Scherrer, P. H., Bush, R. I., Wachter, R., Couvidat, S., Rabello-Soares, M. C., Bogart, R. S., Hoeksema, J. T., Liu, Y., Duvall, T. L., Akin, D. J., Allard, B. A., Miles, J. W., Rairden, R., Shine, R. A., Tarbell, T. D., Title, A. M., Wolfson, C. J., Elmore, D. F., Norton, A. A., and Tomczyk, S. Design and Ground Calibration of the Helioseismic and Magnetic Imager (HMI) Instrument on the Solar Dynamics Observatory (SDO). *Solar Physics 275* (2012), 229–259.

[155] Schwabe, H., and Schwabe, H. Sonnen — beobachtungen im jahre 1843. *Astronomische Nachrichten 21* (1844), 234–235.

[156] Schwartz, R., Csillaghy, A., Tolbert, A., Hurford, G., MTiernan, J., and Zarro, D. *Solar Physics 210* (2002), 165–191.

[157] Sharykin, I. N., and Kosovichev, A. G. Fine structure of flare ribbons and evolution of electric currents. *Astrophysical Journal Letters 788* (2014), L18.

[158] Shestov, S. V., Nakariakov, V. M., Ulyanov, A. S., Reva, A. A., and Kuzin, S. V. Nonlinear evolution of short-wavelength torsional alfvén waves. *Astrophysical Journal 840* (2017), 64.

[159] Srivastava, A. K., Shetye, J., Murawski, K., Doyle, J. G., Stangalini, M., Scullion, E., Ray, T., Wójcik, D. P., and Dwivedi, B. N. High-frequency torsional alfvén waves as an energy source for coronal heating. *Scientific Reports 7* (2017), 43147.

[160] Steenbeck, M., and Krause, F. Erklärung stellarer und planetarer magnetfelder durch einen turbulenzbedingten dynamomechanismus. *Zeitschrift für Naturforschung A 21* (1966). 8.

[161] Sturrock, P. A. Model of the High-Energy Phase of Solar Flares. *Nature 211* (1966), 695–697.

[162] Sukhorukov, A. V., and Leenaarts, J. Partial redistribution in 3D non-LTE radiative transfer in solar-atmosphere models. *Astronomy and Astrophysics 597* (2017), A46.

[163] Tan, C., Chen, P. F., Abramenko, V., and Wang, H. Evolution of optical penumbral and shear flows associated with the x3.4 flare of 2006 december 13. *Astrophysical Journal 690* (2009), 1820–1828.

[164] Tandberg-Hanssen, E. Études des raies d'émission de He I dans l'atmosphère solaire. Les profils de la raie triplet infrarouge 10830 Å. *Annales d'Astrophysique 25* (1962), 357.

[165] Taroyan, Y., and Williams, T. Magnetic field twisting by intergranular downdrafts. *Astrophysical Journal 829* (2016), 107.

[166] Tei, A., Sakaue, T., Okamoto, T. J., Kawate, T., Heinzel, P., UeNo, S., Asai, A., Ichimoto, K., and Shibata, K. Blue-wing enhancement of the chromospheric Mg II h and k lines in a solar flare. *Publications of the ASJ* (2018).

[167] Tian, H., DeLuca, E. E., Cranmer, S. R., De Pontieu, B., Peter, H., Martínez-Sykora, J., Golub, L., McKillop, S., Reeves, K. K., Miralles, M. P., McCauley, P., Saar, S., Testa, P., Weber, M., Murphy, N., Lemen, J., Title, A., Boerner, P., Hurlburt, N., Tarbell, T. D., Wuelser, J. P., Kleint, L., Kankelborg, C., Jaeggli, S., Carlsson, M., Hansteen, V., and McIntosh, S. W. Prevalence of small-scale jets from the networks of the solar transition region and chromosphere. *Science 346* (2014), 6207.

[168] Uitenbroek, H. Multilevel Radiative Transfer with Partial Frequency Redistribution. *Astrophysical Journal 557* (2001), 389–398.

[169] Usoskin, I. G. A history of solar activity over millennia. *Living Reviews in Solar Physics 14* (2017).

[170] Van Doorsselaere, T., Nakariakov, V. M., and Verwichte, E. Detection of waves in the solar corona: Kink or alfvén? *Astrophysical Journal Letters 676* (2008), L73.

[171] Vernazza, J. E., Avrett, E. H., and Loeser, R. Structure of the solar chromosphere. iii. models of the euv brightness components of the quiet sun. *Astrophysical Journal Supplement 45* (1981), 635–725.

[172] Wang, H., Chae, J., Gurman, J. B., and Kucera, T. A. Comparison of Prominences in Hα and He II 304 Å. *Solar Physics 183* (1998), 91–96.

[173] Wang, H., Jing, J., Tan, C., Wiegelmann, T., and Kubo, M. Study of Magnetic Channel Structure in Active Region 10930. *Astrophysical Journal 687* (2008), 658–667.

[174] Wang, H., Liu, C., Ahn, K., Xu, Y., Jing, J., Deng, N., Huang, N., Liu, R., Kusano, K., Fleishman, G. D., Gary, D. E., and Cao, W. High-resolution observations of flare precursors in the low solar atmosphere. *Nature Astronomy 1* (2017), 0085.

[175] Wang, H., Liu, C., Qiu, J., Deng, N., Goode, P. R., and Denker, C. Rapid penumbral decay following three x-class solar flares. *Astrophysical Journal Letters 601* (2004), L195–L198.

[176] Wang, H., and Qiu, J. Relationship between Flare Kernels in Hα Far-Blue Wing and Magnetic Fields. *Astrophysical Journal 568* (2002), 408–412.

[177] Wang, L., Fang, C., and Ming-DeDing. Small-Scale Brightenings in the UV Continuum of an M9.1 Solar Flare. *Chinese Journal of Astronomy and Astrophysics 7* (2007), 721–732.

[178] Wang, S., Liu, C., Deng, N., and Wang, H. Sudden photospheric motion and sunspot rotation associated with the x2.2 flare on 2011 february 15. *Astrophysical Journal Letters 782* (2014), L31.

[179] Wang, S., Liu, C., Liu, R., Deng, N., Liu, Y., and Wang, H. Response of the photospheric magnetic field to the x2.2 flare on 2011 february 15. *Astrophysical Journal Letters 745*, 2 (2012), L17.

[180] Wang, Y.-M., and N. R., J. S. Magnetic flux transport and the suns dipole moment - new twists to the babcock-leighton model. *Astrophysical Journal 375* (1991), 761.

[181] Warren, H. P. Multithread hydrodynamic modeling of a solar flare. *Astrophysical Journal 637*, 1 (2006), 522–530.

[182] Wilhelm, K., Curdt, W., Marsch, E., Sch?hle, U., Lemaire, P., Gabriel, A., Vial, J. C., Grewing, M., Huber, M. C. E., Jordan, S. D., Poland, A. I., Thomas, R. J., K?hne, M., Timothy, J. G., Hassler, D. M., and Siegmund, O. H. W. SUMER - solar ultraviolet measurements of emitted radiation. *Solar Physics 162* (1995), 189–231.

[183] Wolf. Abstract of his latest results. *Monthly Notices of the Royal Astronomical Society 21*, 3 (1861), 77–78.

[184] Xu, Y., Cao, W., Ahn, K., Jing, J., Liu, C., Chae, J., Huang, N., Deng, N., Gary, D. E., and Wang, H. Transient rotation of photospheric vector magnetic fields associated with a solar flare. *Nature Communications 9* (2018), 1.

[185] Xu, Y., Cao, W., Ding, M., Kleint, L., Su, J., Liu, C., Ji, H., Chae, J., Jing, J., Cho, K., Cho, K., Gary, D., and Wang, H. Ultra-narrow Negative Flare Front Observed in Helium-10830 Å Using the 1.6 m New Solar Telescope. *Astrophysical Journal 819* (2016), 89.

[186] Xu, Y., Cao, W., Jing, J., and Wang, H. High resolution observations of white-light emissions from the opacity minimum during an X-class flare. *Astronomische Nachrichten 331* (2010), 596–598.

[187] Xu, Y., Cao, W., Jing, J., and Wang, H. Characteristic Size of Flare Kernels in the Visible and Near-infrared Continua. *Astrophysical Journal Letters 750* (2012), L7.

[188] Xu, Y., Cao, W., Liu, C., Yang, G., Jing, J., Denker, C., Emslie, A. G., and Wang, H. High-resolution observations of multiwavelength emissions during two x-class white-light flares. *Astrophysical Journal 641* (2006), 1210–1216.

[189] Xu, Y., Cao, W., Liu, C., Yang, G., Qiu, J., Jing, J., Denker, C., and Wang, H. Near-infrared observations at 1.56 microns of the 2003 october 29 x10 white-light flare. *Astrophysical Journal Letters 607* (2004), L131–L134.

[190] Xu, Y., Yang, G., Qiu, J., Spirock, T. J., Jing, J., Denker, C., and Wang, H. Visible and near-infrared contrast of faculae in active region NOAA 8518. *Chinese Journal of Astronomy and Astrophysics 4* (2004), 481–489.

[191] Yang, G., Xu, Y., Cao, W., Wang, H., Denker, C., and Rimmele, T. R. Photospheric Shear Flows along the Magnetic Neutral Line of Active Region 10486 prior to an X10 Flare. *Astrophysical Journal Letters 617* (2004), L151–L154.

[192] You, J. Q., and Oertel, G. K. What Caused an Unusually Broad He i 10830 Angstrom Emission Line in a Solar Limb Flare? *Astrophysical Journal Letters 389* (1992), L33.

[193] Yurchyshyn, V., Wang, H., Abramenko, V., Spirock, T. J., and Krucker, S. Magnetic field, hα, and rhessi observations of the 2002 july 23 gamma-ray flare. *Astrophysical Journal 605*, 1 (2004), 546–553.

[194] Zeng, Z., Qiu, J., Cao, W., and Judge, P. G. A Flare Observed in Coronal, Transition Region, and Helium I 10830 Å Emissions. *Astrophysical Journal 793*, 2 (2014), 87.

[195] Zirin, H. The helium chromosphere, coronal holes, and stellar X-rays. *Astrophysical Journal Letters 199* (1975), L63–L66.

[196] Zirin, H. Three flares with blue continuum, one with a D3 preflare shell. *Astrophysical Journal 235* (1980), 618–624.

[197] Zirin, H. *Astrophysics of the sun*) Cambridge University Press, Cambridge, 1988.

[198] Zirin, H., and Howard, R. The structure of the solar chromosphere. ii. spectroheliograms in λ 10830 å and their interpretation. *Astrophysical Journal 146* (1966), 367.

[199] Zirin, H., and Neidig, D. F. Continuum emission in the 1980 July 1 solar flare. *Astrophysical Journal Letters 248* (1981), L45–L48.